

# The role of Encapsulants in the long-term performance of advanced Crystalline Silicon Glass-Glass PV modules

Présentée le 27 juin 2022

Faculté des sciences et techniques de l'ingénieur  
Laboratoire de photovoltaïque et couches minces électroniques  
Programme doctoral en science et génie des matériaux

pour l'obtention du grade de Docteur ès Sciences

par

**Luca GNOCCHI**

Acceptée sur proposition du jury

Prof. A. Mortensen, président du jury  
Prof. C. Ballif, Dr A. F. A. Virtuani, directeurs de thèse  
Prof. G. Oreski, rapporteur  
Dr M. Owen-Bellini, rapporteur  
Dr Y. Leterrier, rapporteur





# Acknowledgments

*"Talent wins games, but teamwork  
and intelligence win championships."*

*Michael Jordan*

This manuscript is the result of more than four years of work. But not only that. It is also the logbook of an important piece of my life that I had the honor and pleasure to share with many people whom I would like to thank.

First and foremost, I want to thank my thesis director, Prof. Christophe Ballif, who believed in my abilities by offering me the opportunity to start on this path. Thank you for your guidance, for the fruitful discussions (sometimes just the few minutes we shared to smoke a cigarette together, but enough to come up with multiple ideas) and for challenging me on achieving always better results. Your determination and passion for PV have been an incentive and an example that I will hardly forget. Special thanks go to my thesis co-director, life teacher, colleague, and friend, Alessandro Virtuani. You always guided me wisely, providing constant support, especially during the toughest times (and there have been many). I dare not imagine what the outcome of this work would have been without your help.

I also want to thank my jury members Prof. Andreas Mortensen, Prof. Gernot Oreski, Dr. Michael Owen Bellini, and Dr. Yves Leterrier for taking the time to read the thesis, and providing helpful comments.

A huge thank you to the entire Modules Team - a true reliable one: Olatz, Fabiana, Alejandro, Andrew, and Hugo, the time spent together inside (and especially outside) the lab was simply fantastic. You are irreplaceable. Thank you also to my right-hand man, teacher of French and general Swiss culture, Xavier.

Thank you to my office-mates Peter and Mario, with whom I have shared not only the desk, but more importantly four years asking ourselves "Will we ever make it?". I wish you all the best in your future steps.

Thanks to the two pillars of PV-Lab: Aïcha and Karine; the sum of your every little gesture, thoughtfulness, and attention are essential for a healthy working environment (and PhD students mental sanity).

Thank you to all the PV-Lab colleagues and friends: Florent, Aymeric, Julie, Luca A., Marion, Audrey, Jean, Esteban, Eleonora, Ana, Quentin J., Jordan, Josua, Gizem, Lionel, Marina, Janina,

## Acknowledgements

---

Sofia, Ezgi, Deniz, Julien, Mostafa, Kerem, Jonathan, Samira, Quentin G., Franz, Mathieu, Nicolas, Christian, Sylvain, Cedric, ..., for the scientific contribution, the coffee breaks, the lunches, the aperitifs, the beers, the evenings spent together and all the time we shared. Thanks to the Microcity staff, Peter, Thierry, Hassan and Chady. Thanks also to the colleagues next door (CSEM) especially Andrea, Gianluca, Delphine, Leonardo, Frank, Jordi, Sylvain, Pierrick, Christophe, Jonathan, Jan-Willem...

Ce ne sont pas des collègues, ce qui explique pourquoi leur apport était encore plus précieux pendant ces années. Robinho, YaYa, Andre, Nico, Julien, Trig, Yannick, Aigoulita, ChaCha, Lau, JuJu, Valou... mercie du fond du coeur pour votre presence, soutien inconditionnel et Amitié!

Cari mamma e papà, Michi, ce l'abbiamo fatta (ancora una volta)! Un altro importante traguardo è stato raggiunto soprattutto grazie alla vostra presenza costante. La completa fiducia e piena libertà nelle decisioni importanti della vita, accompagnate dal vostro incessante sostegno e appoggio mi hanno permesso di poter aspirare ad obiettivi sempre piu' grandi ed ambiziosi. Grazie.

Finally, I thank you, dear reader, whoever you are. If you are reading these pages is because you are somehow interested in my thesis. I hope it can be of inspiration for your next experiments, or whatever your goal is... Good luck!

*Neuchatel, June 10, 2022*



# Abstract

The adoption of crystalline silicon (c-Si) PV modules based on glass-glass (G-G) structures is gaining momentum because of the possibility to manufacture bifacial panels, collecting light from the rear side. Despite not being an optimal material, Ethylene Vinyl Acetate (EVA) has become the dominant encapsulant in the PV industry. In fact, upon exposure to UV at high temperatures in the presence of moisture, EVA generates acetic acid (HAc), leading to the corrosion of the metallic interconnects. This problematic may be even more pronounced in a non-permeable G-G structure, compared to a conventional glass-backsheet (G-BS) design, in which HAc can be partially degassed out through the breathable BS. Nevertheless, some industries would like to continue using EVA in the manufacturing of G-G modules, because of the lower cost, the much longer track record and easier processability of EVA compared to newer alternatives, such as polyolefins (POs). In this work, we try to answer the question whether it is possible to use EVA in the manufacturing of G-G modules. The experimental chapters focus primarily on study the long-term reliability, in particular:

1. The sensitivity to water of different c-Si cell technologies (i.e. Aluminum Back Surface Field (Al-BSF), Passivated Emitter Rear Cell (PERC) and Silicon Heterojunction (SHJ)) exposed to damp heat (DH), where we highlight the good stability of the EVA, and the sensitivity to moisture of the SHJ solar cells.
2. We propose a detailed microscopic model explaining the degradation of the SHJ in DH. In reality, the presence of moisture (favored by the use of EVA) is only a contributing factor, as clearly indicated by the fact that the degradation is more pronounced in the presence of glass. Here we point at the role of a glass corrosion process and of NaOH in damaging the passivating properties of the cell. Either by reducing the water ingress (with an edge seal or a PO) or by replacing the glass type, the degradation phenomenon is not observed.
3. The impact of EVA storage conditions on the lamination quality and ultraviolet (UV) degradation. If good polymer storage and handling practices are carefully respected, the results tend to suggest that EVA can still be a viable solution to encapsulate G-G PV modules, for deployment in geographical zones where the humidity levels are not so high during the year (i.e. temperate climates). On the contrary, if these conditions are not observed, or in the event of module operating in a hot-humid climate, we believe that this may affect the long-term performance of G-G modules encapsulated with EVA.

4. An accelerated aging test for acetic acid corrosion (missing in the industry standards) is developed to probe wear-out and end-of-life behavior and facilitate screening of metallization, and interconnection technologies. Corrosion is in fact one of the main end-of-life failure modes in PV modules which use EVA. Here, SHJ cells with a low temperature silver paste-based interconnection outperformed cells with conventional solder-based interconnection (i.e. Al-BSF and PERC). The proposed corrosion test method can be optimized to match corrosion behavior observed in field modules with shorter times than standard damp heat tests.

These results give us a deeper insight on how to manufacture reliable and durable G-G modules, based on different cell technologies, and do not rule out the possibility to use EVA when targeting extended lifetimes of double glass panels.

**Key words:** Photovoltaic, Solar cell, Solar module, Reliability, Glass-Glass, Degradation, Long-term, Encapsulant, Ethylene Vinyl Acetate (EVA).

# Résumé

Le marché des modules photovoltaïques (PV) en silicium cristallin (c-Si) avec des structures verre-verre (G-G) gagne en importance en raison de la possibilité de fabriquer des panneaux bifaciaux, qui collectent la lumière également sur la face arrière. Bien qu'il ne s'agisse pas d'un matériau optimal, l'éthylène-acétate de vinyle (EVA) est devenu l'encapsulant dominant dans l'industrie photovoltaïque. Pourtant, après une exposition aux UV à des températures élevées et en présence d'humidité, l'EVA génère de l'acide acétique (HAc), ce qui entraîne la corrosion des interconnexions métalliques. Cette problématique peut être encore plus prononcée dans une structure G-G non perméable, par rapport à une conception conventionnelle glass-backsheet (G-BS), dans laquelle le HAc peut être partiellement dégazé à travers la BS perméable. Néanmoins, certaines industries souhaitent continuer à utiliser l'EVA dans la fabrication des modules G-G en raison de son faible coût, de l'historique beaucoup plus long et de la facilité de traitement de l'EVA par rapport à de nouvelles alternatives, telles que les polyoléfinés (PO). Dans ce travail, nous essayons de déterminer s'il est possible d'utiliser l'EVA dans la fabrication de modules G-G. Pour ce faire, les parties expérimentales se concentrent principalement sur l'étude de la fiabilité à long terme, et en particulier:

1. La sensibilité à l'eau de différentes technologies de cellules c-Si (c'est-à-dire Aluminum Back Surface Field (Al-BSF), Passivated Emitter Rear Cell (PERC) et Silicon Heterojunction (SHJ)) exposées à la chaleur humide, où nous soulignons la bonne stabilité de l'EVA, et la sensibilité à l'humidité des cellules solaires SHJ.
2. La sensibilité particulière de la SHJ à l'eau, phénomène pour lequel nous proposons un modèle microscopique détaillé. En réalité, la présence d'humidité (favorisée par l'utilisation d'EVA) n'est qu'un facteur contributif, comme l'indique clairement le fait que la dégradation est plus prononcée en présence de verre. Nous soulignons ici le rôle d'un processus de corrosion du verre et du NaOH dans la dégradation des propriétés passives de la cellule. Si l'on réduit l'entrée d'eau (avec un joint de bordure ou un PO) ou que l'on modifie le type de verre, le phénomène de dégradation n'est pas observé.
3. L'impact des conditions de stockage de l'EVA sur la qualité du laminage et la dégradation par les ultraviolets (UV). Si les bonnes pratiques de stockage et de manipulation des polymères sont soigneusement respectées, les résultats tendent à suggérer que l'EVA peut encore être une solution viable pour encapsuler les modules PV G-G, pour un déploiement dans des zones géographiques où les niveaux d'humidité ne sont pas trop élevés pendant l'année (c'est-à-dire les climats tempérés). Au contraire, en cas de

fonctionnement du module dans un climat chaud-humide, nous pensons que cela peut affecter les performances à long terme des modules G-G encapsulés avec de l'EVA.

4. Un test de vieillissement accéléré pour la corrosion par l'acide acétique (absent des normes industrielles), qui a été développé pour sonder le comportement d'usure et de fin de vie et faciliter la sélection des technologies de métallisation et d'interconnexion. La corrosion constitue l'un des principaux modes de défaillance en fin de vie des modules PV qui utilisent l'EVA. Ici, les cellules SHJ avec une interconnexion à base de pâte d'argent à basse température ont surpassé les cellules avec une interconnexion conventionnelle à base de soudure (c'est-à-dire Al-BSF et PERC). Cette méthode d'essai de corrosion proposée peut être optimisée afin de simuler le comportement de corrosion observé dans les modules de terrain mais avec des temps plus courts que les tests standards de chaleur humide.

Ces résultats nous permettent de mieux comprendre comment fabriquer des modules G-G fiables et durables, basés sur différentes technologies cellulaires, et n'excluent pas la possibilité d'utiliser l'EVA lorsque l'on vise une durée de vie prolongée des panneaux à double vitrage.

**Mots clés:** Photovoltaïque, Cellules solaires, Panneaux solaires, Fiabilité, Double vitrage, Dégradation, Long terme, Encapsulant, éthylène-acétate de vinyle (EVA).

# Contents

<b>Acknowledgements</b>	<b>iii</b>
<b>Abstract</b>	<b>v</b>
<b>1 Introduction</b>	<b>1</b>
1.1 Motivation . . . . .	1
1.2 Competitiveness of Photovoltaic . . . . .	2
1.2.1 PV Market evolution . . . . .	2
1.2.2 Improvement strategies . . . . .	3
1.3 Crystalline silicon PV modules . . . . .	5
1.3.1 Solar cell technologies . . . . .	6
1.3.2 Metallic interconnection . . . . .	8
1.3.3 Module packaging . . . . .	10
1.4 Reliability in photovoltaic . . . . .	12
1.4.1 Degradation modes . . . . .	13
1.4.2 Qualification standard tests . . . . .	15
1.4.3 Lifetime prediction complexities . . . . .	17
1.5 The role of the encapsulant . . . . .	20
1.5.1 Material selection . . . . .	21
1.5.2 EVA formulation . . . . .	21
1.5.3 The lamination process . . . . .	22
1.5.4 Causes and effects of EVA degradation . . . . .	24
1.6 The potential of the glass-glass PV module layout . . . . .	26
1.6.1 Encapsulant alternatives for G-G modules . . . . .	30
1.7 Conclusions . . . . .	30
1.8 Structure of the thesis . . . . .	31
1.9 Contribution to the research field . . . . .	32
<b>2 Experimental methods</b>	<b>33</b>
2.1 Sample design & materials . . . . .	33
2.1.1 Front and back cover glass . . . . .	33
2.1.2 Solar cells . . . . .	34
2.1.3 Metallization . . . . .	34
2.1.4 Encapsulants and edge sealant . . . . .	35

## Contents

---

2.2	Tools for characterization of module and cell performance . . . . .	35
2.2.1	Current-voltage (I-V) measurements . . . . .	35
2.2.2	Electroluminescence (EL) . . . . .	37
2.2.3	Photoluminescence (PL) . . . . .	38
2.3	Tools for characterization of module materials . . . . .	38
2.3.1	Fourier Transformed Infrared (FTIR) spectroscopy . . . . .	38
2.3.2	UV visible Near infrared (UV-Vis-NIR) spectroscopy . . . . .	39
2.3.3	Raman Spectroscopy . . . . .	39
2.3.4	Differential scanning calorimetry (DSC) . . . . .	39
2.3.5	Scanning Electron Microscopy (SEM) . . . . .	41
2.4	Indoor aging tests . . . . .	41
2.4.1	Damp Heat (DH) . . . . .	41
2.4.2	UV aging . . . . .	42
<b>3</b>	<b>Moisture ingress in G-G modules encapsulated with EVA</b>	<b>43</b>
3.1	Introduction . . . . .	43
3.2	Experimental methods . . . . .	44
3.2.1	Sample fabrication . . . . .	44
3.2.2	Aging test . . . . .	44
3.2.3	Module and material characterization . . . . .	45
3.3	Results . . . . .	45
3.3.1	Effect of the Relative Humidity . . . . .	45
3.3.2	Water ingress modeling . . . . .	48
3.4	Discussion . . . . .	50
3.5	Conclusions . . . . .	52
<b>4</b>	<b>Insights into the sensitivity of SHJ modules to damp heat: a microscopic model</b>	<b>53</b>
4.1	Introduction . . . . .	54
4.2	Experimental details . . . . .	54
4.2.1	Samples design and fabrication . . . . .	55
4.2.2	Module characterization . . . . .	56
4.2.3	Cells and materials characterization . . . . .	57
4.3	Results . . . . .	57
4.3.1	Module electrical characterization . . . . .	57
4.3.2	Analysis of the metallization . . . . .	58
4.3.3	Characterization of the encapsulant . . . . .	59
4.3.4	Effect of moisture on passivating cell layers and interface . . . . .	61
4.3.5	The effect of moisture on different module structures . . . . .	62
4.3.6	Glass corrosion and the role of sodium . . . . .	63
4.3.7	Na <sup>+</sup> droplet test . . . . .	65
4.4	Degradation model . . . . .	65
4.5	Mitigation strategies . . . . .	67
4.6	Conclusions . . . . .	69



<b>5</b>	<b>The Effect of Storage Conditions on the Long-Term Stability of EVA</b>	<b>71</b>
5.1	Introduction . . . . .	71
5.2	Experimental details . . . . .	72
5.2.1	Storage conditions . . . . .	73
5.2.2	Samples design and fabrication . . . . .	73
5.2.3	Aging conditions . . . . .	74
5.2.4	Module inspection and performance . . . . .	74
5.2.5	EVA properties . . . . .	75
5.3	Results . . . . .	75
5.3.1	After lamination – unaged samples . . . . .	75
5.3.2	UV aging . . . . .	77
5.4	Summary and discussion . . . . .	83
5.5	Conclusions . . . . .	84
<b>6</b>	<b>Corrosion testing of solar cells: Wear-out degradation behavior</b>	<b>87</b>
6.1	Introduction . . . . .	87
6.2	Experimental methods . . . . .	89
6.2.1	Module fabrication . . . . .	89
6.2.2	Corrosion testing . . . . .	89
6.2.3	Module and material characterization . . . . .	90
6.3	Results and discussion . . . . .	91
6.3.1	Al-BSF modules . . . . .	91
6.3.2	PERC and SHJ modules . . . . .	94
6.4	Applications to module development . . . . .	95
6.5	Conclusions . . . . .	95
<b>7</b>	<b>Conclusions and perspectives</b>	<b>97</b>
7.1	Summary . . . . .	97
7.2	General conclusion on the use of EVA in a glass-glass PV module . . . . .	99
7.3	Perspectives . . . . .	100
<b>A</b>	<b>Evaluation of the diffusion properties of EVA</b>	<b>103</b>
<b>B</b>	<b>Water ingress simulations during indoor DH test</b>	<b>107</b>
<b>C</b>	<b>Effect of moisture on SHJ passivating cell layers and interface: i/p a-Si:H and i/pa-Si:H with ITO samples</b>	<b>109</b>
<b>D</b>	<b>Effect of the <math>\text{NaCl}_{aq}</math> on SHJ cells exposed to DH</b>	<b>111</b>
<b>E</b>	<b>Effect of the UV on Al-BSF, PERC, and SHJ G-G modules</b>	<b>113</b>
<b>F</b>	<b>Measurements of the water content in uncured EVA foils after storage</b>	<b>117</b>
<b>G</b>	<b>Water ingress simulations during real outdoor exposure</b>	<b>119</b>



# List of abbreviations

<b>Al-BSF</b>	Aluminium back surface field
<b>AlO<sub>x</sub></b>	Aluminum oxide
<b>a-Si:H</b>	Hydrogenated amorphous silicon
<b>a-Si</b>	Amorphous silicon
<b>BBs</b>	Busbars
<b>BI-PV</b>	Building integrated photovoltaic
<b>BOM</b>	Bill of materials
<b>BOS</b>	Balance-of-system
<b>BS</b>	Back-sheet
<b>C-AST</b>	Combined-accelerated stress test
<b>CB</b>	Conduction band
<b>CIGS</b>	Copper-indium-gallium-selenide
<b>CO<sub>2</sub></b>	Carbon dioxide
<b>c-Si</b>	Crystalline silicon
<b>CTM</b>	Cell-to-module
<b>DH</b>	Damp heat
<b>EVA</b>	Ethylene vinyl acetate
<b>G-BS</b>	Glass-backsheet
<b>G-G</b>	Glass-glass
<b>HAc</b>	Acetic acid
<b>HALS</b>	Hindered amine light stabilizer

## Contents

---

<b>HF</b>	Humidity freeze
<b>IEA</b>	International energy agency
<b>IEC</b>	International electrotechnical commission
<b>JPL</b>	Jet propulsion laboratory
<b>LCOE</b>	Levelized cost of electricity
<b>LID</b>	Light-induced degradation
<b>MAST</b>	Module-accelerated stress test
<b>PA</b>	Polyamide
<b>PCE</b>	Power conversion efficiency
<b>PDMS</b>	Polydimethyl siloxane
<b>PECVD</b>	Plasma enhanced chemical vapor deposition
<b>PERC</b>	Passivated emitter rear cell
<b>PID</b>	Potential induced degradation
<b>PO</b>	Poly-olefines
<b>PP</b>	Polypropylene
<b>PV</b>	Photovoltaic
<b>PVB</b>	Polyvinyl butyral
<b>SHJ</b>	Silicon heterojunctions
<b>SiN<sub>x</sub></b>	Silicon nitride
<b>SiO<sub>x</sub></b>	Silicon oxide
<b>SLP</b>	Service life prediction
<b>STC</b>	Standard test conditions
<b>SWCT</b>	Smart wire connection technology
<b>TC</b>	Thermal cycling
<b>TOPCon</b>	Tunnel oxide passivated contacts
<b>UV</b>	Ultraviolet
<b>VB</b>	Valence band
<b>VI-PV</b>	Vehicle-integrated photovoltaic



# 1 Introduction

This chapter aims to provide the most relevant insights into the recent design and materials used in fabricating crystalline silicon (c-Si) based PV modules. The global PV field continuously researches new solutions to improve cell efficiency and module reliability. The main challenge is to continue developing all these aspects while maintaining or even reducing the fabrication cost. Given the considerable progress witnessed by the technology in recent years, the next generation of solar panels deployed over the next 10-15 years will be different from the technology deployed today. A better understanding of the different materials and their developments through the years is crucial, and we should carefully look at the complexities of what drives production and what potentially limits further improvements in the PV reliability field.

## 1.1 Motivation

The industrial revolution started at the beginning of the 18th century has brought a huge economic transformation putting energy as the foundation of modern society. An easier and faster energy availability brought great benefits to the world population, improving the wealth and quality of life through rapid evolution of technologies, goods accessibility, and affordability. On the other hand, the continuous increase in energy demand has led to a significant production of greenhouse gases, such as carbon dioxide (CO<sub>2</sub>). Today, the global energy system relies mainly on fossil fuels, and its uncontrolled use contributes to a global warming through the massive emission of CO<sub>2</sub> in the atmosphere. The change in global surface temperatures is a natural effect that can not be controlled. However, the superposition of anthropogenic activities leads to an unprecedented increase rate. The direct consequences of climate change are already noticeable and the consequences for our planet can be catastrophic [1].

During the 21st Conference of Parties (COP 21), the United Nations climate summit held in 2015, 196 parties signed the Paris Agreement, which aims at keeping the rise in mean global temperature below 2 °C above pre-industrial levels [2]. The main strategy to reduce carbon

emissions relies on a huge energetic transition plan. In this framework, renewable energies should overtake traditional fossil fuel (oil, coal, and gas) based energy sources.

In 2020, the global primary energy consumption was around 166000 TWh, with a moderate reduction of ~4% over 2019 strictly related to the Covid-19 pandemic restrictions [3]. Nevertheless, the 80% of the global energy system still relies on fossil resources. When transport demand will return to pre-Covid levels, global energy demand will rise even higher, to almost 2% above 2019 levels [4]. With a growth rate of about 2%/year, it is expected that by 2050 the global primary energy consumption will reach 250000 TWh. The total proven reserves of coal, oil, and natural gas amount to 8.4 million, 2.9 million, and 2.1 million TWh, respectively [3]. Even ignoring the disastrous ecological consequences of burning carbon-based fuel, this amount is still not enough for even 100 years needs at the 2019 rate of consumption [3]. It is, therefore, crucial to increase the energy produced by renewable sources.

In order to reach net-zero emissions by 2050, the International Energy Agency projects that 80% of the total energy production has to be supplied by a mix of solar, nuclear, wind, and others [5]. Solar photovoltaic (PV) is expected to count the largest contribution supplying about the 30%, corresponding to ~ 80000 TWh of Primary energy in the BP reporting method. The trustworthiness is motivated by the outstanding progress established during the years as a result of manufacturing and joint efforts between industrial partners and scientific collaborators to make PV a reliable and affordable technology. However, there is still more to do to meet the over-cited targets.

## 1.2 Competitiveness of Photovoltaic

### 1.2.1 PV Market evolution

The PV technology has been successfully adopted firstly in the aerospace field since 1958. The idea of a solar panel market for terrestrial application rose in 1973. The first oil crisis sparked governments everywhere to accelerate innovation and research into renewable energies. At the beginning of the 2000s, with the concerns and evidence of climate change, the PV market started to take over for terrestrial applications. Governments brought substantial economic support in terms of feed-in tariff programs, subsidies investments, and new regulations to promote the installation of solar panels [6].

According to the International Energy Agency (IEA), the global cumulative installed PV capacity has increased from 1.4 GW in 2000 to 773 GW in 2020 [7], with a new annual installation record set in 2021, with an **added capacity of about 160 GW** [8] as reported in Figure 1.1. Besides supportive policies, reasons for this constant market growth are the steady reduction of PV module costs (-80% since 2010) and the increasing competitiveness of the technology, driven by constant progress in solar cell efficiency and module reliability.

The growth rate of the PV market is encouraging. However, the production and installation

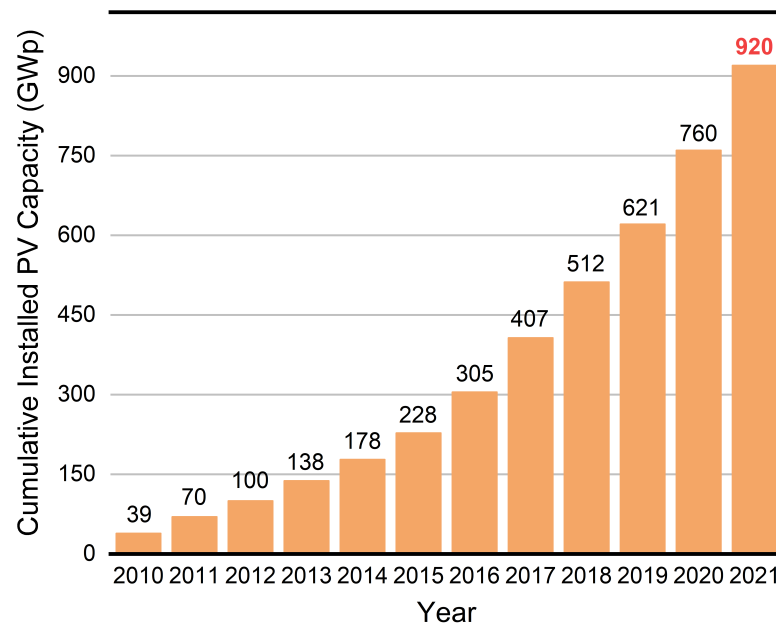


Figure 1.1: Cumulative Installed PV Capacity chart from 2010. Production is measured in Watts-peak, which is the Watt rating of each module at standard  $1000 \text{ W/m}^2$  intensity, summed over all modules produced. Data source: [8, 9].

rates need to be further increased to achieve the targeted 30000 TWh by 2050.

### 1.2.2 Improvement strategies

Photovoltaic is employed in various power systems that range from small residential installations - rooftop-mounted PV systems - to large utility-scale systems PV plants -. New approaches such as building-integrated photovoltaic (BI-PV), and vehicle-integrated photovoltaic (VI-PV) are promising solutions to boost even more the market in the coming years. To further increase the PV adoption rate, people need to be tempted to invest their own money.

An important parameter to consider when evaluating whether to invest in a photovoltaic installation is the **energy yield** of the module. It is a factor linked to the electricity generation cost; therefore, its estimation is particularly strategic for the potential owner. The energy yield is defined as the amount of energy (in kWh) produced by the PV plant over its estimated lifetime. The **levelized cost of electricity** (LCOE) is a typical figure in the PV field, used to compare the electricity cost of various power generation technologies. Specifically, the LCOE is a present value assessment of the total system costs evaluated over its lifetime. There are different formulas to calculate the LCOE value however, the basic principle is the same. It is the ratio between total life-cycle system costs and the total energy yield of the system over its lifetime:



$$LCOE = \frac{\text{Lifecycle Cost}}{\text{Lifetime Energy Yield}} \quad (1.1)$$

It is expressed in €/Wh and incorporates all types of costs the owner will be subjected to, such as initial investment costs and annual operational and maintenance expenses. The LCOE value is also a function of more financial-related parameters (i.e discount rate, and potential additional fees). For a more detailed explanation, the reader can refer to [10]. A simple expression of the LCOE formula is:

$$LCOE = \frac{CAPEX + \sum_{n=1}^N \frac{OPEX - RV}{(1+r)^n}}{\sum_{n=1}^N \frac{Y_0 \cdot (1-D)^n}{(1+r)^n}} \quad (1.2)$$

where:

$N$  is the number of years in operation [years];

$CAPEX$  is the total initial investment [€/kWp];

$OPEX$  is the sum of the annual operation and maintenance expenses [€/kWp];

$RV$  is the residual value [€/kWp];

$r$  is the discount rate [%];

$Y_0$  is the initial energy yield [kWh];

$D$  is the system annual degradation rate [%].

The outstanding improvements in recent years regarding silicon purification and wafer fabrication steps, along with the increased production volume, have resulted in a considerable cost reduction [11]. Today, less than 40% of the total price of a residential PV installation is represented by the c-Si module cost [9]. The remaining percentage counts for the balance-of-system (BOS) costs, namely - the inverters, cabling/wiring, mounting system, and installation [9]. However, these costs are not easily reducible, as shown in Figure 1.2.

As reported by Jordan *et al.* [12], the reduction of the LCOE can be obtained on different levels. In particular, the two applicable strategies on a module level are:

- Increase the power conversion efficiency (PCE) of the modules and inverters (i.e. increase the initial energy yield,  $Y_0$ ).
- Increase the service life of the full system and components (i.e. reduce the annual degradation rate,  $D$ ).

Specifically, **the work done during the time of this thesis focused on studying and under-**

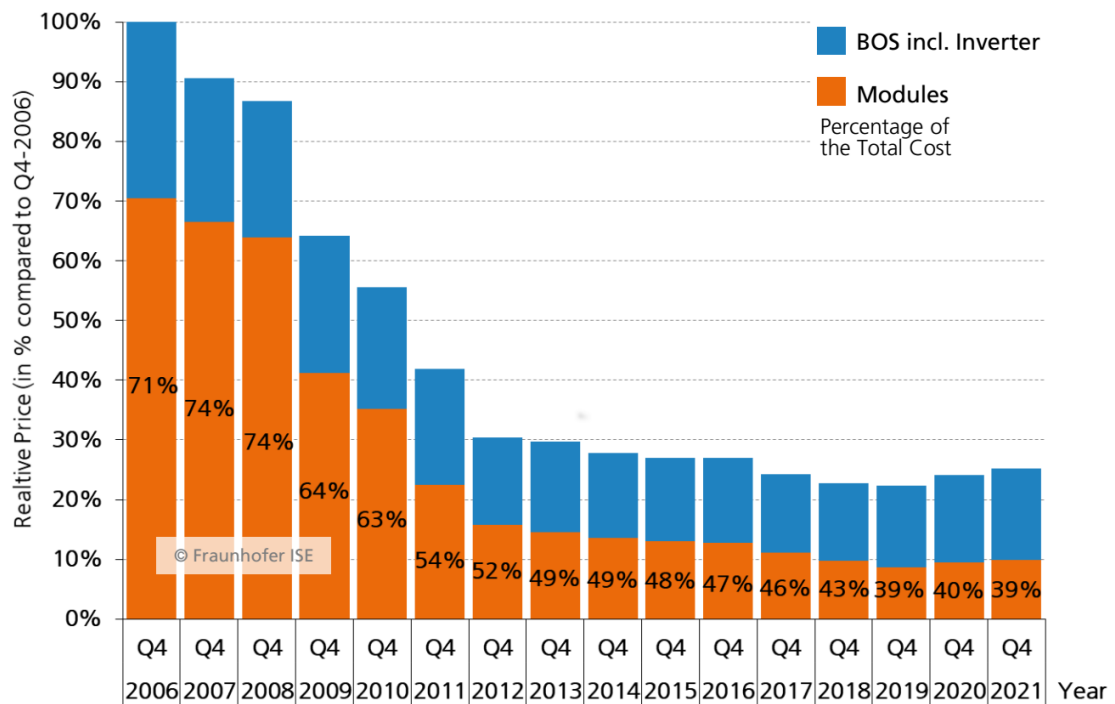


Figure 1.2: Evolution of PV installation costs from 2006 to 2021 for PV Rooftop Systems in Germany. Overall costs have reduced of 70-75% in 10 years. Image taken and adapted from [13].

**standing of PV module degradation.** Extending the energy life (and minimizing degradation) of the system and components (modules) may greatly impact LCOE and the profitability of investments in solar parks. In fact, PV modules still make up about 30% of overall installation CAPEX costs of 0.50 to 0.70 €/W in many countries (in 2020), as reported in Figure 1.3. Additionally, over an estimated service lifetime of 25-30 years, several components are expected to be changed, such as the inverters. Nevertheless, no substitution of solar panels is envisioned in the business plans of solar parks. A sub-standard module performance may considerably impact the profitability and LCOE of solar projects.

### 1.3 Crystalline silicon PV modules

The production of a standard solar panel (i.e. encapsulated crystalline silicon-based solar cells) requires different materials, such as semiconductor absorber to capture the sunlight (i.e. silicon wafers), conductors to extract the converted electricity (i.e. metallic interconnection), and insulators to prevent safety hazard and provide physical insulation to the whole module against climatic aging stresses (i.e. polymeric encapsulant and rear-sheet, and the front glass).

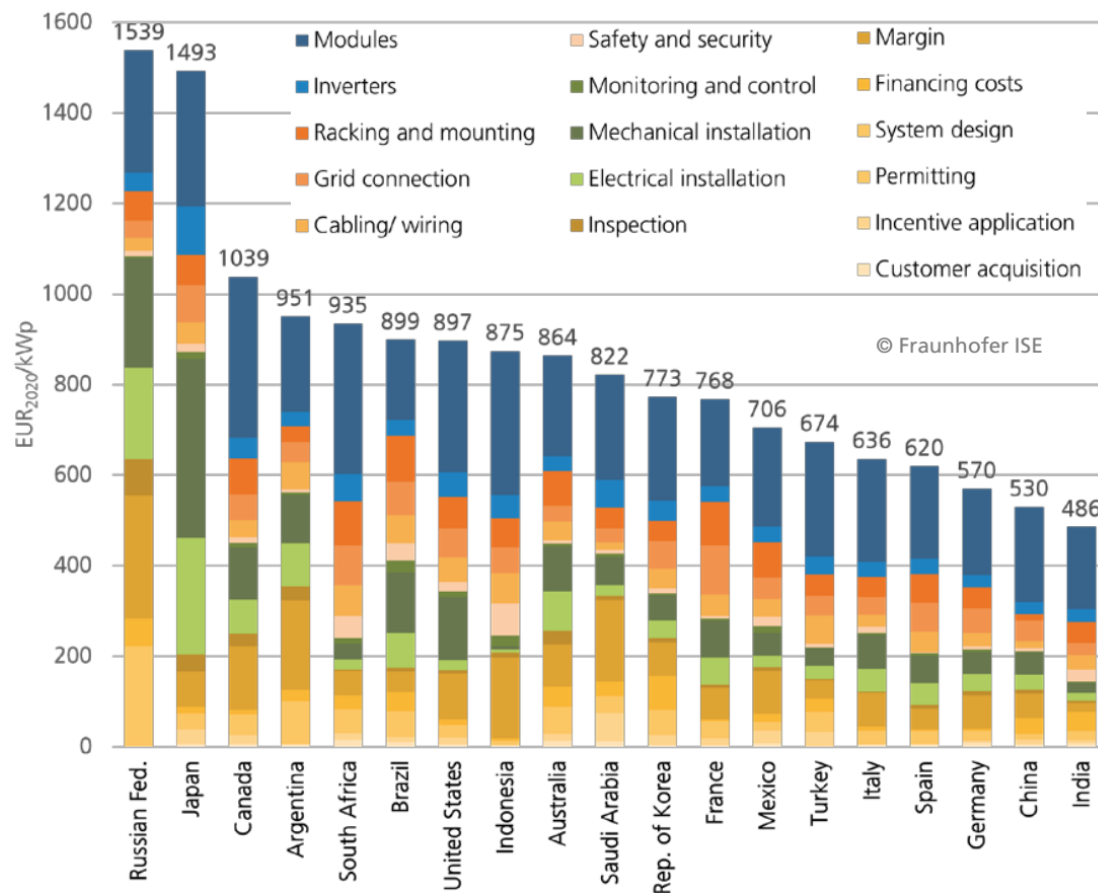


Figure 1.3: Utility-scale PV total installed costs by country in 2020. Image taken and adapted from [9]. Data source: [13], currency converted from USD to EUR. Date of data: Jun-2021.

### 1.3.1 Solar cell technologies

The solar cell is the **active unit** that allows the sunlight to be collected and directly converted into electricity. The physical mechanism is based on the special capability of certain materials called semiconductors to absorb the radiation in a specific wavelength interval. When the energy of the impinging photon is higher than the energy band-gap of the material, there is a certain probability that the photon get absorbed by an electron. The *excited electron* is then "promoted" from the valence band (VB) to the higher energetic level, called the conduction band (CB). After the *electronic jump*, a positive free state is left behind in the valence band, a *hole*. To produce electricity, the two charge carriers must be *collected* separately to avoid them recombining, then *transported* to the surface of the material, and finally *extracted* out. The final cell device is the result of multiple fabrication steps.

Despite different semiconductors being available and can be processed as solar cells, the annual PV module production is almost exclusively based on **crystalline silicon (c-Si)** wafers, with more than 95% of the global market. The remaining 5% is represented by thin-film technologies, such as cadmium-telluride (CdTe), copper-indium-gallium-selenide(CIGS), and

amorphous silicon (a-Si) modules. In fact, silicon is an abundant, relatively cheap, and non-toxic material on the earth's crust. Its physical and chemical properties are well known because it is the base material used in the microelectronics industry. Additionally, the band-gap value of c-Si (i.e. 1.1 eV) is well suited for the solar spectrum and makes it an excellent candidate for PV applications.

The emphasis of this thesis is on c-Si-based PV modules. The following sections will focus on different aspects of this specific technology.

Until 2015-2016, c-Si cells were based on the so-called aluminum back surface field (Al-BSF) cell type. This technology offers a low cost with a limited number of fabrication processing steps. The carrier collection is improved by the heavily doped rear side of the wafer with aluminum atoms. However, the direct contact between the silicon wafer and metallization causes a high carrier recombination rate (i.e. low achievable lifetime value), limiting the cell efficiency to 20% (see Figure 1.4a).

In approximately five years, this type of technology has been almost entirely replaced by the more efficient and sophisticated PERC (Passivated Emitter Rear Cell) concept [14] (see Figure 1.4b). The major improvement of this cell is characterized by the introduction of an insulating layer ( $\text{AlO}_x$  or  $\text{SiN}_x$ ) at the rear side with only localized openings to reduce the direct metal-silicon contact. This creates increased surface passivation leading PCE of 23.56% (mono-facial p-type mono-crystalline silicon cell) for industrial solar cells manufactured by Trina Solar [15]. The fast transition from Al-BSF to PERC is facilitated by the possibility of easily upgrading a standard Al-BSF production line to fabricate PERC cells.

The Tunnel Oxide Passivated Contacts (TOPCon) cell types are even more advanced with respect to the PERC concept. The peculiarity of this cell type is the deposition of a thin silicon oxide ( $\text{SiO}_x$ ) layer capped by doped poly-silicon deposited on both sides of the wafer improving cell passivation (see Figure 1.4c). Carriers transport is still allowed by tunneling effect, or through a pinhole's net across the insulating  $\text{SiO}_x$  layer [16, 17]. The best-industrialized cells have been reported by JinkoSolar company, with a PCE of 25.25% (mono-facial n-type mono-crystalline silicon cell) [18].

A different approach to obtain a fully passivated area consists in the deposition, on both sides of the wafer, of an hydrogenated amorphous silicon (a-Si:H) layer (see Figure 1.4d) [19,20]. The plasma-enhanced chemical vapor deposition (PECVD) technique allows to introduce dopants (i.e. boron for p-type and phosphorus for n-type) in the gas mixture to form selective charge contacts on each side. High open-circuit voltage values are achieved with silicon heterojunction (SHJ),  $> 700$  mV [21] and the current world record silicon solar cell with efficiency of 26.7% (by Kaneka) [22], employing an interdigitated back-contact structure (i.e. no carrier extraction metallization lines at the front side). One major difference between PERC/TopCon and SHJ is the thermal budget of the processing: the presence of the a-Si:H reduces the maximum allowed exposure temperature of SHJ cells to 200°C. Higher temperatures may damage the a-Si:H layers leading to losses in the cells' passivation properties. This aspect is important when

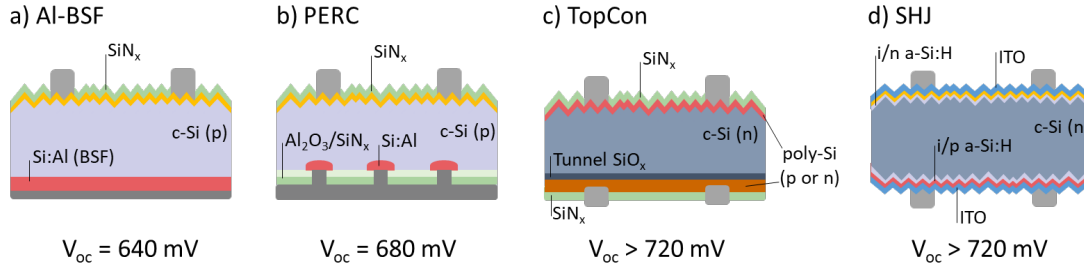


Figure 1.4: Evolution of c-Si solar cell technologies. a) Aluminum back surface field (Al-BSF), b) Passivated emitter and rear cell (PERC), c) Tunnel Oxide Passivated Contacts (TOPCon), d) Silicon heterojunction cell (SHJ).

cells are interconnected in a module. In fact, the soldering process of ribbons (i.e stringing step) in conventional cells uses soldering at temperatures around 400°C. Understandably, the same process cannot be used for SHJ. More details regarding the stringing technologies for SHJ cells are described in the following section.

### 1.3.2 Metallic interconnection

Different interconnection levels are present in a c-Si PV module. The adopted terminology might be somewhat confusing. In this thesis, we refer to [23] and the scheme shown in Figure 1.5.

The extraction of the generated charge carriers transported to the front surface of the solar cell is allowed by the presence of a thin silver-based line-net called *gridlines* (or **fingers**). They run straight the cell width, and the size is the suitable trade-off to maximize the current extraction and limit the shadowing of the cell's active area. The current then makes its path towards the **busbars** (BBs), thicker silver lines perpendicularly aligned with respect to the fingers. These two contacts are printed onto the surface via screen printing technology. The rear side of a standard cell is completely metalized. The silver plating is necessary to improve current conductivity (at the front side) and reduce oxidization (at the rear side).

Since the power generated by a single cell is relatively low (i.e. approximately 5 W), several cells need to be interconnected in series to reach a meaningful power level. The connection is done by first aligning two cells and connecting the positive side of one cell to the negative side of the following. Then, **cell interconnect ribbons** are soldered on top of the busbars. One line of interconnected cells is called a *string*. Finally, multiple strings are connected by **string interconnect ribbons**. Ribbons are copper strips coated by a protective lead-tin layer, promoting good contact and adhesion to the cell busbars.

The stringing process is important as it is responsible for the final electrical properties of the module. A typical solar panel counts 60 or 72 stringed cells.

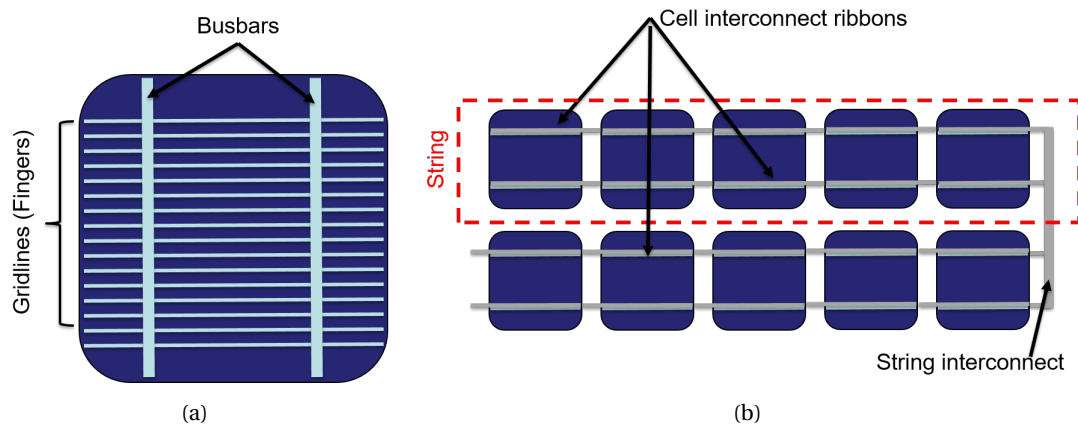


Figure 1.5: Schematic sketch of the metallization interconnections in a PV module. (a) Metallic connectors on the silicon cell: gridlines and busbars are screen-printed on the cell; (b) Illustrative example of a module string: multiple cells are interconnected by means of copper strings coated with a layer of lead-tin alloy; multiple strings are then interconnected by means of string interconnect wires.

The design of PV modules has changed only marginally during the last decades. However, we are witnessing a considerable revolution during the last five years, with several innovative concepts being introduced on the market. Improvements on the modules level are becoming more critical in improving the cell-to-module (CTM) power ratio and the module service lifetime.

Innovation in the interconnection and cell design boosts the module power rating. The standard 2 (or 3) busbars are now replaced by 5 or 7 (or more) thinner metal lines. The number of busbars (and cell ribbons) can be increased, further-reaching what is generally called *multi-busbars*. Adding more busbars reduces the gap between them, shortening the finger length. Consequently, the current load on the fingers is lowered. This allows for making much narrower busbars, decreasing resistive losses and the silver consumption [24]. *Smart Wire Connection Technology* (SWCT) is also another innovative concept developed by Meyer Burger and mainly used for SHJ technology [25]. Thin metal lines are already embedded in the encapsulant sheet, and the low-temperature soldering is done directly during the lamination step. Each of the 18 lines is in direct contact with the fingers. This approach also reduces silver consumption with no need for busbars. An example of some interconnection technologies is reported in Figure 1.6.

Other concepts as *shingling cells* do not require ribbons as the partial overlapping of adjacent cells gives the interconnection. A different approach is the use of *half cells*. The halved dimension reduces the generated current and Ohmic resistive losses in the copper busbars or wires.

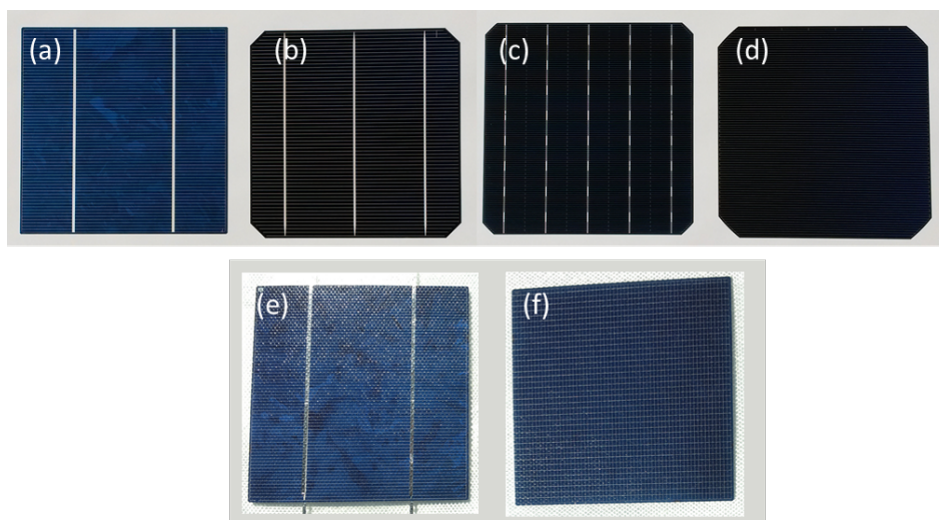


Figure 1.6: The top row shows different c-Si cell interconnection technologies (a) standard two (2BB), (b) three (3BB), (c) five (5BB) busbar and (d) cell without busbars (below right). Current-collecting fingers are placed perpendicular to the busbars. The second row shows two encapsulated solar cells: (e) c-Si solar cells with 2BBs and ribbons, and (f) solar cell with no ribbons and the smart wire connecting technology. Images adjusted from [26].

### 1.3.3 Module packaging

PV modules are expected to operate outdoor for more than 20 years. A packaging structure is needed, as schematically represented in Figure 1.7, to protect solar cells from outdoor weathering.

After the stringing process, cells are placed in a lay-up station, along with a front and rear cover. The **front** is usually a 3.2 mm-thick tempered or heat-strengthened **glass plate** with specific requirements, such as high transparency (to let sunlight reach the solar cells), good physical insulation (to avoid moisture diffusion into the cell circuit) and mechanical stability (to avoid cells to get damaged by outdoor stresses, such as wind, snow or hail). The rear can be a second glass plate or more often, a polymeric multi-layer sheet, called **back-sheet** (BS). It mimics the front glass without the need for optical transparency. Two polymeric sheets, called the **encapsulant** are inserted, one on each side of the stringed cells. The polymer has to guarantee certain physical insulation, UV and mechanical stability, and its optical properties need to match the one of the front glass well. During the lamination process step, the encapsulant melts and provides the final adhesion between all components in a single "laminate structure". A more detailed explanation of the lamination and process parameters are given in Section 1.5.3. Finally, the edges are trimmed, and an **aluminum frame** gives the final mechanical stability. The **junction box** is glued at the rear of the module to extract – by means of cables and connectors - the generated electrical power.

Proper packaging is essential in ensuring the long-term stability of PV modules and a long service lifetime. Longer lifetimes and modules with a modified visual appearance (such as

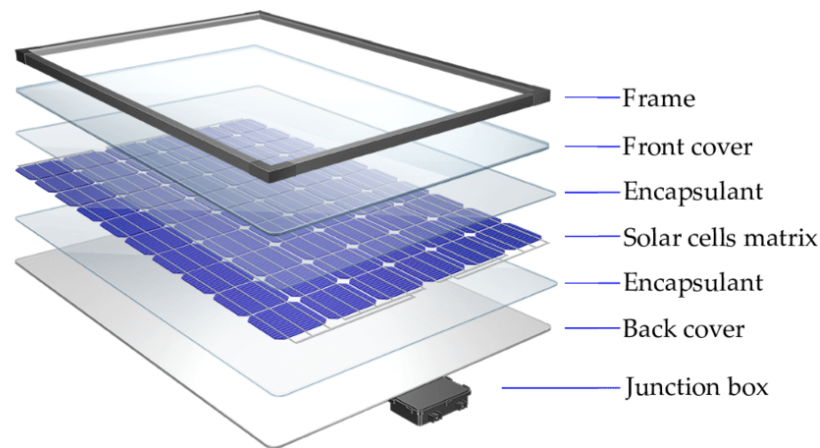


Figure 1.7: Scheme of the layers of a typical c-Si based PV module. From front to rear side: aluminum frame, front glass plate, front encapsulant foil, interconnected solar cells, rear encapsulant foil, back-sheet, junction box.

colored modules) contribute to bring fresh ideas to the module design. White PV modules variant is an attractive alternative for BI-PV applications [27].

The market of back-sheets offers a variety of options. There are mainly two categories: fluoropolymer (i.e. Tedlar from Dupont) and non-fluoropolymer (PET configuration). Alternative extruded backsheets based on polypropylene (PP) are gaining interest. In fact, the production of co-extruded allow for easy material design and formulation adjustments. Recent results published by Oreski *et al.* [28] suggest that co-extruded PP based BS can be a valid option to replace standard PET foils.

Another interesting trend for the rear cover is the increasing double-glass (G-G) configuration market expected in the coming years. As a matter of fact, bifacial cell architectures are easily produced with the new technologies described above (i.e. PERC, TopCon, SHJ). Additionally, the second cover glass on the rear side increases the physical insulation, and mechanical stability of the module [29]. These aspects are encouraging G-G PV manufacturers to extend the performance warranty of their products up to +35 years. A more detailed description of the glass-glass structure is presented in Section 1.6.

In a *sandwich* structure like that of solar modules, the transparent polymeric encapsulant foil serves multiple purposes, such as providing the adhesion between components, good physical insulation, and ensuring optical coupling between the front glass and the solar cells. A variety of formulations are commercially available for the PV industry. These include thermoplastic polymers (or thermoplastics, TPs) and thermosetting polymers (or elastomers). The main difference between the two classes of polymers is the type of bonding created after being processed. Specifically, in a thermosetting polymer, strong covalent bonds are formed between molecules thanks to a cross-linking agent added to the resin, which creates a three-dimensional cross-linked network. After the chemical reaction, the elastomer does not



soften and cannot be reshaped. In a thermoplastic formulation, the bonds between molecules are Van Der Waals forces weaker than thermoset polymers. In fact, TPs may suffer spatial displacements (i.e creep) if heated up at their melting temperature.

Thermoplastics include PVB (polyvinyl butyral), TPU (thermoplastic polyurethane), and Ionomer. The thermo-setting ethylene vinyl acetate (EVA) formulation has stood for encapsulant since ever. Its market share (> 80% [30]) is expected to be maintained in the near future thanks to the cost-properties ratio. More recently developed polyolefin elastomers (POs) are expected to perform better outdoor [31], but the cost is yet too high with respect to EVA. A detailed description of the encapsulant, with a focus on the EVA, is presented in Section 1.5.

### 1.4 Reliability in photovoltaic

The terminology used when speaking about PV reliability is sometimes misused. Before describing the different aspects and the crucial importance of reliability in PV, it is worth clarifying some terms and their general meaning.

**Reliability** is an important research field in many industries. Its definition is given in [32] as "*the ability [of a system or component] to perform as required, without failure, for a given time interval, under given conditions*". **Failure** is "*the loss of ability to perform as required*".

A generic reliability function,  $R(t)$ , expresses the probability that a specific product performs as required by time. Reliability at time  $t$  is therefore expressed as  $R(t) = 1 - F(t)$ , where  $F(t)$  is called the *cumulative failure distribution function* and represents the probability that the specific product will fail by time  $t$ .

The **durability** of an item is instead the "*ability to perform as required, under given conditions of use and maintenance, until the end of useful life*", where useful life (or **lifetime**) is the "*time interval from first use until user requirements are no longer met, due to economics of operation and maintenance, or obsolescence*". Thus, the durability quantifies the useful life as time or number of cycles.

The peculiarity of a solar panel is that it has to perform outdoor for several years. Weather factors are multiple, and an accurate forecast of their synergistic effect on the long-term is not an easy task. Temperature and relative humidity variations, moisture and pollutants in the atmosphere, UV radiation, wind, hail, snow, and sand are some examples of climate stresses that can affect the PV module structure during operating time. As discussed in Section 1.3, a solar panel is composed of a variety of materials. Each component has a different weatherability and the failure of a single part can endanger the whole system's functionality.

The **performance degradation** of a PV module are typically evaluated and quantified by

measuring its **power loss** over time:

$$P_{loss}(t)[\%] = \frac{P_{nom} - P_{max}(t)}{P_{nom}} \cdot 100 \quad (1.3)$$

Where:

$P_{nom}$  is the initial maximum power of the module measured after fabrication;

$P_{max}(t)$  is the maximum power output evaluated at operating time  $t$ .

To compare the two values, modules are always measured at **standard test conditions (STC)**, i.e. irradiance of  $1000 \text{ W/m}^2$ , solar spectrum AM1.5G, and temperature of  $25^\circ\text{C}$ . More details on module performance characterization are given in Chapter 2. Excluding catastrophic events, a PV module power output is unlikely to drop to zero. However, there is a minimum generated power threshold value below which a PV module is no more economically viable to be maintained operational.

Today, c-Si PV module manufacturers generally give a **performance warranty of 25 years** of operation in the field, ensuring **80% of the nominal power**. A common degradation rate is expressed with a linear power reduction of  $0.8\%/year$ . Nevertheless, some companies provide different degradation as for example, Sun Power company [33]. These figures are based on data recorded during years of outdoor exposure. However, an accurate evaluation of the performance degradation on the long-term requires a systematic collection of data from the field for 25 years. This is a time-consuming task, especially when it is done for each new module design. One solution is to use **outdoor data** and **to develop indoor tests** which reflect the same degradation scheme seen in the field in a reasonable time. **Qualification standards** for PV modules have been designed with this aim in mind. They are based on a series of aging tests that PV modules are subjected to identify potential failure modes occurring during operation.

### 1.4.1 Degradation modes

In reliability engineering, system failure rates over the operation time can be described by the bathtub curve (see [34], or [35]). The concept is to identify three different stages during the system operation lifespan:

1. **Infant mortality stage:** this occurs during the initial period of usage and shows the highest failure rate. Main premature failure causes are attributed to defective items after the production.
2. **Mid-life failure stage:** during this period, failures occur randomly at a constant low rate.
3. **Wear-out failure stage:** this happens in the late operation time interval. The failure rate increases again.

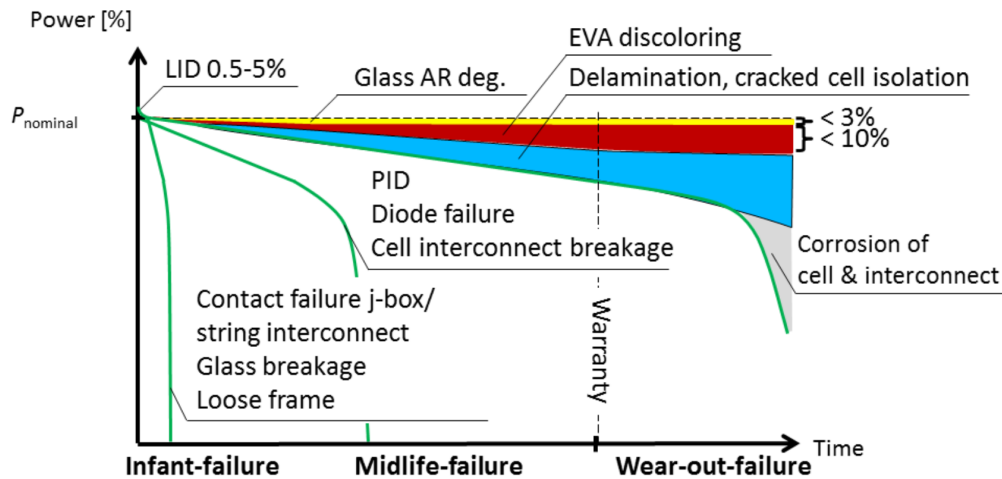


Figure 1.8: Three typical failure scenarios for c-Si modules. Image taken from [23]

The related chart for PV modules is presented in the report from IEA on PV module failure modes in the field [23], and shown in Figure 1.8. Failure rates are reported as power reduction with respect to the initial nominal power.

1. Infant failures occur at the beginning of the outdoors exposure of a PV module. The main causes are **manufacturing defects** of the module, transportation, or installation. Junction-box failures, glass breakage, defecting cell interconnects, and loose frame are the most common among others. Light-induced degradation (LID) does not count as a failure mechanism, as the module power stabilizes after initial exposure (weeks or months) to sunlight.
2. Failures relative to the midlife of PV modules (e.g during the first 10 years of installation) are related to an **non-optimized bill of materials (BOM)**. They are described in a study by DeGraaf [36] identifying ribbons and interconnects detachment and glass defects (e.g. anti-reflecting coating delamination). More recently, Eder [37] also showed cracks formation in polyamide (PA) back-sheets.
3. Wear-out failures occur after many years of deployment, as a result of **material degradation** caused by weathering agents (such as moisture ingress, UV radiation). Mainly, encapsulant chemical degradation is responsible for the yellowing, loose adhesion (e.g. delamination), and interconnection lines corrosion. Wear-out failures determine the maximum lifetime of PV modules.

### Commonly observed PV module degradation mechanisms in the field

The field degradation of PV modules can be classified into five categories [38]:

- **Degradation of packaging materials** such as glass breakage, discoloration of the encapsulant, and back sheet cracking;
- **Loss in adhesion strength** or delamination. Field experience has shown delamination on the front side of the module is more common than the backside. This can also cause optical decoupling and prevent effective heat dissipation. Module reliability is inextricably related to the cohesion and adhesion of all material layers in the module [39];
- **Degradation of cell/module interconnects;**
- **Degradation caused by moisture ingress**, which causes corrosion in metallic parts and increases current leakage. Moisture permeation also results in delamination;
- Degradation of the semiconductor devices.

### 1.4.2 Qualification standard tests

Since 1975, PV manufacturers and research laboratories have put considerable effort into developing accelerated stress tests for terrestrial PV modules to answer the fundamental question: "*How long will encapsulated stringed cells be able to deliver power?*". The main idea of indoor aging tests is to replicate the PV failure modes observed in the field in a lower time interval. The adopted strategy can be resumed in the following three tasks:

- Identify different failure modes occurring in the field;
- Identify stress factors that cause the failure;
- Determine the accelerating factor to replicate the same failure pattern by means of indoor tests.

This effort resulted in developing specific stress test series approved by the International Electrotechnical Commission (IEC), aiming to provide a minimum level of product quality. As a matter of fact, these tests are the only ones accepted by both module manufacturers and buyers.

Depending on the solar module type, we can distinguish three main standards. Since **this thesis focuses on c-Si PV modules**, the related standard is the **IEC-61215 for Crystalline Silicon Modules** [40]. It includes thermal stress tests, such as damp heat (DH), thermal cycling (TC), humidity freeze (HF), UV preconditioning, and mechanical tests such as mechanical load and hail test. In Table 1.1 a short description of single tests is given, with the related potential failure mode to reproduce.

This standard incorporates a strict "pass/fail" criterion which allows manufacturers to demonstrate the degree of performance [42]. The module gets certified if:

## Chapter 1. Introduction

Table 1.1: Examples of the most-demanding aging tests contained in IEC 61215:2016 with corresponding failure modes that each test aims to reproduce. Table adapted from [41]

Test	Conditions & Description	Potential effects and field failure modes
damp heat	Exposure to constant temperature of 85°C and a relative humidity of 85% for 1000 hours, to evaluate the effect of prolonged exposure to high humidity and potential water penetration	Delamination, solder bonding failure and encapsulant discoloration.
Thermal cycling	Exposure to 200 of temperature ramp cycles from 85 to -40°C, to evaluate possible thermal mismatches between module's component. At temperatures $T > 25^{\circ}\text{C}$ , the module maximum current flows through the module.	Delamination, junction box failure, broken interconnections, solder joint failure and cell breakage.
Humidity freeze	Exposure to temperatures cycling between 85°C with relative humidity of 85% and -40°C, to evaluate module's resistance to the effect of high and low temperatures and humidity. During the tests the module has a continuous current flow	Delamination, junction box failure, broken interconnections, solder joint failure and cell breakage.
Mechanical Load	The module is loaded on the front side with 2400/5400 Pa for 1 hour and afterward with -2400/-5400 Pa for another 1 hour (x3 times). It determine the stability of the module in presence of snow or wind.	Structural failures, glass damage, broken interconnections, cell breakage, solder bonding failure.
UV pre conditioning	Exposure to constant temperature of $60 \pm 5^{\circ}\text{C}$ and UV light source (with a specif intensity spectrum) up to a cumulative UV dose of 15 kWh/m <sup>2</sup> . It evaluate the stability of UV sensitive module's components(i.e. polymeric materials)	Encapsulant and backsheet discoloration, delamination.
Hail test	The module is shot in several positions with ice balls of specif diameter range (i.e. 25–75 mm) and velocities (i.e. 23–39.5 m/s). It verify the resistance of the module to impact of hail.	Cell breakage, glass damage.

- After each test sequence, the maximum power output drop is less than 5% with respect to its initial  $P_{nom}$ ;
- There is no visual evidence of major defects (yellowing, delamination, corrosion, bending);
- The insulation (dry) and wet leakage current test requirements are met at the beginning and the end of each sequence.

Qualification tests help identify materials that lead to potential failures after installation and establish a certain quality to PV modules. However, they are sometimes mistakenly taken as predictive lifetime tests. As specified in the IEC 61215 standard, these tests aim at showing “*that the module is capable of withstanding prolonged exposure in general open-air climates. The actual lifetime expectancy of modules so qualified will depend on their design, their environment and the conditions under which they are operated.*” (cit. from [40]). During the last years, some advances in stress testing came out, such as IEC 63209, IEC 62788, or other combined/sequential testing procedures, beyond the IEC 61215.

### 1.4.3 Lifetime prediction complexities

An accurate evaluation of the service lifetime of a PV module after its installation is one major topic in the reliability field. For simplicity, the **lifetime of a PV module** often coincides with the performance warranty conditions given by the producer (see Section 1.4). It can be then defined - arbitrarily - as the time required for a PV module to lose its nominal power by 20% (so-called degradation limit) [44]. A precise estimate of how performances will degrade over time is crucial to narrow uncertainties in the LCOE estimates. However, this is not a straightforward task, and many diversified variables need to be considered.

In most of the cases, degradation rates used to forecast the module lifetime are based on available data recorded from **old installations**. However, there is no direct correlation between the components and **materials used** for the specific PV system. The importance of the BOM during real operation was assessed by Virtuani and Annigoni [45, 46]. They conducted a detailed study on a 35-year installed PV system in Switzerland. The main finding reveals how the module performance varies depending on the encapsulant used. Figure 1.10 shows the appearance of three aged modules from the same PV installation: the encapsulant discoloration level is due to the use of the same based polymer (i.e. Polyvinyl butyral, PVB) but supplied by different companies. The use of a quality encapsulant material resulted in a reduction of performance of less than 5% after 35 years in the modules manufactured with a proper encapsulant. The module manufactured with sub-optimal encapsulants clearly showed higher degradation rates. This witness the importance of adopting a 360° approach to quality, which includes material and supplier qualification, proper module design, and the development of accelerated aging tests to ensure the extended service lifetime of PV modules.

All recent developments listed in Section 1.3 refer only to main module components; never-

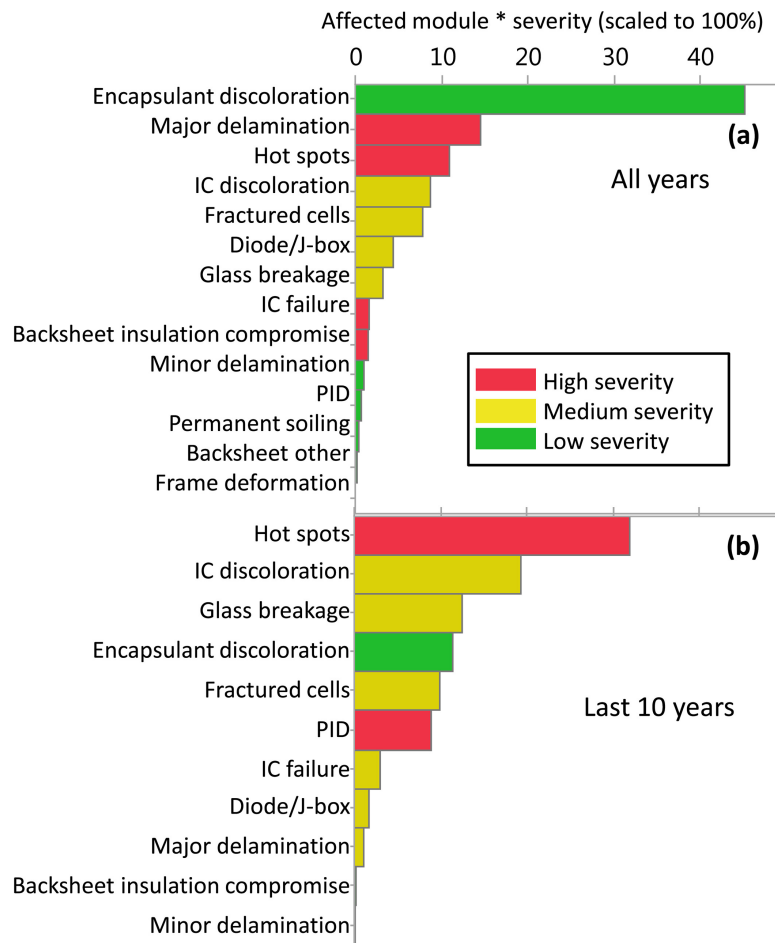


Figure 1.9: Pareto chart of the most significant degradation modes for (a) systems installed more than 20 years ago and (b) systems installed in the last 10 years. Image taken from [43].

theless, they are already good indicators regarding the fallacy of comparing different module types. The constant change of the failure mode scenario with the module technology is also visible in Figure 1.9 showing how the percentage of detected degradation modes has changed during the years.

The limited outdoor track record of new PV modules put more attention on interpreting the output of the qualification standard tests. However, these tests cannot be used as service life prediction (SLP) tests since **an acceleration factor is difficult to find**. Their major limitations are:

- They are not climate-specific. The IEC 61215 sequence is unique. The module can pass the test, but its behavior during operation strictly depends on the climate conditions (i.e. temperature variations, UV dose, humidity, dust, and soiling,...);
- They are single-stress tests. One major criticism is the risk of developing new compo-

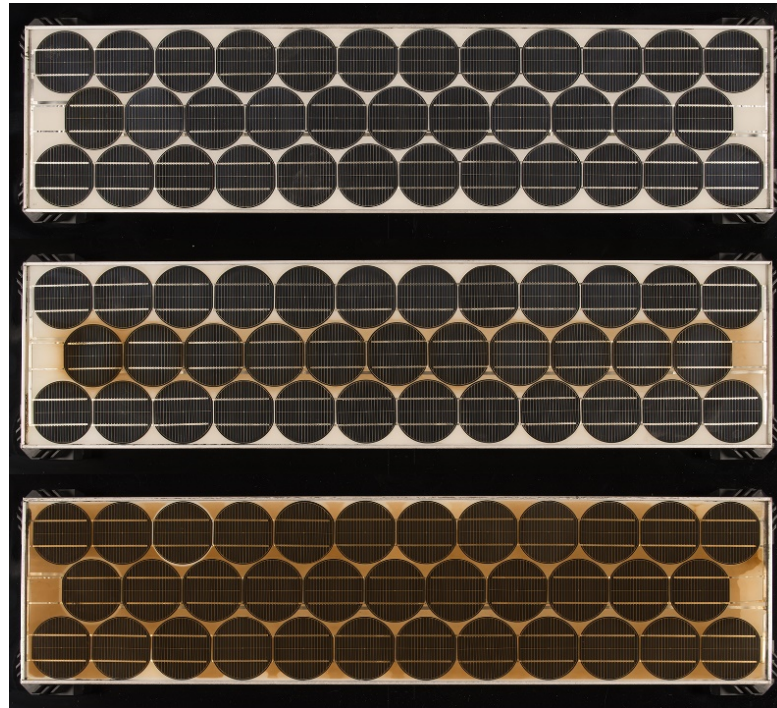


Figure 1.10: Visual inspection performed on three different classes of module coming from the same PV installation with 35 years of useful service lifetime. From top to bottom, the polymer yellowing becomes stronger and has a higher impact on module performance. All modules were fabricated using PVB as an encapsulant but supplied by different producers. Image taken from [46].

nents to withstand better during indoor test. However, the synergistic action of multiple stresses during real operation can lead to unforeseen failures [37];

- The increase of one (or more) climatic stressors can lead to unrealistic failure modes to occur. For instance, too high temperatures are not realistic. It is difficult to find an Arrhenius dependency for the RH. The use of UV sources that do not match the solar spectrum can trigger degradation modes that will never occur during outdoor exposure.

Recently, new test series are proposed with simultaneous application of multiple stresses. DuPont [47] developed a module-accelerated stress test (MAST). In this way, they could reproduce backsheet failure that occurred in field installations that were not reproduced during the IEC standard tests. Another example is proposed by NREL [48] with the combined-accelerated stress test (C-AST). The idea is to employ **combined and/or sequential stress protocols** to better show PV module weaknesses by applying stress intensities that are not unrealistic or unobservable in the natural environment [49]. The potential value of these new protocols is an important step toward a more realistic accelerated lifetime test for PV. However, the adoption of this test series may requires the application of considerable modifications to a commercial climatic chamber.



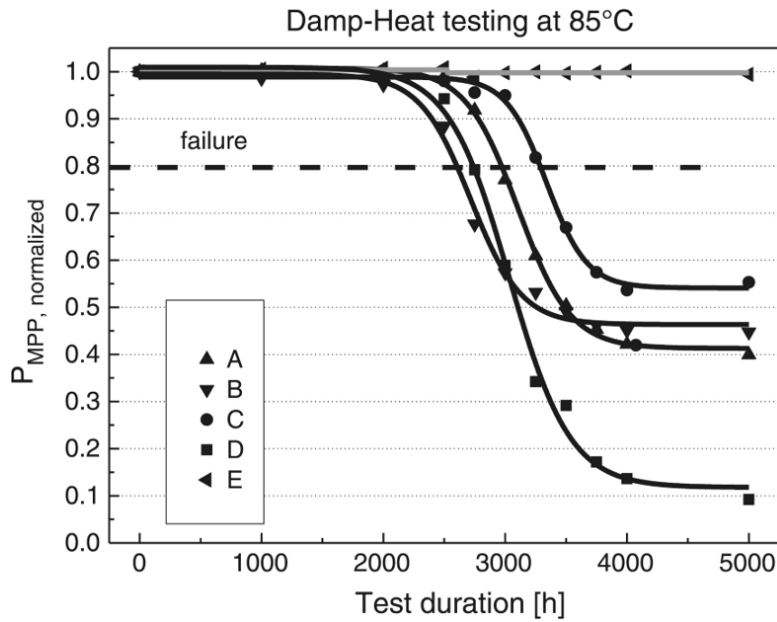


Figure 1.11: Normalized power of the five different PV module types tested in damp Heat conditions (85°C and 85% RH) as function of exposure time and fitted degradation curves. The test duration of this work extends up to 5000 hours, compared to the conventional 1000 hours contained in the IEC standard. The chart is taken from [51].

**Extend the duration of a standard test** can be a more straightforward solution, practical to compare the stability of two modules with different BOM, i.e. different encapsulant suppliers. An example is shown in Figure 1.11. The power degradation of the same module types is very similar after the 1000 hours of damp Heat test, as prescribed by the IEC 61215 standard. Since the power loss is lower than 5% of the initial value, all modules passed the test. However, if the test is extended beyond the classical 1000 hours, the power loss of the specific PV module is different. Hence, such modules might perform differently after field exposure. Extended stress testing is described in the recently drafted IEC TS 63209 [50] which *"provides a standardized method for evaluating longer term reliability of photovoltaic (PV) modules and for different bills of materials (BOMs) that may be used when manufacturing those modules"* (cit. from [50]).

## 1.5 The role of the encapsulant

In Section 1.3 we listed the different module materials. Specifically, the encapsulant is the polymeric foil that acts as the intermediate layer to glue all single components "at one" through the so-called lamination or encapsulation process. The final quality of the module, i.e. after the lamination step, and its stability during field operations are strictly linked to the encapsulant properties obtained during the lamination step (as already shown in Figure 1.10).

### 1.5.1 Material selection

The encapsulant is a polymeric material characterized by its glass transition temperature, melting temperature, creep resistance, optical transparency, etc. To fulfill the requirements as PV encapsulant, a list of specific properties is given by Czanderna in [52]. The main functions of the encapsulant for PV applications can be resumed as follow [52,53]:

- Provide mechanical support to the module lay-up and positioning of the stringed solar cells;
- Provide good physical isolation from environmental degrading elements (such as moisture and pollutants) of the solar cells during field operation;
- Assure optical coupling between the solar cells and the front glass to maximize the power output of the module;
- Guarantee the electrical insulation between the solar cells and circuit elements of the module during operation.

An extensive material screening was conducted already in the 1970s by the Jet Propulsion Laboratory (JPL) to find suitable candidates for the use in PV modules. Historically, the first adopted material was a polydimethylsiloxane (PDMS) formulation [54], chosen because of its optical properties, processability, stability at usual module operating temperature (i.e. 60°C) and resistance to UV radiation [55]. However, PDMS were too expensive to use for large-scale terrestrial applications, and thereby, alternative materials were investigated and developed, leading to the emergence of ethylene vinyl acetate (EVA) [56]. Currently, the share market of EVA still takes up more than 80% [30]. Alternative polymers used as encapsulants are PVB, silicones, and Ionomers. Still, EVA, despite not being an optimal material, has a proven track record over multiple decades, acceptable costs, easy processability, and an overall good price-quality ratio.

### 1.5.2 EVA formulation

EVA is a random co-polymer of ethylene and vinyl acetate (VA) as shown in Figure 1.12, chemically synthesized via a radical polymerization process. The use of EVA for industrial applications is wide because its properties can be easily tailored by simply adjusting the VA content [57]. Increasing the VA percentage makes the material more amorphous (e.g. disruption of the crystalline polyethylene segments); consequently, the transmittance and flexibility properties tend to improve. For PV applications, the usual content of VA is around 33%. This chemical composition demonstrated good transmittance, thermal stability, and mechanical properties after UV aging experiments [58].

The first available EVA formulation for PV application was developed at the Springborn laboratories in 1978, under the name A9918 [59]. As reported in Table 1.2 the base material was the

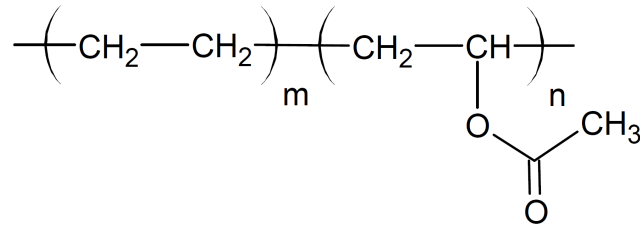


Figure 1.12: The chemical formula of the EVA encapsulant.

Table 1.2: Formulation of the First Generation EVA Encapsulation Film, designated A-9918 [59].

Component	Role	Composition (Part by weight)
EVA (Elvax 150, DuPont)	polymeric resin	100
Lupersol (peroxide) 101	cross-linking agent	1.5
Naugard-P	antioxidant agent	0.2
Tinuvin 770	UV stabilizer	0.1
Cyasorb UV-531	UV stabilizer	0.3

EVA Elvax150, with a VA content of 33%. Since EVA itself is a thermoplastic polymer with a soften temperature of 70°C, Springborn developed a cure system by introducing a thermally activated peroxide-based cross-linking agent (Lupersol 101) along with other additives to improve the weather stability of the material (such as antioxidants, UV absorbers, and UV stabilizer agents) without affecting the optical properties. During the years, the EVA formulation has been further optimized in order to improve the outdoor stability by for example, replacing the Lupersol 101 with the Lupersol TBEC (to reduce the discoloration rate of the EVA) [60], and the addition of hindered amine light stabilizers (HALS) to prevent the photo-degradation of the UV stabilizers [61].

### 1.5.3 The lamination process

The fabrication step during which the encapsulant foils melt and the curing agent is thermally activated to provide the adhesion between elements and the rigidity to the structure is called lamination or encapsulation process. The quality of this process – and the adoption of the proper temperature and pressure profiles - is critical in ensuring a long service lifetime of the final product. Once the module assembly is ready (i.e. all the different elements are neatly stacked), it is placed in a flat-bed vacuum bag laminator. A typical laminator is divided into two chambers (i.e. upper and lower) and separated by a flexible rubber membrane. The lower chamber is equipped with a heating plate and metal pins that can be lifted up and/or retracted to adjust the heating rate of the module lay-up [62]. During the encapsulation process, temperature (T), pressure (p), and time (t) parameters are specifically varied and controlled

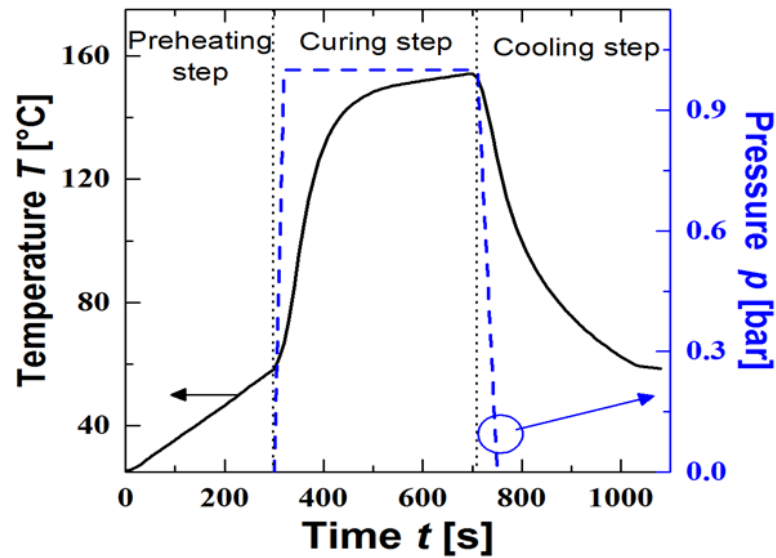


Figure 1.13: The temperature and pressure profiles during a typical encapsulation process of PV modules.

to match an ideal lamination profile (T-p-t profile). Figure 1.13 illustrates a conventional PV lamination profile. Typically, three main stages can be identified:

1. **Preheating** – the pins are lifted up to avoid thermal shocks between the module lay-up and the hot-plate. This stage aims at reaching the softening temperature of the encapsulant (around 60°C) while out-gassing the air present in between the frontsheet and backsheet to avoid the formation of bubbles;
2. **Curing** – The silicone diaphragm is filled with air to reach a certain pressure in the upper chamber. This allows the softened encapsulant to "wet" the entire module parts and provide good adhesion. At the same time, the pins are retracted to let the module heat up and reach the curing temperature (around 150°C) and initiate the encapsulant curing process; The peroxide cross-linking agent is activated and depleted to generate chemical bonds between the polymeric chains of the EVA. This step takes between 300 and 900 seconds in order to reach a cross-linking value (or gel content) > 80% ;
3. **Cooling** – the laminate is moved to a second chamber maintained at a certain cooling temperature. Simultaneously, a pressure of 1 atm is applied to the laminate - by means of a rubber membrane - to avoid warping of the module stack. The main purpose of this last - optional - step is to minimize bowing and to prevent edge delamination.

### 1.5.4 Causes and effects of EVA degradation

The weathering of the PV module can affect the properties of the polymeric and other materials. Outdoors stress such as UV radiation, moisture and temperature variations can trigger degradation reactions such as UV photo-oxidation, thermal oxidation, and hydrolysis.

Polymers are, in general, prone to UV-induced degradation. In a PV module, the front glass has a UV cut-off wavelength of 320 nm, meaning that it absorbs most of the high energetic UV-B rays (280 – 315 nm) coming from solar radiation. The remaining portion of the UV spectrum (i.e. UV-A, 315 – 390 nm) is transmitted to the rear layer, i.e. the polymeric encapsulant. However, a pure EVA resin film does not absorb the UV-A [63]. Nevertheless, the EVA formulation used for PV application is prone to **discoloration** (i.e. yellowing or browning) that occurs after certain years of outdoor exposure. A remarkable example of this problem is the case of the Carrisa Plains PV power plant [64]. The 5.2 MW installation was completed in 1985 with PV modules encapsulated with EVA. After only 4 years of field operation, much sooner than the designated 20-year lifetime, the power output was less than the 70% with respect to the original nominal value. The primary failure modes observed in this case were a severe **EVA browning and the production of acetic acid** with the consequent reduction of the incident light intensity reaching the cell top surface, and the corrosion of the metallic interconnection due to acidic pH level, respectively. Since the outburst of similar cases in different locations, the EVA yellowing/browning problem has attracted broad research interest.

The main cause of fast discoloration of EVA is attributed to the presence of chromophoric species in the polymer. Chromophores can be generated during UV exposure due to residues of unreacted peroxide catalyst as a result of a **non-optimal lamination process**. As shown by Pern, a partially cured EVA shows faster yellowing compared to an optimally cured one [60]. Additives and curing agents that reduce the generation of chromophores lead to a lower discoloration rate of the encapsulant [61, 65, 66].

UV absorber additives are usually added to the EVA formulation to reduce the UV light absorption by the chromophores. However, the UV absorber itself degrades during UV exposure. Once it is completely consumed, the chromophoric species are directly exposed to the UV radiation, leading to a complete photo-degradation. Moreover, degraded UV absorbers can initiate the decomposition of EVA chains leading to a faster material browning [60]. To tackle this issue, HALS are added to prevent the degradation of UV absorbers. Additionally, in the case of a glass-backsheet (G-BS) structure, the breathable rear sheet allows oxygen ingress. The presence of oxygen helps eliminate active free radicals, therefore stabilizing the UV absorbers [67] through a photobleaching reaction as opposed to the discoloration. Photobleaching is then dominant at the edges of the module and in between adjacent solar cells compared with the center of the cell where the oxygen diffusion is limited [68]. An example of the discoloration difference between the edges and the center of solar cells in a G-BS PV module is shown in Figure 1.14. The pathways for yellowing/browning process of EVA are recalled in Figure 1.15.

The thermal activation of the curing agent during lamination requires temperatures of 145-



Figure 1.14: Picture of a glass/back-sheet PV module highlighting the different discoloration intensities depending on the position. [69].

155°C. In this temperature range, the thermal degradation of EVA occurs, and acetic acid (HAc) might be generated in the laminate [71]. The synergistic action of UV radiation and moisture/oxygen ingress during outdoor exposure can accelerate the degradation reaction rate. The degradation of the EVA through Norrish type reaction is well documented in the literature [52, 53, 65, 72]. Figure 1.17 shows the possible chemical reactions that EVA undergoes under extended UV exposure [58]. The deacetylation (i.e. from Norrish type II reaction) is catalyzed by acetic acid: the higher the concentration of HAc, the faster the initial deacetylation reaction. Other degradation products formed during the oxidation process (i.e. Norrish type III reaction) are  $\alpha, \beta$  unsaturated carbonyl compounds and hydroperoxides. In the presence of moisture, the hydrolysis reaction of VA units can occur, as reported in Figure 1.16.

Additionally, the presence of **water inside the module** (due to the non-ideal water vapor transmission rate of EVA), can lead to other failure modes that may impact the long-term performance and reliability of the module:

- The water ingress can **lower the adhesion** properties of the EVA to the glass, solar cells, and metal interconnected and can lead to delamination between different layers in the module lay-up. Additionally, the presence of an air interface between the EVA and the cell/front glass may reduce the light transmission;
- Water that diffuses through the EVA can also bring along **dissolved metal ions** from the glass (i.e.  $\text{Na}^+$ ) and/or the corroded metallic electrical connections at the cell surface ( $\text{Pb}^{++}$  or  $\text{Cu}^{++}$ );
- The co-presence of moisture and the acetic acid locally reduces the pH on the surface of the cell with a **corrosive effect** on the metal interconnection lines. This increases the

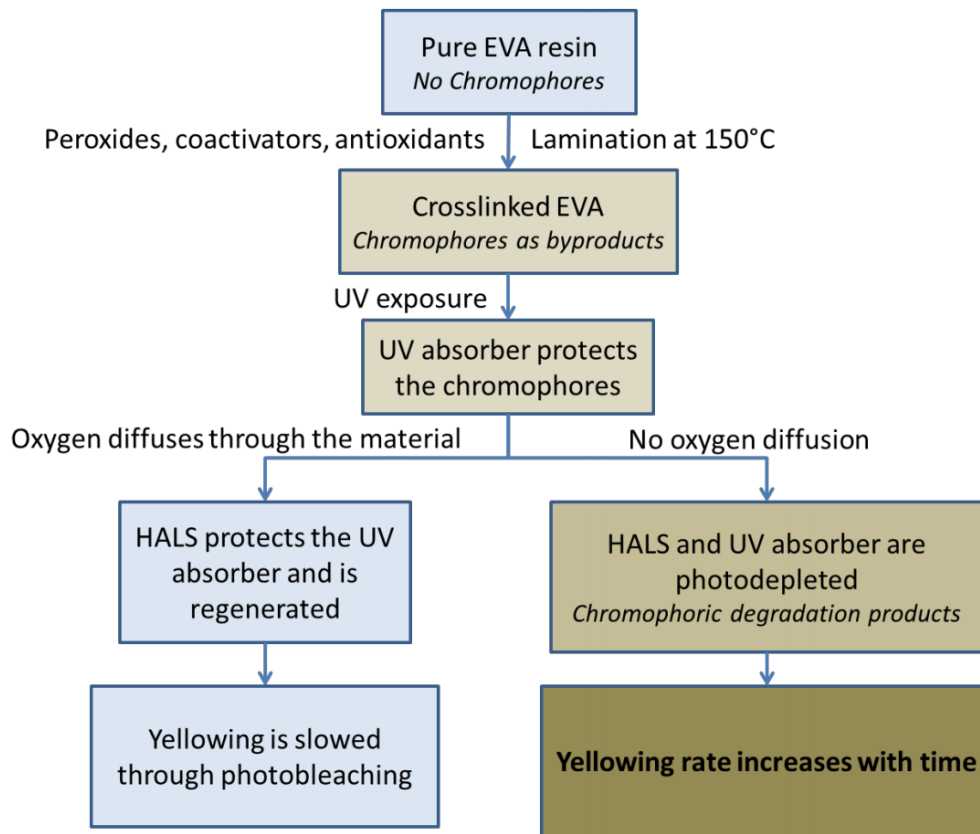


Figure 1.15: Schematic diagram of degradation pathways of the yellowing process in an EVA-encapsulated PV module. [70].

series resistance of the module and the consequent power output reduction.

However, in conventional glass/back-sheet structures, the partly breathable polymeric back-sheet allows the out-diffusion of HAc from the rear cover, mitigating its concentration. Simultaneously, it allows oxygen ingress, which, thanks to photo-bleaching, mitigates the problem between cells and the module's edges.

When the structure does not allow the out-diffusion of HAc, such as in a double glass lay-up or when a thin aluminum plate is present in the BS stack, the degradation of the EVA may be more severe.

## 1.6 The potential of the glass-glass PV module layout

PV modules with a glass-glass (G-G) have been previously used mostly for thin-film PV technologies [62] and BI-PV products. Nevertheless, this structure is gaining momentum in the last few years thanks to the rise of the bifacial c-Si cells technologies, as reported in Figure 1.18. The use of bifacial cells in a glass-glass structure in fact, allows the realization of bifacial

## 1.6 The potential of the glass-glass PV module layout

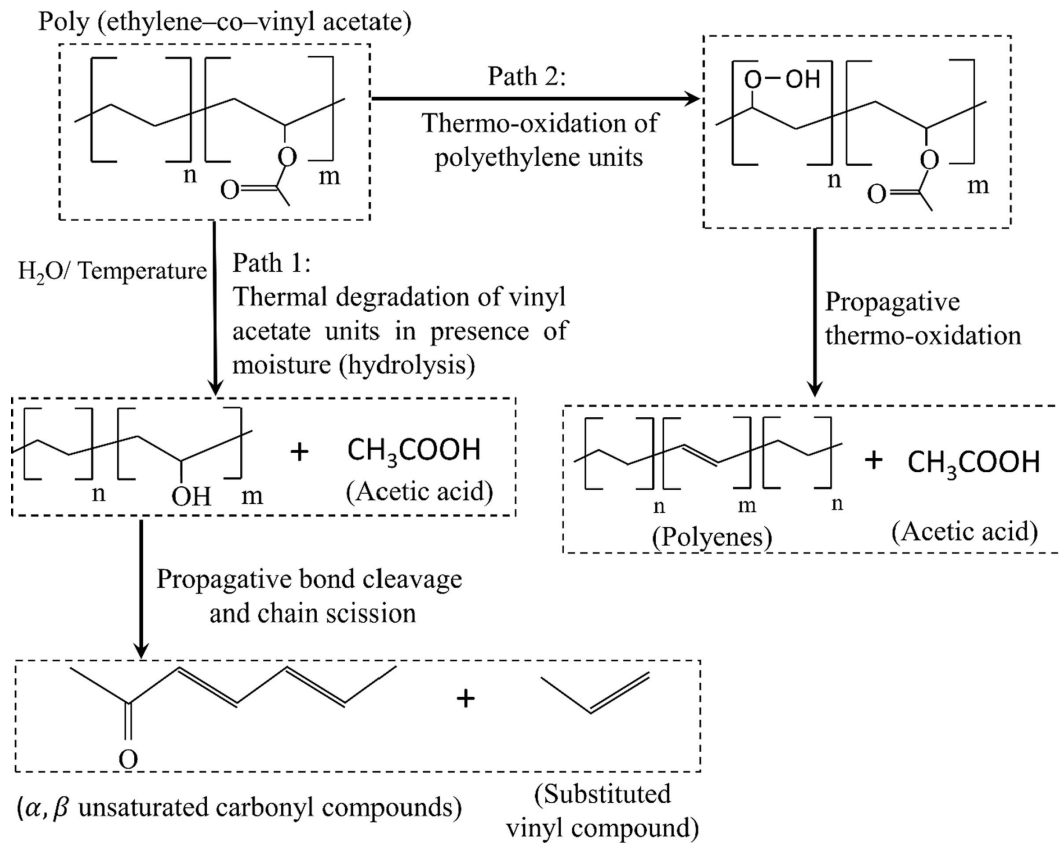


Figure 1.16: Structural degradation mechanism in EVA due to moisture and temperature [73].

modules, which lead to higher energy yields compared to mono facial PV modules (up to 6-10%) [74] thanks to the collection of reflected light from the rear side. The energy yield gain also depends on the cell technology, as recently reported by Wang *et al.* [75].

The use of a double glass structure is a good leverage to reduce the LCOE values of the PV technology:

- The production costs of G-G and G-BS modules are comparable.
- The replacement of the standard opaque polymeric back-sheet with a second glass plate allows the absorption of the albedo fraction of the light reflected and diffused back from the ground. The albedo depends on the type of ground. This added *chance* of the light collection is beneficial to improve the current and the power generated by the bifacial module [77].
- The rear glass plate improves the mechanical stability and the physical insulation of the final module laminate. This directly affects the durability and useful life of the PV module.

However, there are some limitations to obtaining a detailed LCOE that uniquely determines if



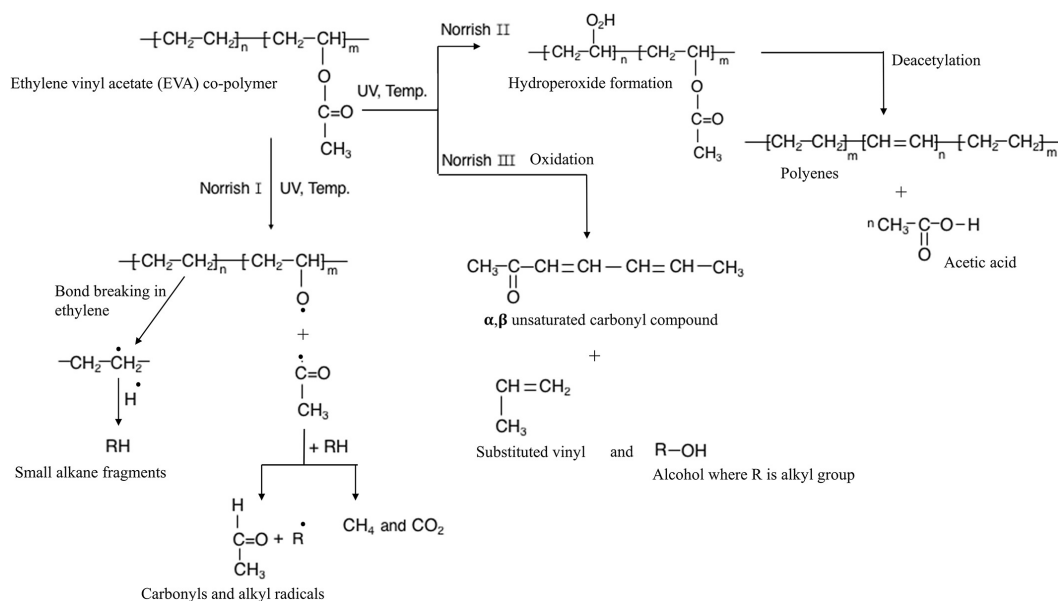


Figure 1.17: Structural degradation mechanism in EVA under UV irradiation [58].

the best solution is a mono-facial or a bifacial installation, as reported by Rodriguez-Gallegos *et. al* [78]: variables such as geographical zone, optimal til angle, and land price need to be evaluated for each particular case. The case of bifacial modules installed with single-axis trackers is the most interesting solution, reaching the lowest LCOE in almost all sites. Nevertheless, some drawbacks of G-G modules structures exist:

- The higher weight of G-G modules impacts the transportation and installation costs. The most significant contribution to the weight of a solar panel is that of the glass sheets.
- To maximize the potential of the rear active surface, the positioning of the PV system must be optimized, and a certain distance between two adjacent rows is needed (typically 6-8 meters). This increases the amount of land area required [79].
- There is a lack of data from field installations compared to conventional G-BG layout [29] and the energy yield modeling for bifacial modules is not yet a straightforward process.

To overcome the former issue, polymeric transparent back-sheets [80] and thinner glass covers can be potential solutions.

The track record and number of field installations with data for G-G modules are limited compared to conventional G-BG. In the literature, we found two main publications related to inspections of 10 to 20 years-old double glass PV modules installed in Arizona (i.e. hot & dry climate). Patel *et. al* [81] compared the power loss of G-G and G-BG modules encapsulated with EVA and observed that G-G modules are more prone to discoloration and thereby they suffer higher performance losses than G-B modules after only 10 years of outdoor exposure.



Figure 1.18: Cumulative installed bifacial PV capacity from 2012 to 2020. Image taken from [76].

Thorat *et. al* [82] also concluded that EVA-based G-G modules suffer from encapsulant browning, delamination, and interconnect corrosion, whereas modules encapsulated with Ionomer did not experience these failure modes. These results confirm that the use of EVA in G-G structures may be critical because of the high physical insulation of the whole lay-up. On the one hand, it prevents/mitigates the water ingress from the rear side; on the other, it reduces the oxygen diffusion - responsible for the browning attenuation as explained in Section 1.5.4 - and hinders the out-diffusion of generated acetic acid.

It is interesting to notice that diverging results come from indoor aging tests. Particularly, Tang *et. al* have shown that industrial Canadian Solar's double-glass PV modules, encapsulated by the use of an EVA formulation, passed 3 times extended qualification standard tests following IEC 61215 and IEC 61730 [83]. These results, published in 2017 confirm what we already explain in Section 1.4.3 about the difficulties encountered to accurately evaluate the service lifetime of PV modules using accelerated-aging test (i.e. the IEC tests typically do not involve UV and therefore there should not be any troubles with the encapsulant stability), and that the bill of materials plays a key role in the reliability of solar panels.

An exhaustive literature review on double glass PV module reliability has been recently published by SLAC and NREL institutes, concluding that "*the current state of G/G technology and the widespread efforts in materials characterization leads us to a positive outlook for increasing G/G deployment. With appropriate adjustments in G/G design and bill of materials, detrimental degradation processes can be mitigated. We expect G/G to enable longer lifespan and higher efficiency modules if scientifically-driven designs are implemented that counteract the reliability concerns*" [29].

### 1.6.1 Encapsulant alternatives for G-G modules

Different chemical formulations are under investigation to tackle acetic acid generation and provide more durable encapsulants. However, EVA remains the encapsulant choice for most PV module manufacturers. As recently reported by the PV magazine, the Chinese company Hangzhou First Applied Material. *"has secured exclusive patent authorization for anti-acid technology that makes it possible to reduce the degradation of solar cells by suppressing the generation of acid in EVA under ultraviolet sun rays"* [84].

A promising alternative to conventional EVA are the more recently developed **poly-olefines (PO)**. The main difference compared to the standard EVA formulation is that POs have **no vinyl acetate groups**, which are the main ones responsible for acetic acid generation during UV degradation. Additionally, POs have **higher volume resistivity and lower water vapor transmission rate** compared to EVA. These aspects are beneficial in preventing (or reducing) the potential induced degradation (PID) phenomena. Recent works done at PCCL research group by Oreski [31] and Barretta *et. al* [85] have compared the degradation of EVA and newly developed polyolefins showing the potential better stability of the latter under damp heat conditions and UV radiation. However, POs have the drawback of higher prices than EVA, and, somehow, a more difficult processability that needs to be carefully tailored.

## 1.7 Conclusions

Obtaining trustful scientific data is crucial to improving PV modules' reliability and competitiveness in the industrial market.

As described in this chapter, the vast improvements and development at different levels during the last decade have significantly increased the efficiency of a single panel. However, the rapid change of materials, configuration, and fabrication processes – and their introduction in the market - raises the question about the reliability and durability of these newly developed module concepts.

Understandably, we cannot wait 20 to 25 years to get the proper feedback from field modules. Meanwhile, we can improve our understanding and get insights on some crucial aspects of developing new indoor accelerated stress sequences and combining them with modeling.

Particularly, we decided to **focus on the glass-glass module designs in this work**. The rise of bifacial cells has boosted the fabrication and installation of solar modules with a double glass structure. This trend is deemed at continuing in the next years with an estimated market share for these modules of 30% by 2030 [30].

The concept is known since decades as it was adopted mainly in thin-film PV technologies. Nevertheless, c-Si-based solar cells cannot be compared with technologies such as amorphous silicon. The available data from outdoor installations are not exhaustive and do not incorporate newly developed module materials.

In this frame, a *hot topic* is the use of conventional Ethylene Vinyl-Acetate encapsulant in advanced crystalline–silicon-based glass-glass PV modules. Some manufacturers still rely on EVA because of its lower costs and easier processability. On the other hand, newly developed PO formulations are gaining attraction as they proved to be more stable than standard EVA. Drawbacks are the higher cost and an unknown track record from field installations.

**In this thesis we** will show results from different indoor aging tests attempting to understand the long-term degradation of EVA used to encapsulate G-G modules and **contributing to answering this question: “Is mainstream EVA still a prospective encapsulant for glass-glass PV modules?”**.

## 1.8 Structure of the thesis

The thesis is structured as follow:

- **Chapter 2** describes the materials used in this work, the different experimental methodologies, and characterization methods exploited in order to evaluate and study the observed degradation mechanisms.
- **Chapter 3** shows the results related to standard indoor aging tests run to understand how the relative humidity impacts the module performance losses of glass-glass modules encapsulated with EVA using different cell technologies, such as aluminium back surface field (Al-BSF), passivated emitter rear cell (PERC) and silicon heterojunction (SHJ). This first screening test helped us restrict the following work area and develop a more efficient experimental methodology.
- **Chapter 4** explains the root cause of the degradation mechanism of silicon heterojunction double glass modules encapsulated with EVA due to damp heat test aging conditions. We detail a microscopical model explaining the root cause behind the observed sensitivity to damp heat (and water ingress) of SHJ modules manufactured in a glass-glass structure using EVA. This degradation mechanism is specific to the SHJ technology, and we additionally describe ways to mitigate the degradation sensitivity of this technology to damp heat.
- **Chapter 5** focuses on the importance of the storage conditions of the uncured EVA rolls before their usage and the effect of potential trapped water in a G-G configuration during outdoor exposure, particularly the UV aging. Samples are subjected to a cumulative UV dose of  $630 \text{ kWh/m}^2$ , corresponding to 10 years of natural aging in a temperate climate in central European zones, such as Switzerland. From the observed results, we try to answer the following question: "can EVA be used in glass-glass PV modules?"
- **Chapter 6** proposes a new test developed to verify the stability of interconnection corrosion in the long-term exposure interval due to the degradation of the EVA and its consequent generation of acetic acid.

- **Chapter 7** resumes the relevant results obtained in this work and provides an outlook for follow-up activities.

### 1.9 Contribution to the research field

The work presented in this thesis leads to the following contributions to the research field of PV modules reliability:

1. We are the first to develop a detailed microscopical model explaining the sensitivity of SHJ cells/modules to damp heat (and water ingress). We highlight that this sensitivity depends not elusively on moisture ingress but on a reaction with the sodium ions ( $\text{Na}^+$ ) contained in the glass (which acts as a reservoir of Na). This degradation mechanism is specific to SHJ cells and is not observed in other cell technologies. Strategies to overcome this are discussed in detail.
2. We try to answer the question: "Can EVA be used in a glass-glass module structure?" We have demonstrated that the storage conditions of the uncured polymer roll play an essential role on the mid- to long-term stability of the module. Specifically, when the supplier's recommendations are carefully respected, EVA shows good stability under high UV doses. However, the combination of UV radiation and the presence of water trapped inside the impermeable glass-glass structure can lead to fast degradation of the encapsulant and the consequent premature failure of the module.
3. Corrosion is one of the main end-of-life degradation and failure modes in photovoltaic (PV) modules. Most module manufacturers will continue to use acid-generating EVA encapsulants in the near- to mid-term. However, all tests contained in IEC qualification standards cannot trigger corrosion - in a reasonable time scale. An accelerated aging test for acetic acid corrosion is developed to probe wear-out and end-of-life behavior and facilitate screening of new cells, metallization, and interconnection technologies. In all tests, lead oxides were the primary degradation products detected and found to accumulate mainly along the printed metallization, especially in proximity to the busbar. SHJ cells with a silver paste-based interconnection outperformed Al-BSF and PERC cells with a solder-based interconnection.

Our investigations agree with the challenges that the PV industry is currently facing. Our key findings could be helpful not only to the scientific community but also to the main industrial PV players.

The scientific contributions drafted and presented during the time of the thesis, are listed at the end of the manuscript.

The experimental methodologies and characterization techniques exploited for this purpose are described in the next chapter.

## 2 Experimental methods

### Summary

This chapter describes the main materials used to prepare the different sample designs employed during this work. The analytical techniques used to characterize some specific components and the evolution of material properties are also presented, along with the applied experimental methodologies.

### 2.1 Sample design & materials

The samples used in this work are divided in two different designs as schematically depicted in Figure 2.1:

1. The layout of the single-cell  $20 \times 20 \text{ cm}^2$  PV module was used to replicate - on a smaller scale - the commercial 60-cells glass-glass (G-G) module (with standard dimensions of  $1.0 \times 1.6 \text{ m}^2$ ). The PV stack consists of a front glass sheet/front encapsulating sheet (i.e. EVA)/soldered 6" solar cell/rear encapsulating sheet (i.e. EVA)/ rear glass sheet.
2. The  $10 \times 10 \text{ cm}^2$  glass/EVA/glass coupons were used to characterize the optical and chemical properties of the encapsulant and follow its degradation.

The significantly reduced size of the samples used in this work - compared to a standard c-Si module - it is more of a worst case for some of the experiments. Particularly, when evaluating the degradation mechanism due to the water ingress, as the diffusion time for a standard module will be clearly longer compared to the single-cell sample used in this work.

#### 2.1.1 Front and back cover glass

The front and back cover glass was a SOLARFLOAT HT soda-lime glass with the following specifications:

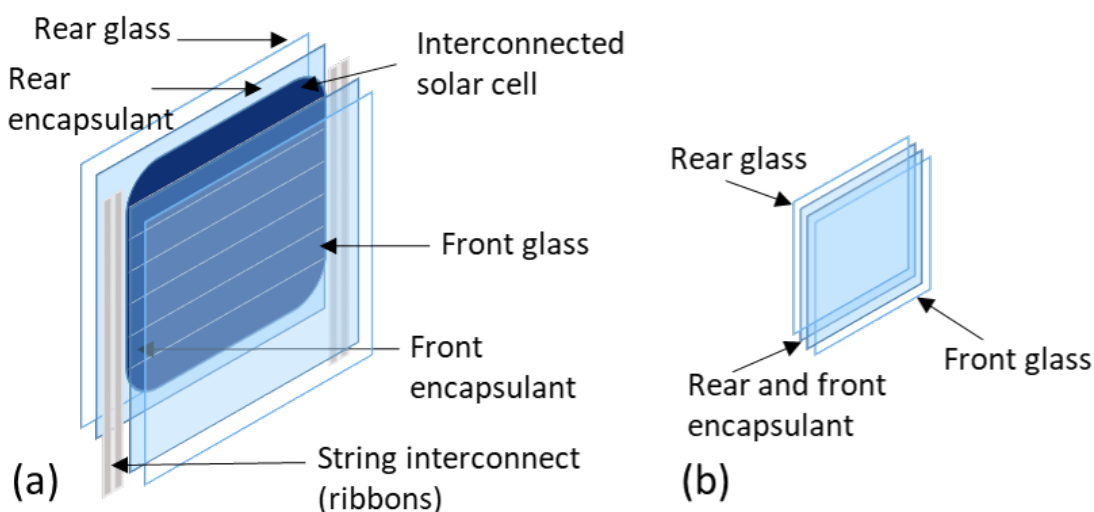


Figure 2.1: Schematic representation of the 2 main sample designs fabricated in this work: (a) 20 x 20 cm<sup>2</sup> single-cell module, and (b) 10 x 10 cm<sup>2</sup> glass/EVA/glass coupon.

- Plate dimensions: 600 mm x 600 mm x 3.2 mm (L x W x H);
- Heat strengthened glass;
- Optical transmission:  $\sim 91\% \pm 0.5\%$  from 350 to 1200 nm (see Figure 2.7 at the end of this chapter);
- Does not contain heavy metals.

A typical composition of this glass is 70–75 wt% SiO<sub>2</sub>, 12–16 wt% of Na<sub>2</sub>O, and 10–15 wt% CaO. The glass plates were cut with a glass diamond cutter into squares to fit the different sample geometries.

### 2.1.2 Solar cells

Different types of industrially available 6" solar cells were used. Particularly:

- Monofacial Al-BFS p-type, front emitter with 5 busbars from Canadian;
- Monofacial PERC p-type, front emitter with 5 busbars from Jinko Solar;
- Bifacial SHJ n-type, rear emitter with 4 (and 5) busbars, fabricated by CEA (commissariat à l'énergie atomique et aux énergies alternatives).

### 2.1.3 Metallization

Depending on the type of cell, different soldering materials and methodologies were used:

---

## 2.2 Tools for characterization of module and cell performance

- The Al-BFS and PERC cells were both manually soldered at 370°C by using a SnAg coated copper ribbons. The cell interconnects had a dimension of 1.5 mm x 0.2 mm, and string ribbons 5 mm x 0.2 mm.
- The SHJ solar cells required a low-temperature soldering to avoid damaging the passivating *a-Si* layers. A low-temperature electrical conductive adhesive (ECA) paste was used to glue the cell ribbons onto the busbars. CEA developed the specific ECA formulation, and SHJ cells were delivered already soldered.

### 2.1.4 Encapsulants and edge sealant

The same commercial EVA formulation was used for all the experiments, if not specified otherwise. The uncured roll was the F406S type from the Chinese company Hangzhou First. The optical and chemical properties of the encapsulant after the lamination process are shown later in Figure 2.5. The lamination temperature was set as 150°C as indicated by the producer.

To decouple the effect of the moisture - one of the main environmental stressors for PV modules - and its accumulation in a module, some tests were performed on a set of single-cell modules with the addition of an edge seal (ES). The commercially available sealant roll was commissioned from HelioSeal, specifically PVS 101 reactive desiccated solar edge sealant (1.2 mm x 8 mm). The ES is cut into strips of 20 cm and placed all around the module perimeter. Additionally, two small strips are put on top of the front ribbons extending outside the laminate to have a complete edge coverage.

## 2.2 Tools for characterization of module and cell performance

### 2.2.1 Current-voltage (I-V) measurements

The fundamental electric characteristics of a PV module are evaluated by means of current-voltage (I-V) measurements. The I-V curve is generated by scanning a voltage in a specific interval, across the solar cell and recording the generated current out-put for each voltage value. The punctual product of the voltage and the corresponding current gives the correlated power-voltage (P-V) curve [86], often displayed in the same graph along with the I-V characteristic. The direct comparison of different PV modules is possible when this measurement is performed at standard test conditions (STC) as defined by IEC 60904-3:2016 [87]: *the module is at 25°C, illuminated by a simulated light with an intensity of 1000 W/m<sup>2</sup>, with AM1.5G being the reference solar spectrum.*

In addition to the power out-put, other important module parameters can be extrapolated/-calculated:

- The open-circuit voltage ( $V_{oc}$ ): the maximum voltage reached by the PV module, when the current in the solar cell is zero.



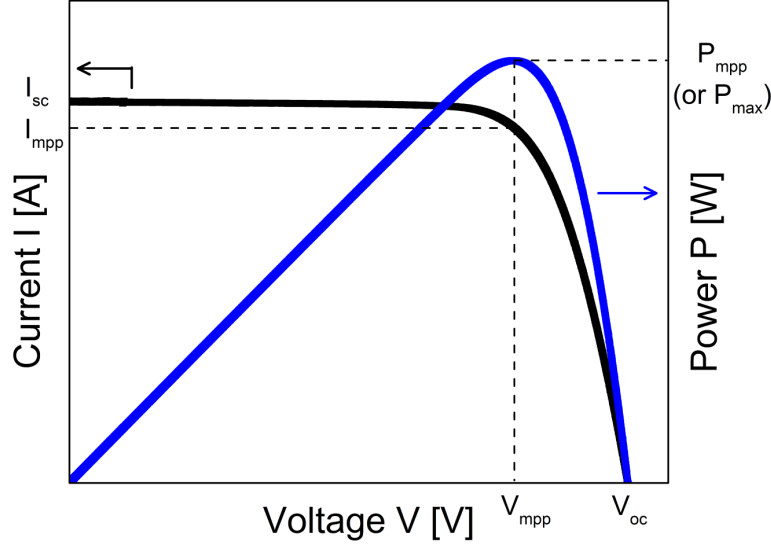


Figure 2.2: Classical I-V and P-V (power-voltage) curves of a PV module with some of the relevant electrical characteristics, such as  $I_{sc}$ ,  $V_{oc}$ ,  $P_{max}$ .

- The short-circuit current ( $I_{sc}$ ): the maximum current passing through the solar cells when the voltage difference is null;
- The current ( $I_{mpp}$ ) and voltage ( $V_{mpp}$ ) at the maximum power point;
- The maximum power point ( $P_{mpp}$  or  $P_{max}$ ): the maximum power that can be extracted from the PV module. It is calculated as:  $P_{max} = V_{mpp} \cdot I_{mpp}$ ;
- The fill factor ( $FF$ ): is a value expressed in % and it expresses how far is the recorder I-V curve from the ideal I-V squared shape. It is calculated as:  $FF = \left( \frac{I_{mpp} \cdot V_{mpp}}{I_{sc} \cdot V_{oc}} \right)$ ;
- The power conversion efficiency ( $\eta$ ): expresses the ratio of the measured electrical power out-put with respect to the incident light power input under STC. It is calculated as:  $\eta = \left( \frac{P_{max}}{P_{in}} \right)$ .

The I-V curves were measured indoors using a solar simulator device. The PV module was placed horizontally over a glass table with the solar cells facing downwards and connected in the four-point probe configuration (to remove the effect of probe/cell contact resistance). The device was then illuminated by a set of halogen and LED light sources which replicate the AM1.5G spectrum. The temperature of the device was recorded by a temperature sensor placed at the back of the module. The software automatically corrected the I-V curve to STC (25°C) for temperature deviations using the measured temperature and the temperature coefficients for  $V_{oc}$ ,  $I_{sc}$  and  $P_{max}$ . The measurement uncertainty of the setup is estimated at  $\pm 3\%$ , and the reproducibility at  $\pm 1\%$ . An example of an I-V curve is shown in Figure 2.2.

This type of measurement was the most used during the work. The change of the curve behavior and electrical parameters during different aging tests were helpful in understanding

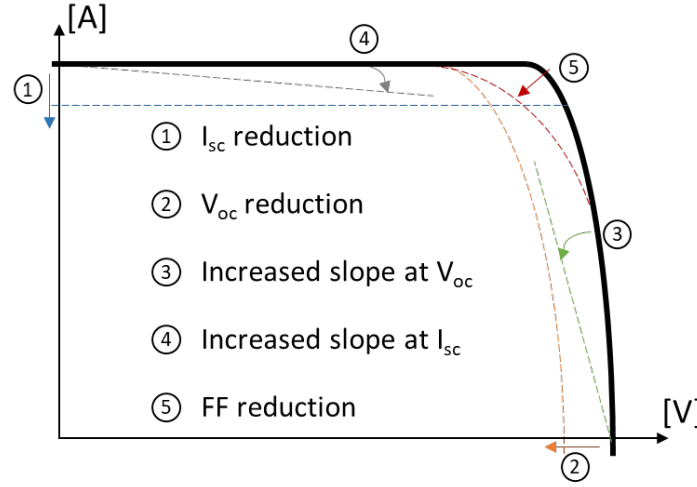


Figure 2.3: Effect of some module degradation on the the relevant electrical characteristics of a classical I-V curve of a PV module, such as  $I_{sc}$  and  $V_{oc}$  reduction (1 and 2), the increase of the slope near the  $V_{oc}$  (3) and near the  $I_{sc}$  (4), and FF reduction (5).

what part of the module was mainly affected by the specific experimental condition. Figure 2.3 shows how to interpret the most common I-V curve deviations: a reduction of the  $I_{sc}$  can be related to discoloration of the encapsulant or degradation of the anti-reflecting coating; a  $V_{oc}$  reduction can be due to a loss of passivation of the cell; an increased slope near the  $V_{oc}$  is the consequence of metallization corrosion, whereas an increased slope near the  $I_{sc}$  can be due to the formation of shunt paths in the PV cells [88]. Most of the time, we were not interested in absolute values but rather in relative variation with respect to the un-aged condition. Hence, the electrical parameters were normalized with respect to the value at the beginning of the test, set at 100%.

### 2.2.2 Electroluminescence (EL)

Electroluminescence (EL) imaging of PV modules is a fast, non-destructive analysis that provides a qualitative module inspection. From the recorded image, it is possible to identify some defects, such as shunts, cell cracks, broken fingers, and interconnections. The methodology consists in injecting a DC current (typically the value of  $I_{sc}$ ) in the module to stimulate radiative recombination of generated electrons, and holes in the solar cells [86]. Emitted photons are detected by a charge-coupled device (CCD) camera specifically, we used a SamBa Ci model from Sensovation, equipped with a Nikon lens with a fixed focal length and a pixel resolution of  $1660 \times 1252$ . Images are acquired in dark conditions to reduce background noise. In this work, we used EL to compare the current flow inside the module before and periodically during an aging test. An example of EL comparison before and after hail test is shown in figure 2.4 with clearly visible spots where the hail balls have hit the module with consequent damage on a cell level.

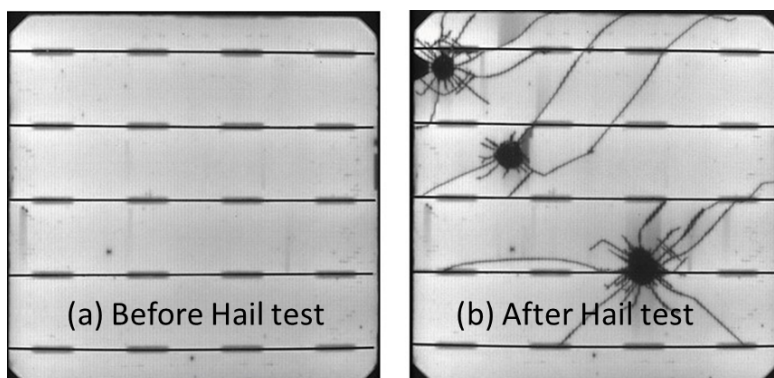


Figure 2.4: Example of EL images: (a) taken before the test, and (b) after hail test. It is clear that where the hail balls have hit the module the cell got damaged and the current cannot flow.

### 2.2.3 Photoluminescence (PL)

Photoluminescence (PL) is a further tool used to qualitatively assess the passivation of the solar cell. As for the EL technique, a CCD camera is used to detect photons coming from the radiative recombination mechanism. However, the carrier generation source comes from a laser hitting the cell surface. Cell regions with high signal - i.e. strong radiative recombination - denote good passivation. Contrary, sample regions appearing dark correspond to a badly passivated, or damaged parts. As the EL imaging, this technique is fast, contactless, and non-destructive. PL imaging was mainly used in Chapter 4 to compare the effect of different packaging layers on the cell during aging tests.

## 2.3 Tools for characterization of module materials

### 2.3.1 Fourier Transformed Infrared (FTIR) spectroscopy

The Fourier transform infrared (FTIR) spectroscopy is another analytic technique mainly used to identify the chemical composition and changes in the material. Depending on the type of sample, two different measurement methods were performed. To avoid unwanted absorption from the glass plate, the EVA samples were measured in attenuated total reflectance (ATR) mode on a Bruker Tensor 27 FTIR-Spectrometer with a Smart Orbit diamond - put in direct contact with the polymeric surface to analyze - ATR unit over a continuous scanning from  $600\text{--}4000\text{ cm}^{-1}$  (the background is collected on a clean ATR crystal). An example of an FTIR-ATR measurement of the EVA is reported in Figure 2.5a. Typical peaks for EVA at  $1370$ ,  $1463$ ,  $2850$ , and  $2920\text{ cm}^{-1}$  can be assigned to the symmetric, asymmetric and deformation vibrations of the  $\text{CH}_2$  and  $\text{CH}_3$  groups of the ethylene segments [89]. The absorption at  $1736$ ,  $1238$  and  $1020\text{ cm}^{-1}$  correspond to ester groups of the Vinyl Acetate segments [89]. In Chapter 4, non encapsulated solar cells were measured in transmission mode on a Bruker Tensor 27 FTIR-Spectrometer during a continuous scanning from  $650\text{--}4000\text{ cm}^{-1}$  with Opus software.

In both cases, each layer was analyzed by 32 scans recorded with a resolution of  $4\text{ cm}^{-1}$ .

### 2.3.2 UV visible Near infrared (UV-Vis-NIR) spectroscopy

UV-Visible spectroscopy is an important analytical tool, mainly used here to measure the transmittance of the polymeric encapsulant. A Lambda 950 spectrometer from Perkin Elmer (Waltham, USA) was used for the UV-Vis analysis. Spectra were recorded from 250 to 1000 nm with an integrating sphere from Labsphere (North Sutton, USA) to measure the hemispherical transmittance. From the transmittance properties is possible to calculate the Yellowing Index (YI) of the polymer following the procedure from [90]. Specifically, in Chapter 5, we used the YI to correlate the Isc reduction of the polymer with the browning of the EVA. This analytical technique was used on squared samples of  $10 \times 10\text{ cm}^2$  as previously described in Section 2.1.

### 2.3.3 Raman Spectroscopy

Raman spectroscopy is a further nondestructive technique used in this work to identify corrosion products. A laser beam is focused on the sample to be examined. The energy/frequency of the scattered photons is measured. Some photons can change energy upon inelastic interactions with vibration modes in the sample. The loss (or gain) in energy, and thus the frequency shift, is characteristic of the chemical bonds present in the material.

Raman spectroscopy was used in Chapter 6, to identify corrosion products. We used a Mono-Vista CRS+ with an Olympus BX51WI camera. Three acquisitions of 60 seconds of exposure with a 514 nm green laser to obtain more precise spectra.

### 2.3.4 Differential scanning calorimetry (DSC)

Differential scanning calorimetry (DSC) is a common thermo-analytical technique used to analyze polymers. It measures heat flow into or from a sample under heating, cooling, or isothermal conditions as a function of sample temperature. The main thermal transitions occurring in polymers can be detected, such as the glass transition temperature  $T_g$  (the temperature at which a polymer changes from a viscous or rubber condition to a hard or relatively brittle one due to changes in chain mobility), the melting temperature  $T_m$  - or range - (corresponding to a change from a solid to a liquid state of the polymer, due to an increased chains mobility), the crystallization temperature - or range -, as well as other exothermic or endothermic reactions [91, 92].

Figure 2.6 shows a characteristic heating DCS thermogram of an EVA from  $-70^\circ\text{C}$  to  $200^\circ\text{C}$ . As highlighted in the graph, the main EVA phase transitions are: (i) the glass transition between  $-40^\circ\text{C}$  and  $-20^\circ\text{C}$  [93], (ii) the melting region between  $55^\circ\text{C}$  and  $65^\circ\text{C}$  [94], and (iii) the exothermal decomposition, at  $120\text{-}200^\circ\text{C}$  range, of the additives, such as peroxides corresponding to the cross-linking chemical reaction needed to avoid creep phenomena [95]. In this work, we used

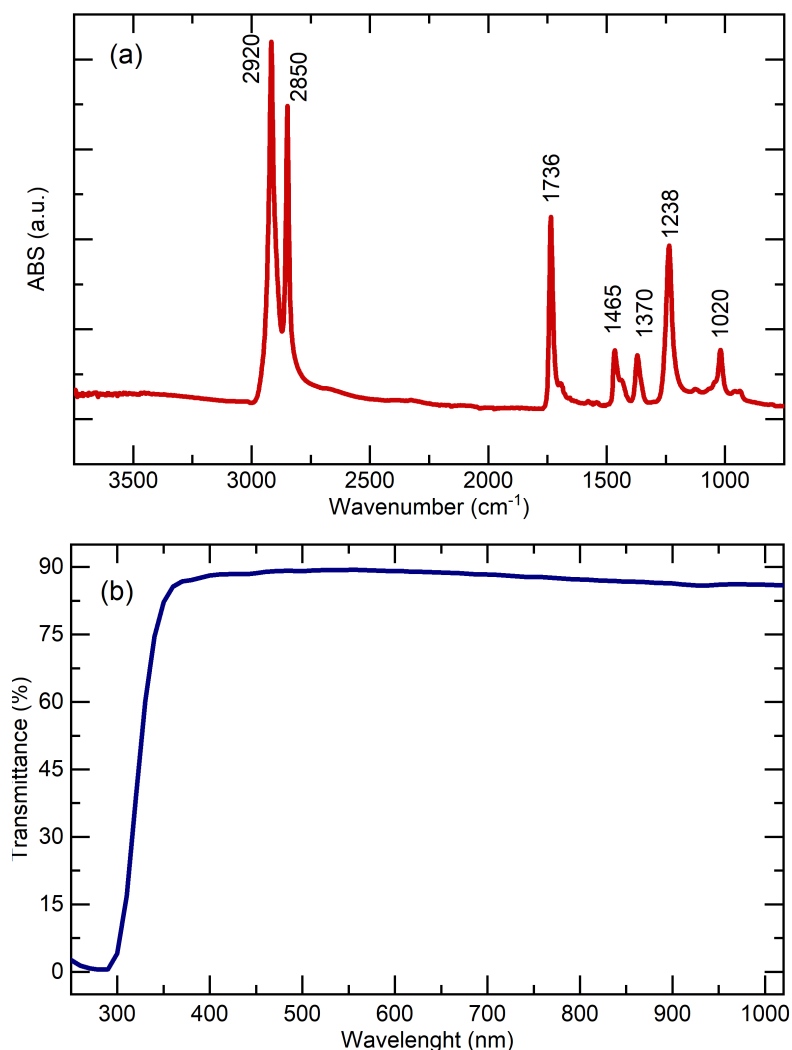


Figure 2.5: Chemical and optical properties of the EVA used in this work after the lamination process. (a) FTIR-ATR scan with the corresponding absorption peaks; (b) Transmittance of the glass/EVA/glass coupon in the UV-visible spectrum.

the DSC in Chapter 5 to study the effect of the UV degradation on the EVA encapsulant and observe potential changes in the polymer morphology related to the presence of water. DSC analyses were performed using a DSC TA Q100, from TA Instruments. For each sample, three different thermographs were recorded - 1<sup>st</sup> heating run, a cooling run, and 2<sup>nd</sup> heating run - under nitrogen atmosphere (80 ml/min). The heating and cooling rate was 10 K/min. Peak temperatures were evaluated according to ISO 11357-3 [96]. The first heating scan gives information regarding the history of the polymer: both physical and chemical characteristics (i.e. lamination or aging effects). After cooling, the second heating is designed to erase the thermal history of the sample and shows only irreversible processes (i.e. chemical degradation).

Some of the measurements were performed at the Laboratory for Processing of Advanced

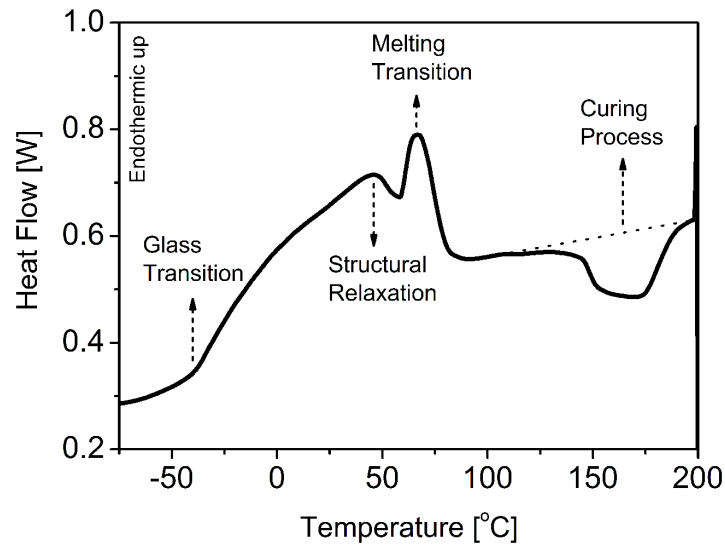


Figure 2.6: Typical DSC thermogram of EVA. The glass transition appears at approximately -30 °C. Two overlapped endothermic peaks are centered at about 45°C and 60 °C. The broad exothermic peak from 110°C to 190 °C corresponds to the thermal decomposition of the additives (mainly peroxide) and subsequent curing of the EVA. Image taken from [97].

Composites (LPAC) at EPFL. We gratefully acknowledge the laboratory for the permission.

### 2.3.5 Scanning Electron Microscopy (SEM)

Scanning Electron Microscopy (SEM) images were mainly taken on a Zeiss Gemini 2 microscope, equipped with an Energy-Dispersive X-ray (EDX) detector, typically operated with a 5 keV incident e-beam. This technique was used in Chapters 4 and 7 to check the stability of the metallic lines - fingers and ribbons - and solder joints of aged solar cells. A 2 x 2 cm<sup>2</sup> sample was cut from the encapsulated modules by means of a diamond wire saw. To obtain a mirror-like surface, samples were embedded in a resin and subsequently mechanically polished.

SEM images were taken by Quentin Jeangros. His contribution is gratefully acknowledged.

## 2.4 Indoor aging tests

### 2.4.1 Damp Heat (DH)

The damp Heat (DH) aging test is one of the most used indoor tests in the PV reliability field. It is part of the test sequence of the IEC 61215 standard [40]. The test conditions are: constant air temperature and relative humidity of 85°C, and 85%, respectively. The standard test duration is 1000 hours. During this work, we extended the test duration up to 2000 and 3000 hours. A

climatic chamber from WEISS was used.

### 2.4.2 UV aging

The UV aging test was performed following the IEC 62788-7-2-A3 standard [98]. A Q-Sun Xenon chamber (Q-Lab) is used with the following exposure conditions:

- Chamber air temperature: 65°C;
- Black panel temperature: 90°C;
- Irradiance: 0.8 W/m<sup>2</sup> at 340 nm;
- Relative humidity: 20%.

The Xe-arc lamp with daylight filter has a UV dose corresponding to 63 W/m<sup>2</sup>. Figure 2.7 shows the UV-Vis spectrum of the lamp and the transmittance values of the glass and EVA used in this work.

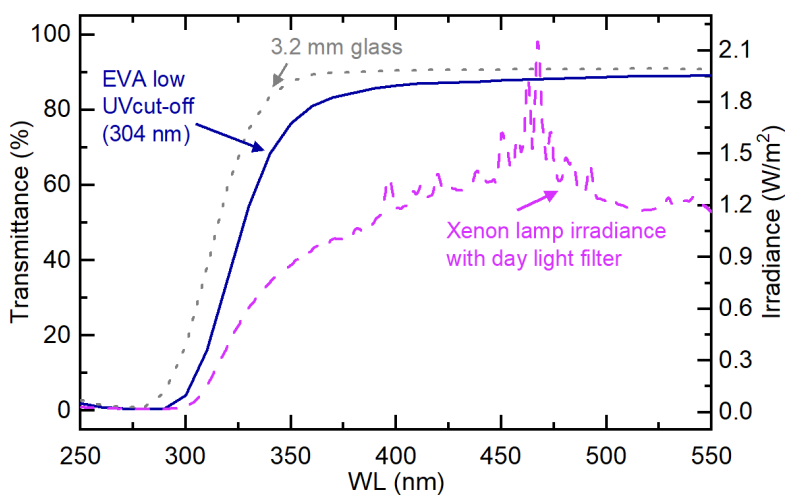


Figure 2.7: Irradiance spectrum of the Xe-arc lamp coupled with a daylight filter in the UV-Vis spectrum along with the transmittance values of the glass plate and the EVA.

## 3 Moisture ingress in G-G modules encapsulated with EVA

### Summary

In this chapter, we investigate the reliability of double-glass PV modules encapsulated with ethylene vinyl-acetate (EVA), under single outdoor stressors. In particular, we investigated the effect of the relative humidity (RH) by performing damp Heat (DH) stress tests extended up to 2000 hours (i.e. 1000 hours more than the duration foreseen in the standard). Different single-cell modules were fabricated with the same laminate structure (and bill of materials) using different cell types, i.e. standard back surface field (Al-BSF), passivated emitter rear cell (PERC) and silicon heterojunction (SHJ). The results show that the EVA's relatively high water vapor transmission rate (WVTR) allows water to diffuse inside the glass-glass module from the edges. EVA's physical and chemical properties remain stable for all samples during the whole test duration. However, the effect of DH affects the electrical parameters of modules differently, depending on the specific cell technology and metallization. We observe a slight current reduction for PERC and a series resistance increase in the Al-BSF, leading to efficiency losses of 1 to 5% after 2000 hours of damp heat. For SHJ, a substantial power reduction of ~65% is observed with EVA encapsulant, which correlates with moisture ingress into the encapsulant.

### 3.1 Introduction

Historically, the vast majority of field-deployed PV modules have a glass-backsheet (G-BS) structure. Until recently, the use of modules with a glass-glass (G-G) structure has mostly been limited to special applications, such as building-integrated PV (BIPV), for which stricter mechanical and structural requirements must be met. Nevertheless, the market share of G-G modules is considerably gaining momentum due to the possibility of manufacturing bifacial modules, especially for large utility-scale systems, as they offer potential energy yield gains of 10-20% when compared to conventional mono facial devices. The market share of G-G PV modules is expected to reach 40% in 2030 [30].



The rise of the passivated emitter and rear cells (PERC) and silicon heterojunction (SHJ) cells offer the possibility to fabricate bifacial devices, which due to the rear-side metallization, was not possible for conventional back surface field (BSF) cells. To allow absorption of the sun light from the rear side, the module design needs to be modified by, for instance, the replacement of conventional rear white BS with a transparent one [80], or with a second glass cover. The added glass plate improves physical insulation against moisture and pollutants, as well as mechanical stability of the module [83].

An important component for the reliability of PV modules is the polymeric encapsulant. Newly developed polyolefines (POs) are recommended in a G-G structure rather than the standard ethylene vinyl acetate (EVA). In fact, POs have a lower water vapor transmission rate compared to the EVA. Additionally, they do not contain vinyl acetate units, hence no acetic acid (HAc) is generated upon photodegradation [31]. In the more common glass-BS structure, the permeable BS allows an easier out-diffusion of generated volatile HAc, which would otherwise remain trapped inside the module - as for the case of a G-G layout - eventually causing the corrosion of metallic interconnects. However, some manufacturers still rely on the use of EVA to produce glass-glass modules thanks to its lower price and easier processability [99]. Recently, some industrial manufacturers are also examining the possibility of using different encapsulant formulations for the front (i.e. EVA), and for the rear (i.e. PO) [100, 101].

Given that the track record and experience for field-deployed glass-glass PV is still limited, indoor aging tests are critical in investigating different module designs and comparing differences between BOMs.

## 3.2 Experimental methods

### 3.2.1 Sample fabrication

Single-cell mono-crystalline silicon glass-glass modules with Al-BSF, PERC, and SHJ solar cells were prepared as illustrated in Figure 3.1a. The laminate structure included glass front, back covers, and an EVA encapsulant. The solar cell top metallization was based on screen-printed silver with five (Al-BSF and PERC) or four (SHJ) busbars, and cell interconnects were 1.5 mm wide flat copper wires coated with a lead-tin based solder. Al-BSF and PERC cells were soldered onto the busbars, and SHJ cells were glued using a silver-based electrically conductive adhesive (ECA).

In parallel, we investigated the potential degradation of the EVA encapsulant during aging tests by laminating 10 x 10 cm<sup>2</sup> coupons in a glass/EVA/EVA/glass structures (see Figure 3.1b).

### 3.2.2 Aging test

After the lamination process, all samples were subjected to conventional damp heat aging test following the IEC 61215 standard [40]. The climatic chamber was set at 85°C with relative

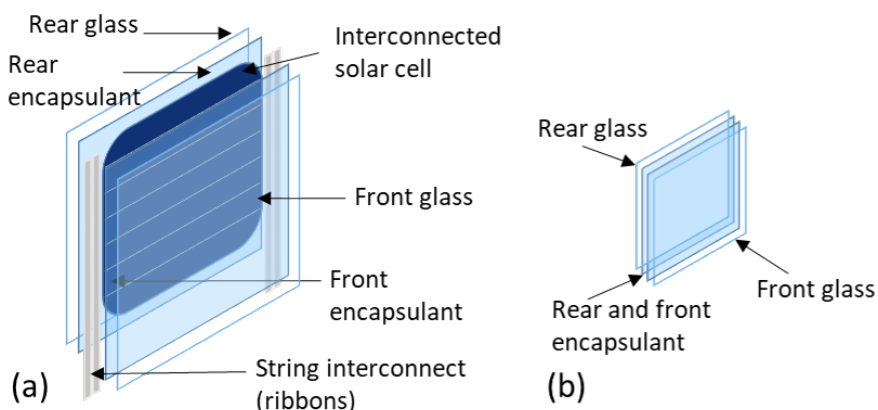


Figure 3.1: Schematic representation of the single-cell modules (a) and 10 x 10 cm<sup>2</sup> coupons (b) used to analyse the EVA properties during DH aging test.

humidity (RH) of 85%. The standard test duration of 1000 hours was extended up to 2000 hours. Indeed, the more insulated G-G structure should allow one to avoid or at least delay water ingress. However, the diffusion process can start from the module edges, where the EVA is directly exposed to the environment.

### 3.2.3 Module and material characterization

Periodically during the aging test, the modules were removed from the climatic chamber and characterized. Modules were visually inspected and characterized using I-V curves performed at standard test conditions (STC, 25°C and light intensity of 1000 W/m<sup>2</sup>). The main optoelectronic properties that were monitored included the power at maximum power point ( $P_{max}$ ), short-circuit current ( $I_{sc}$ ), open-circuit voltage ( $V_{oc}$ ), and fill factor (FF). EL imaging was performed by forward biasing the modules with a current corresponding to  $I_{mpp}$ .

Chemical properties of the EVA encapsulant were also periodically characterized by performing FTIR spectroscopy (in ATR mode) on polymer samples extracted from the 10 x 10 cm<sup>2</sup> glass/EVA/glass coupons.

## 3.3 Results

### 3.3.1 Effect of the Relative Humidity

#### Module and cell degradation

Figure 3.2 shows the I-V curves (a) and EL images (b) of the **Al-BFS** G-G modules performed at regular intervals during the execution of the DH aging test. After 1000 hours, we observed a gradual blackening of the EL intensity, appearing first on the most outer part of the cell. After

200 hours, the image showed a blackening concentrated around the busbar (BB) area. The **decrease of the fill factor** matches well with the observed darkening along the BBs [102]. This particular degradation pattern is also reported by Kumar *et al.* [103] as *the interruption of finger connections along the busbars*, particularly detected in Al-BFS cells encapsulated in a G-G structure. Specifically, they explain that this phenomenon was primarily caused by cell cracking due to residual mechanical stresses after the soldering and the lamination process. Nevertheless, all other electrical parameters (i.e.  $I_{sc}$  and  $V_{oc}$ ) remained stable during the whole duration. The power reduction after 1000 hours (i.e. standard test duration) was less than 1%, above the DH pass/fail criterium set at -5%. However, after +1000 hours of extension (i.e. a cumulative 2000 hours of DH test), the power reduction was 5.6%. The gradual darkening of the EL images, starting from the edges of the module and gradually reaching the center of the sample, can be attributed to **moisture ingress**. Despite the added second rear glass plate, the non-optimal Water Vapor Transmission Rate (WVTR) of the EVA [104] allowed water to diffuse from the edges.

Figure 3.2c and d report the results related to the **PERC** modules. In this case, the power remained stable for the whole test duration. After 2000 hours of DH, no sign of degradation was observed from the I-V curves, in accordance with results recently published by Sulas *et al.* [105] nor from EL images; however it is interesting to make a comparison with the Al-BSF cells. The front side of Al-BSF and PERC architectures are similar. As described previously, in Chapter 1 (Section 1.3.1), the main difference between the two cell structures is at the rear side of the cell. However, the specific set of cells investigated in this work was manufactured by two distinct companies. It is likely that they have used different screen printing formulations to deposit busbars or the soldering temperatures were not the same. These differences, combined with specific viscoelastic properties of the EVA can cause solder joint degradation due to thermomechanical fatigue [106]. By comparing the EL images in Figure 3.2b and d, we notice how the use of a particular silver paste formulation or soldering conditions can affect the module stability.

Completely different behavior is reported in Figure 3.2e and f, showing the results of **SHJ** G-G modules. Already after 500 hours of DH we could observe a change of the I-V curve with a remarkable reduction, particularly of the  $I_{sc}$  and the  $V_{oc}$ . SHJ did not pass the standard DH test duration, and we recorded a **power loss of about 50%** compared to the initial nominal power after 1000 hours. A gradual EL darkening is clearly visible in Figure 3.2b. However, contrarily to what occurred on the Al-BSF cells, the **dark region of SHJ spread on the whole surface** and the BBs remained the only bright spots. This result can be related to an incompatibility of the cell type in the presence of moisture, or a non-optimal formulation of the finger grid.

Figure 3.3 resumes and compares the variation of main electrical parameters (i.e.  $P_{max}$ ,  $I_{sc}$ ,  $V_{oc}$  and FF) of the tested modules. Al-BSF and PERC modules were fairly stable, whereas encapsulated SHJ cells suffered a strong degradation already after the first 500 hours of exposure to a highly humid environment.

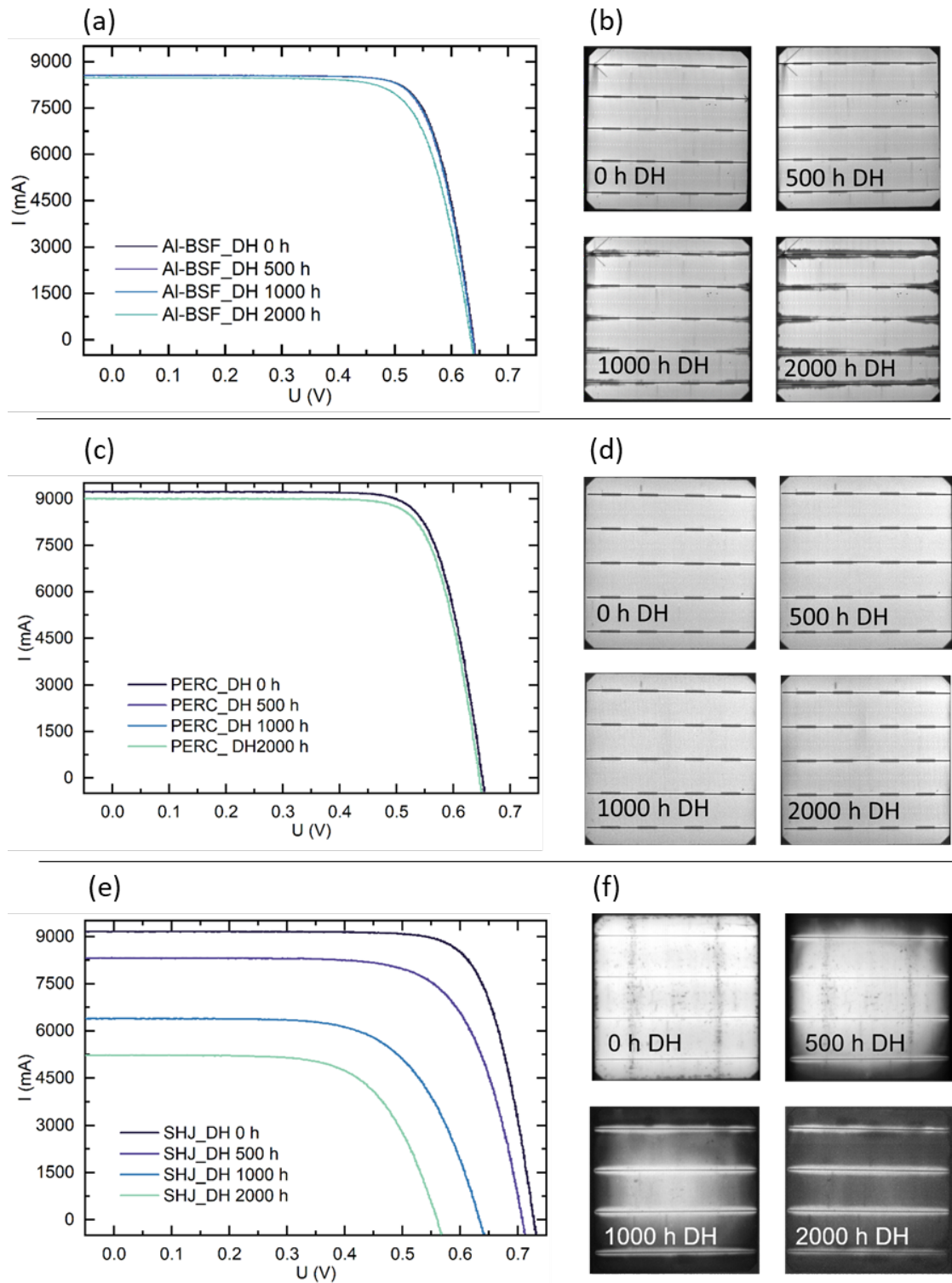


Figure 3.2: I-V measurements and EL images of G-G EVA single-cell modules using Al-BSF (a-b), PERC (c-d), and SHJ (e-f) during extended damp Heat aging test up to 2000 hours.

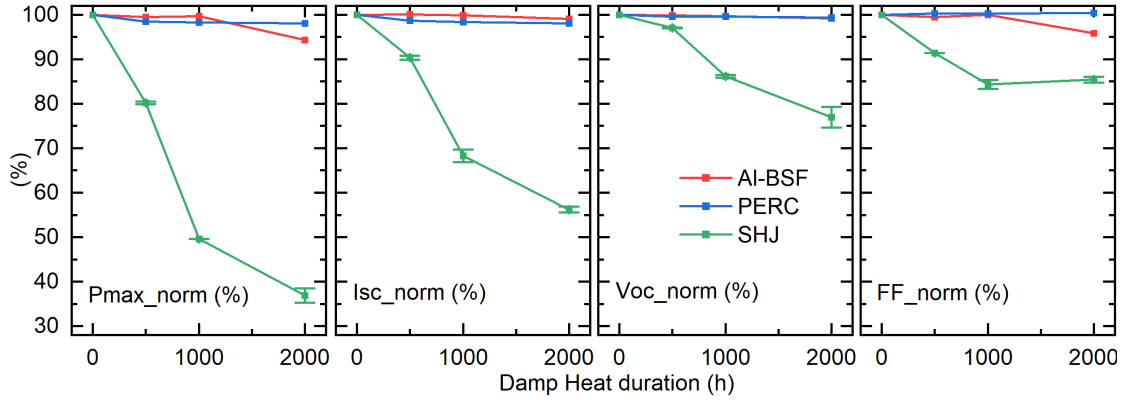


Figure 3.3: Normalized I-V electrical parameters of G-G EVA single cell modules during extended damp Heat aging test up to 2000 hours. Red curves refer to Al-BSF cells, the blue are PERC cells, and the green curves are G-G modules with SHJ solar cells.

#### 3.3.2 Water ingress modeling

The presence of the rear glass cover prevents moisture from diffusing at the rear side, ensuring good mechanical stability of the module. Thus, the aluminum frame's adoption in glass-glass modules can be avoided. In this configuration, the edges of the module are open, and the encapsulant is exposed to the environment.

The diffusivity properties of the EVA were experimentally measured by performing WVTR analysis at the Laboratory for Processing of Advanced Composites (LPAC) at EPFL. Then, by using Finite Element Method (FEM) models previously developed by former colleagues from PV-Lab (we particularly acknowledge Eleonora Annigoni), we set up mathematical simulations by analytically solving the diffusion equation. The water concentration inside the single-cell G-G module during the DH test was evaluated. More details regarding experimental measurements of EVA diffusion properties and mathematical simulations can be found in the Appendix A and B. It is worth mentioning that we assumed Fickian diffusivity, which means that the diffusion properties of the EVA does not depend on the water concentration. However, a deviation from the Fickian regime is possible for certain encapsulant materials as recently reported by Mitterhofer *et. al* [107]. In fact, water can have a plasticizing effect at high relative humidity (RH) concentrations, which for example could increase the solubility parameter compared to the Fickian model. However, there is no clear answer in the literature explaining how the diffusivity properties of EVA change with the RH.

Results of the simulations are reported in Figure 3.4 showing the water concentration profiles of two different points of the module, i.e. at the external edge of the cell and at the center of the module. By comparing the results of the simulations with the electroluminescence images of the SHJ modules, we can observe a good correlation between the moisture ingress and the blackening of the cell. Particularly, the corner edge darkened after 500 hours of test, which corresponds to a water concentration close to the saturation value (red star points

in Figure 3.4). Moreover, the center of the cell reduced its intensity after 1000 hours of DH exposure (green star points in Figure 3.4). The corresponding water concentrations for the 2 points (i.e, the cell edge after 500 hours and the center of the module after 1000 hours) were relatively similar and approached the saturation concentration.

This result confirms that the cell degradation was due to moisture inside the sample and that a certain amount of water, close to the saturation concentration was needed to damage the cell. The same water diffusion mechanism was expected for all tested modules (i.e. SHJ, BFS and PERC cells). We should point out that such mini-modules were expected to be more sensitive than full G-G modules where humidity takes more time to reach the center, as shown by Mittag *et al.* [108].

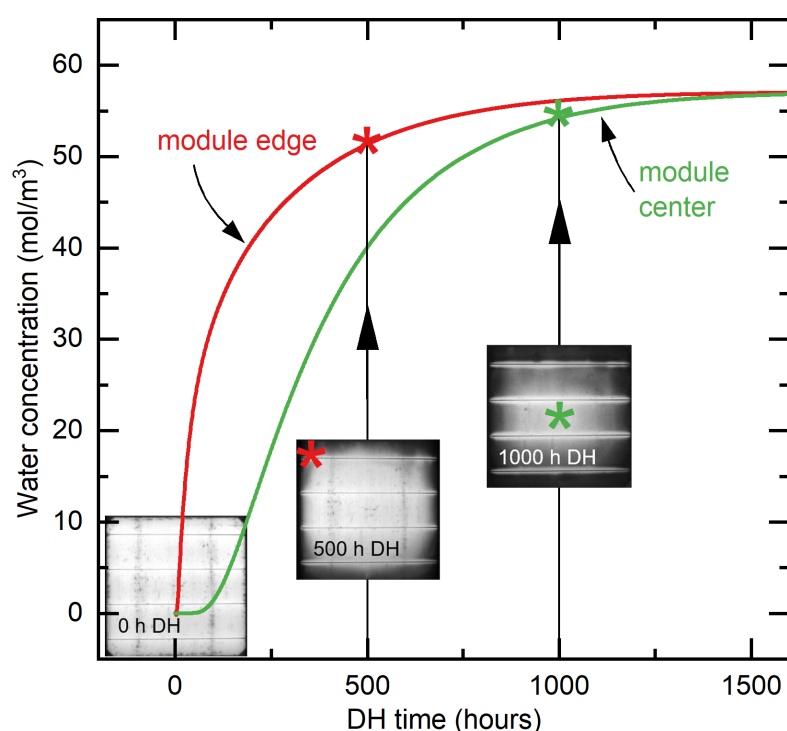


Figure 3.4: Water concentration profile during damp Heat of single-cell module computed at the edge of the module (red curve) and at the center (green curve) with inset of corresponding EL images to validate the water ingress hypothesis.

### EVA stability

The degradation mechanism of the EVA occurring in the presence of moisture and elevated temperature is well documented in the literature. Particularly, the hydrolysis reaction produces acetic acid [109], lowering the pH and potentially leading to corrosion of the metallic interconnections [110].

To follow the EVA potential degradation during the aging test, we analyzed the smaller 10 x

10 cm<sup>2</sup> coupons (due to space constraints in the climatic chamber). It is worth mentioning that the size difference between the EVA coupons and the 20 x 20 cm<sup>2</sup> single-cell modules introduces some limitations to the comparison. As a matter of fact, in the case of moisture diffusion from the edges of the module, water will reach the center of the single-cell module (i.e at 10 cm from the edge) in a longer time scale compared to the glass/EVA/glass samples, where water has to travel half of the distance (i.e. at 5 cm from the edge). However, the analysis of the encapsulant helped understand how its properties varied during the aging test.

The characterization of chemical groups via FTIR spectroscopy for the EVA is shown in Figure 3.5a. After the lamination process, characteristic bands for the unaged samples were observed. Typical peaks for EVA at 1370, 1463, 2850, and 2920 cm<sup>-1</sup> can be assigned to the symmetric, asymmetric and deformation vibrations of the CH<sub>2</sub> and CH<sub>3</sub> groups of the ethylene segments [89]. The absorption at 1736, 1238 and 1020 cm<sup>-1</sup> correspond to ester groups of the Vinyl Acetate segments [89]. During DH aging tests, no chemical changes were detectable. The selected EVA formulation showed good moisture chemical stability.

Optical transmittance was also measured during the test, as shown in Figure 3.5b. During the exposure in DH, the spectrum did not show relevant changes. It was possible to observe a slight reduction of the transmittance value in the visible range from 89.38% to 88.20% after the first 1000 hours of test. A decrease in the UV-blue range (from 340 to 390 nm) was also visible after 2000 hours of exposure. Overall, the transmittance of the polymer was stable. This result is well in accordance with the stable  $I_{sc}$  values recorded on Al-BSF and PERC modules.

The obtained results on the stability of both chemical and optical properties of the EVA under extended DH test are well in accordance with results recently published by Barretta *et al.* [85]. This is a good indication that recently developed EVA formulations are more resistant in the presence of moisture.

## 3.4 Discussion

The goal of this first aging test was to study, on a module level, the effectiveness of using EVA in a double glass laminate with different cell architectures and examine potential failures related to moisture ingress inside the module.

It is important to remark that the damp heat test does not allow one to have any insight into the modules' long-term performance and wear-out mechanisms or the different materials. In fact, damp heat imposes stresses far above the field use environment, as reported by Kempe in [111]. The water vapor saturation concentrations in EVA during DH are much higher compared to values reached during outdoor exposure [112]. Nevertheless, it routinely executes qualification tests to assess potential shortcomings in the design of PV modules.

Particularly, we observed that:

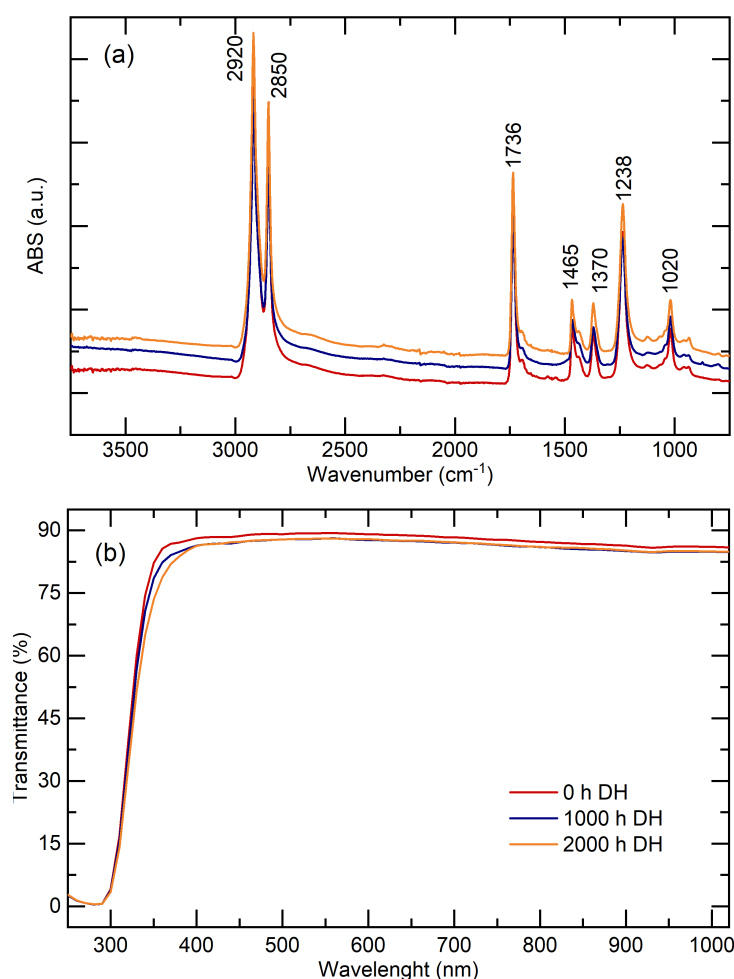


Figure 3.5: Chemical and optical characterization of EVA during extended DH aging test: (a) FTIR-ATR scans, and (b) UV-Visible transmittance.

1. BSF modules were fairly stable in DH with some increased resistive losses, possibly due to corrosion of metallic interconnects (BB or ribbons) after 2000 hours. Consistent with a slight decrease of FF.
2. PERC cells were fairly stable over the whole duration - we observed a slight decrease in the current.
3. SHJ: we observed a strong degradation for the encapsulated cells, which became clear after the first 500 hrs. Both  $I_{sc}$  and  $V_{oc}$  were strongly impacted.
4. EL images for SHJ showed progressive evolution of darkening from the edges, which we attributed to moisture ingress in the encapsulant due to the relatively high WVTR of EVA and its high water permeation properties [113].
5. The water ingress (and its temporal progression) was confirmed by our water diffusion model with parameters specific to EVA. As all modules shared the same BOM (EVA and



glass, except for the cell), we expected a similar absorption of water in all modules, irrespective of the cells used.

6. In addition, the EVA encapsulant was quite stable during the exposure to DH test conditions. In fact, no noticeable signs of chemical nor optical degradation were noticed within the first 2000 hours of exposure.

Therefore, a clear and specific sensitivity to moisture of SHJ cells was observed, which is already known in the PV field. In fact, industrial SHJ modules use encapsulants with a lower WVTR (or lower water absorption content, such as POs). Nevertheless, an understanding of this extreme sensitivity of SHJ to water ingress is still missing.

## 3.5 Conclusions

Standard qualification tests, i.e. damp Heat, have proven to be valuable to investigate potential pitfalls/failure modes of PV modules. However, these results cannot be used as lifetime tests. We considered this test a screening test to understand what are the main limitations and how we can adapt/modify some parameters to replicate in a more efficient way the wear-out mechanisms of a double glass structure.

Particularly, **we want to investigate the possibility of continuing to use EVA encapsulant in G-G modules.**

The good optical and chemical stability of the EVA after 2000 hours of DH are an indication of the polymer formulation improvements during the last years.

Mathematical simulations confirmed that water can still diffuse from the edges of the module, where EVA is in direct contact with the environment. In the specific case of single-cell modules with a size of  $20 \times 20 \text{ cm}^2$  at  $85^\circ\text{C}$  and 85% RH, the EVA gets fully saturated after 1500 hours. However, the reduced size of the tested samples partially preclude the possibility to directly compare these results to a standard 60-cells PV module. In fact, the water diffusion process will take longer time on a surface of  $1.60 \text{ m}^2$ .

A particular case is the degradation of SHJ cells during damp Heat tests. The technology showed a strong sensitivity to moisture ingress. In fact, the module power output dropped approximately 50% with respect to the initial value during the first 1000 hours of test. The result is in accordance with the choice of some PV manufacturers. In general, SHJ G-G modules are encapsulated with polyolefin-based formulations. However, a detailed description of this degradation mechanism is still missing in the literature. The next chapter will focus on the understanding of this specific degradation mechanism.

## 4 Insights into the sensitivity of SHJ modules to damp heat: a microscopic model

### Summary

The encapsulation scheme of silicon heterojunction (SHJ) solar cells usually includes polyolefin (PO) based films. The use of conventional ethylene vinyl acetate (EVA) is discouraged due to the high-performance loss observed after aging tests, such as damp heat (DH). However, the degradation mechanism is not fully understood.

In this chapter, we attempt to explain the root causes of the degradation of SHJ glass-glass modules in damp heat and more generally, the peculiar sensitivity of the technology to water, proposing a detailed microscopic model.

Different sample designs (and materials) were used in order to understand, on a material level, the mechanism of the degradation mode.

Our results indicate that EVA is stable and exhibits no signs of degradation. Further, the low-temperature electrically conductive adhesive (ECA) and interconnects were stable when exposed to an extended test duration of 3000 hours. Initially, the power reduction was attributed to moisture ingress (due to the relatively high water vapor transmission rate (WVTR) of the EVA) that affected the stability of cell layers starting from the edges and spreading towards the center of the module. To our understanding, the role of EVA is instrumental in facilitating a faster water uptake in the module *sandwich*. However, the presence of water is not enough to explain the quick evolution of the degradation process. Additional observations led us to consider the role of glass – and its interaction with water – in the degradation process. In DH conditions, in fact, when solar-grade soda-lime glass is used, a leaching corrosion mechanism can occur at the surface of the glass with the release of sodium hydroxide (NaOH). The NaOH is dissolved in the water, forming an aqueous solution  $\text{NaOH}_{aq}$ , which, according to our hypothesis, percolates through the EVA, eventually reaching the solar cell. If a transparent and conductive oxide layer (such as indium tin oxide) with a sub-optimal morphological structure is present, we hypothesize a reaction with the *a-Si:H* passivating layers or at the *a-Si/c-Si* interface. Particularly,  $\text{Na}^+$  ions may act as recombination centers, reducing the passivation,

especially at the n-doped side of the cell (the front side in the case of a rear-emitter cell).

We propose strategies to reinforce the water-resistance of SHJ solar modules. These include the use of edge seals with EVA and the use of alternative polymers, such as PO.

### 4.1 Introduction

Double-side contacted silicon heterojunction (SHJ) solar cells have demonstrated efficiencies up to 25.1% [114, 115] and are on par with other advanced silicon-based technologies such as TOPcon [116]. SHJ usually stands out with a higher open circuit voltage ( $V_{oc}$ ) and fill factor (FF) but lower current due to the use of full-area hydrogenated amorphous silicon ( $a\text{-Si:H}$ ) for both surface passivation ( $a\text{-Si:H}(i)$ ) and selective layers ( $a\text{-Si:H}(n)$  and  $a\text{-Si:H}(p)$ ), paired with a transparent conductive oxide (TCO) - such as Indium Tin Oxide (ITO) - for lateral charge transport and anti-reflection. The symmetry of the SHJ architecture makes it possible to fabricate bifacial devices easily [117] enabling the absorption of the reflected light from the rear side.

A mass-market entrance has been delayed though by many negative perceptions concerning the difficulty of the technology. These include achievement of homogeneous ultra-thin passivation layers, the relatively high cost of high-quality n-type silicon wafers, the TCO, and the use of a silver paste for metallization [117]. However, a market share of 20% is expected by 2030 [30]. In fact, in the last few years, several companies have launched pilot production or even mass production of SHJ solar cells. Some companies recycled parts of the equipment designed for the production of thin-film silicon solar cells for depositing some of the SHJ layers [118, 119].

Another aspect related to SHJ PV modules is the use of polyolefin (PO) based encapsulant rather than the standard ethylene vinyl acetate (EVA). In the presence of humidity, SHJs perform better when a PO polymeric foil is used in both the glass-foil and glass-glass (G-G) configurations [120, 121]. As confirmed in the previous chapter, when EVA is used, water can enter from the edges of a glass-glass module. Here, we investigate the degradation mechanism and propose a microscopic model highlighting why the use of EVA in glass-glass modules using SHJ solar cells should be avoided. We also provide valuable mitigation strategies.

### 4.2 Experimental details

We manufactured single-cell glass-glass modules using standard 6" bifacial n-type rear emitter silicon heterojunction (SHJ) cells. A cross section of the SHJ cell is presented in Figure 4.1 showing the classical symmetry of the cell with the presence of intrinsic hydrogenated amorphous silicon ( $a\text{-Si:H}(i)$ ) layers on both the front and rear sides. The n-type ( $a\text{-Si:H}(n)$ ) layer at the front side and p-type ( $a\text{-Si:H}(p)$ ) layer at the rear side provide surface passivation and contact selectivity. The cell structure is finished with a sputtered TCO made of an ITO layer

and screen-printed metallization lines. The module design comprised front and rear plates with a 3.2-mm thick solar-grade soda-lime glass and the same commercial EVA used in the previous chapter. Modules were subjected to accelerated DH test, for up to 2000 hours, with the electrical performance of the module and physical characteristics of the materials monitored at regular intervals.

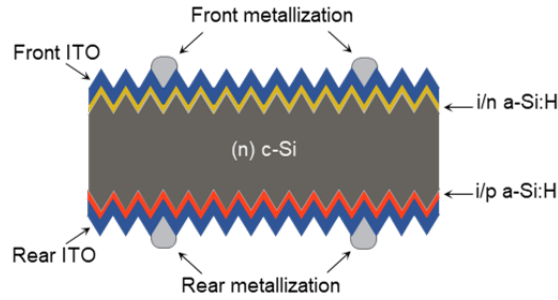


Figure 4.1: Schematic cross section of a SHJ cell. The n-type bulk wafer is coated with intrinsic hydrogenated amorphous silicon (a-Si:H(i)) layers on both sides, a p-type amorphous silicon (a-Si:H(p)) layer at the rear, and an n-type amorphous silicon (a-Si:H(n)) layer at the front. Indium tin oxide and metallic fingers allow for extraction of the electrical charges.

### 4.2.1 Samples design and fabrication

We manufactured single-cell modules with SHJ solar cells to monitor module performances. We tested three encapsulation schemes as shown in Figure 4.2:

1. Standard glass-glass layout;
2. *Glass-free* modules in which the front and rear glass plates were replaced by two ethylene tetrafluoroethylene (ETFE) foils. The surface of the ETFE foil exposed to the external environment had the classical hydrophobic property of fluoro-based polymers. The inner surface (i.e. the one in contact with the EVA) was chemically treated to promote good adhesion to the encapsulant. This configuration was used to compare degradation in the presence or absence of a potential sodium source (i.e. the soda-lime glass plate).
3. Standard glass-glass layout with the addition of a sealing agent (polyisobutene, PIB) along the edges of the module. The edge sealant was cut into strips of 20 cm and placed all around the module perimeter. Additionally, two small strips were put on top of the front ribbons extending outside the laminate in order to have a complete edge coverage.

Additional samples that we manufactured and tested include:

- 10 x 10 cm<sup>2</sup> glass/EVA/glass coupons to analyze the chemical stability of the encapsulant.

## Chapter 4. Insights into the sensitivity of SHJ modules to damp heat: a microscopic model

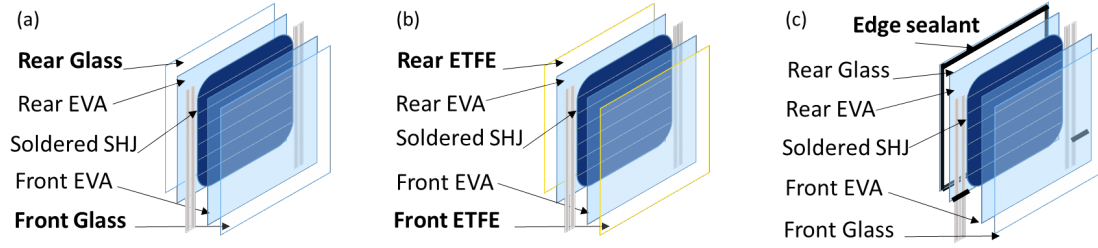


Figure 4.2: Schematic of the different single-cell SHJ modules tested in DH conditions: (a) standard glass-glass layout, (b) "glass-free" configuration in which the front and rear plates are replaced by a transparent hydrophobic ETFE foil, and (c) glass-glass layout with the addition an edge sealant.

- Cells encapsulated with EVA only (*EVA-only*), without the presence of the front and rear glass (EVA/cell/EVA) to understand the role of the EVA.
- Bare cells to investigate the effect of moisture directly on the solar cell.
- Polished (i.e. non-textured) wafers with different coatings (*a-Si* and *a-Si/ITO*) as seen in Figure 4.3 to compare the effect of water exposure on the *n-doped* and *p-doped* sides of the cell, and the presumed protective role of the external ITO layer.

### 4.2.2 Module characterization

During the aging test, samples were removed periodically from the climatic chamber to characterize both the front and rear sides. Single-cell modules were visually inspected, and then light current-voltage (I-V) characteristics were measured at STC (25°C and light intensity of 1000 W/m<sup>2</sup>). The main optoelectronic properties monitored included the power at maximum power point ( $P_{max}$ ), short-circuit current ( $I_{sc}$ ), open-circuit voltage ( $V_{oc}$ ), and fill factor (FF). Electroluminescence (EL) imaging was performed by forward biasing the cells with a current close to 8.5 A (i.e. the cell's  $I_{mpp}$ ). Additionally, we performed External Quantum Efficiency (EQE) measurements.

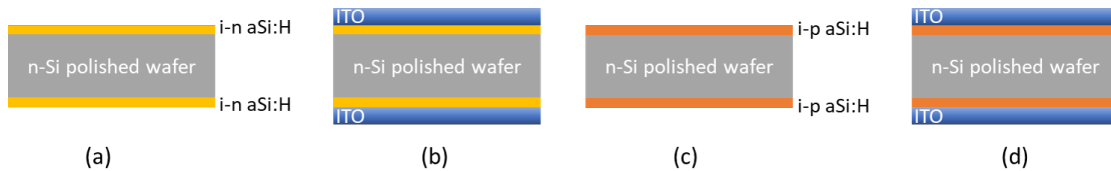


Figure 4.3: Schematic representation of the different un-textured n-type wafer sample stacks (all structures are symmetric, as the coatings are deposited on both sides): (a) *i/n a-Si:H* layer, (b) *i/n a-Si:H* layers with ITO, (c) *i/p a-Si:H* layer, (d) *i/p a-Si:H* layers with ITO.

Table 4.1: Normalized reduction of the I.V parameters of SHJ glass-glass modules after 2000 hours of DH exposure. The modules were flashed from both sides. Values were normalized to the initial pre-DH values.

I-V parameter	Front side	Rear side
$I_{sc}$	-49.60%	-9.93%
$V_{oc}$	-24.76%	-21.96%
FF	-14.33%	-18.27%
$P_{max}$	-63.10%	-41.62%

### 4.2.3 Cells and materials characterization

The stability of metallization lines (i.e. the fingers, busbars, and ribbons) and the electrically conductive adhesive (ECA) was analyzed by SEM. Double-side-polished Si wafers were characterized by Fourier transform infrared (FTIR) spectroscopy in order to collect information about the formation of new chemical bond groups on the different cell layers due to the presence of moisture. The same tool, in attenuated total reflectance (ATR) mode, was used to characterize the chemical stability of the EVA. Additionally, photoluminescence (PL) images were taken to effectively and swiftly compare the evolution of the cell degradation for the different module structures.

## 4.3 Results

### 4.3.1 Module electrical characterization

The I-V curves measured on standard glass-glass modules exposed to DH are represented in Figure 4.4a. Since the cells were bifacial, we characterized both sides of the cell. The graph shows results before and after 2000 hours of exposure and curves from the illuminated front and rear sides. A **significant reduction of the  $I_{sc}$ ,  $V_{oc}$  and fill factor (FF)** was observed. The effect was **more pronounced at the front side** of the cell compared to the rear side. Table 4.1 indicates the reduction of the electrical performance relative to the pre-DH measurement. The difference between the behavior of the front and rear side may be related to the loss of the passivation of the cell that enhances recombination at the front side. This hypothesis was confirmed by the EQE curves reported in Figure 4.4b. The reduction in EQE from the front side is more evident for shorter wavelengths, whereas the reduction is stronger at longer wavelengths when the EQE measurement is performed from the rear side, confirming that the most affected surface of the cell was the front one. These photons are in fact absorbed near the front surface (i.e. on the opposite side of the p-n junction), and the photo-generated carriers cannot effectively reach the p-n junction.

The observation of the impact on module performance of water ingress from the edges (see

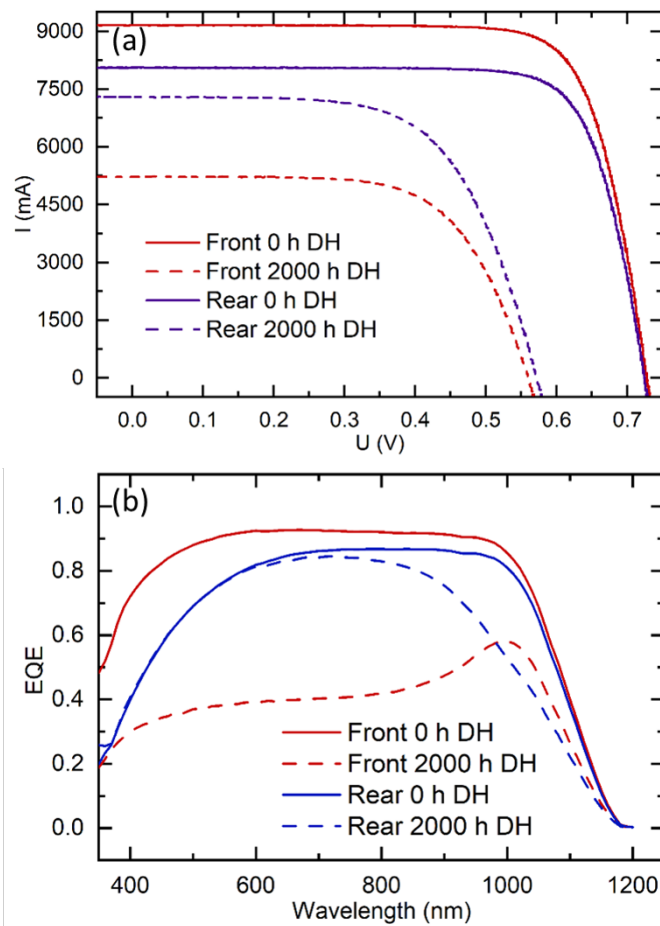


Figure 4.4: (a) I-V and (b) EQE measurements of the front (red) and rear (blue) sides of standard 1-cell G-G modules (see Figure 4.2a) before (solid lines) and after (dashed lines) 2000 hours of exposure to damp heat. The degradation is much more pronounced at the front side of the cell.

EL images in Figure 3.2f) was reinforced by the results of the DH test performed on the SHJ modules made with the same bill of materials with an added PIB edge sealant seen in Figure 4.2c. These samples – for which we expected no water ingress in the laminate - were in fact extremely stable during exposure to DH for 3000 hours, as reported in Figure 4.5, clearly confirming the role of water.

### 4.3.2 Analysis of the metallization

The diffusion of moisture inside the module can impact the stability of the metallization scheme of the solar cell.

Unlike other cell technologies, such as back surface field (BSF) and passivated emitter rear cell (PERC), for which the cell interconnect ribbons are soldered to the busbars using a paste,

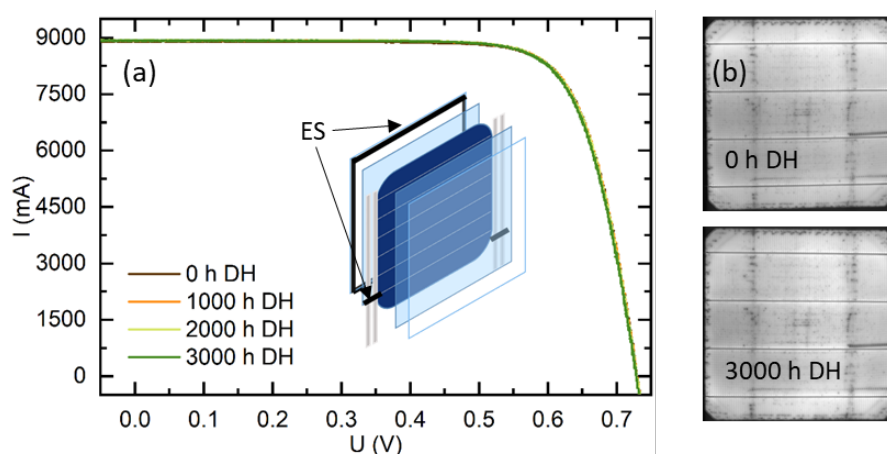


Figure 4.5: (a) I-V curves and (b) EL images of 1-cell modules encapsulated with EVA and an edge sealant (see Figure 4.2c) after 3000 hours of DH exposure.

SHJs require low-temperature processes (i.e.  $T < 200^\circ\text{C}$ ) to interconnect cells. Otherwise the *a-Si* passivating layers will be damaged, and the passivation properties will be destroyed. Interconnection was done by gluing the ribbons to the cell busbars using an electrically conductive adhesive (ECA). Unlike soldering, ribbon-gluing using ECA pastes is a process with a much poorer track record.

We characterized degraded standard G-G single-cell SHJ modules to assess the stability of the cell interconnects and the ECA paste. SEM images were taken as shown in Figure 4.6b to examine the cross section of the fingers and the ECA. Figure 4.6c shows the module cross section along with the ribbons and the corresponding close-up in Figure 4.6d. The cross sections are consistent with the EL image in Figure 4.6a. In fact, the only remaining bright spot after the aging test was the portion near the busbars. The ECA paste looked stable, and there were no voids or detachment between the busbar and the soldered ribbon. The blackening of the cell surface observed in the EL image cannot be correlated to finger degradation. Figures 4.6e and 4.6f confirm that the presence of diffused water did not affect the adhesion of the silver lines, and that there was no significant sign of degradation nor were any defects detectable.

These results confirmed that the **interconnects are not the cause of the module degradation**.

### 4.3.3 Characterization of the encapsulant

The results of the chemical characterization of the EVA polymer exposed to DH were presented in Section 3.3.2. These results showed that the encapsulant was stable, so that, as with the effect of moisture on the metallic interconnections, we are able to exclude any impact of the polymer in the observed degradation of the SHJ module upon exposure to DH.



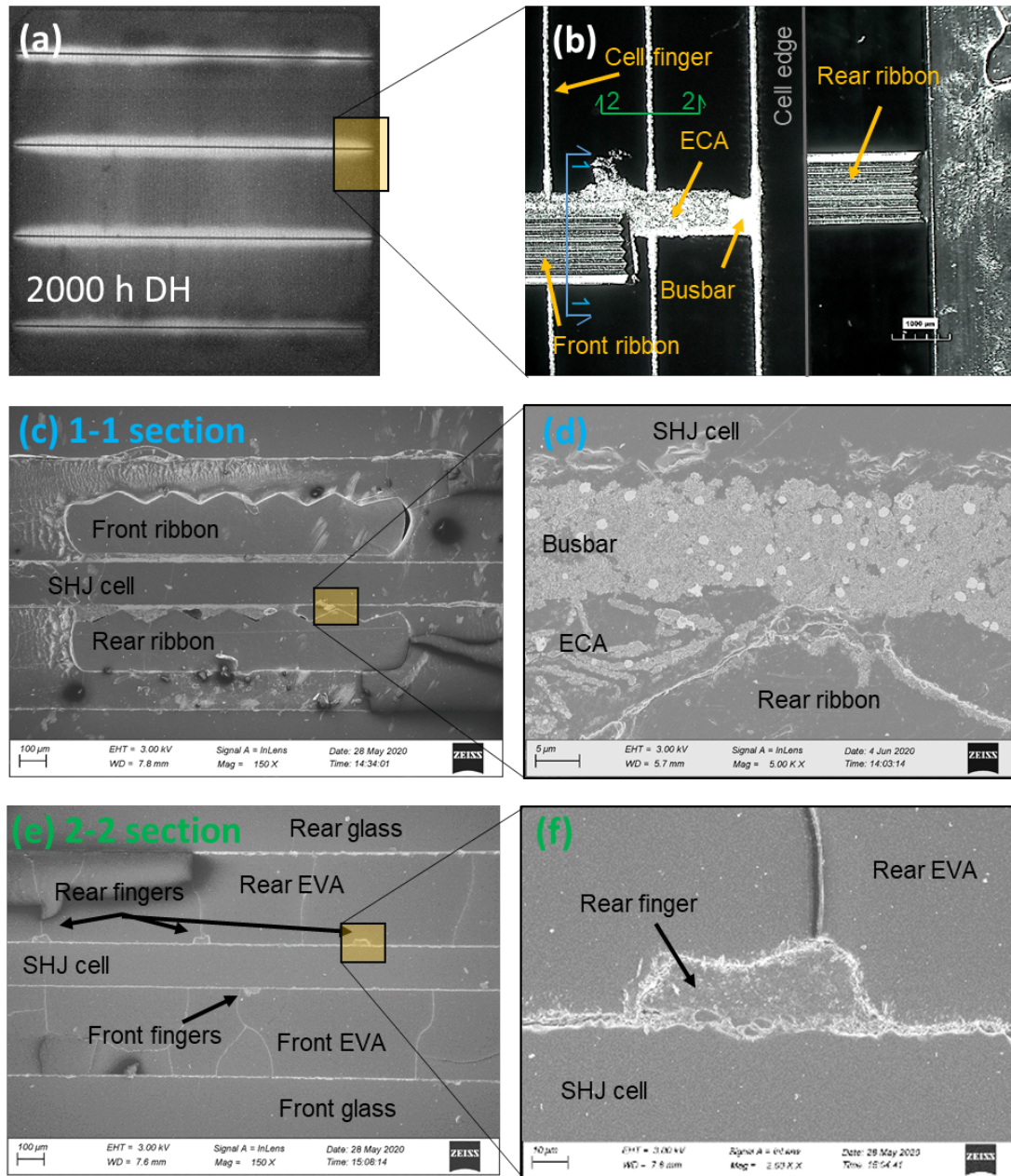


Figure 4.6: (a) EL image of the standard G-G 1-cell SHJ module (see Figure 4.2a) after 2000 hours of damp heat exposure. (b) Optical microscopy image of the cell's top view showing the metallization scheme and where the two cross sections were taken (1-1 perpendicular to the busbar line, and 2-2 perpendicular to the finger line). (c and d) SEM images of the 1-1 cross section used to investigate the stability of the ECA and the busbars. (e and f) SEM images of the 2-2 cross section used to observe the finger morphology. SEM images were taken by PV-Lab colleague Quentin Jeangros.

#### 4.3.4 Effect of moisture on passivating cell layers and interface

To examine the impact of moisture on the different cell layers, we subjected unencapsulated coated Si wafers to DH and looked for modifications of the cell surface using FTIR spectroscopy. Figure 4.7 reports the transmittance spectra recorded during the aging test of an *aSi:H* double-coated sample. The peak at  $610\text{ cm}^{-1}$  was attributed to the phonon absorption of the silicon lattice [122]. Non-aged samples also showed the presence of the Si-O bond at  $1100\text{ cm}^{-1}$ . This was probably due to the presence of a native oxide layer formed after exposure to the air. During damp heat, new peaks were detected at  $680\text{ cm}^{-1}$ , in the  $1500\text{--}1750\text{ cm}^{-1}$  range and from  $3700$  to  $4000\text{ cm}^{-1}$ . Those peaks were assigned to Si-C [123], the O-H groups of water molecules, and the formation of Si-OH, respectively [124]. Similar results were recently observed by Liu *et al.* [125], who also noted the formation of Si-O bonds upon exposure to a hot and humid environment.

Note that Si-H bonds were never detected. The absence of Si-H bonds could be related to the thickness of the *a-Si:H* layer, which was probably too thin (i.e. 4-5 nm) to be detected by the spectrometer. As the same spectra modifications and peak formations were obtained by analyzing symmetrical samples with the addition of the external ITO layer and on positive doped samples (i.e. *i/p a-Si:H* wafers with and with out the ITO layer) we concluded that the ITO did not act as a protective layer for the *a-Si* layers below. The measurements on the *i/p a-Si* coated Si wafers or on the same samples capped with an ITO layer are shown in Appendix C: the same results (i.e. formation of the Si-OH and OH bonds) were observed.

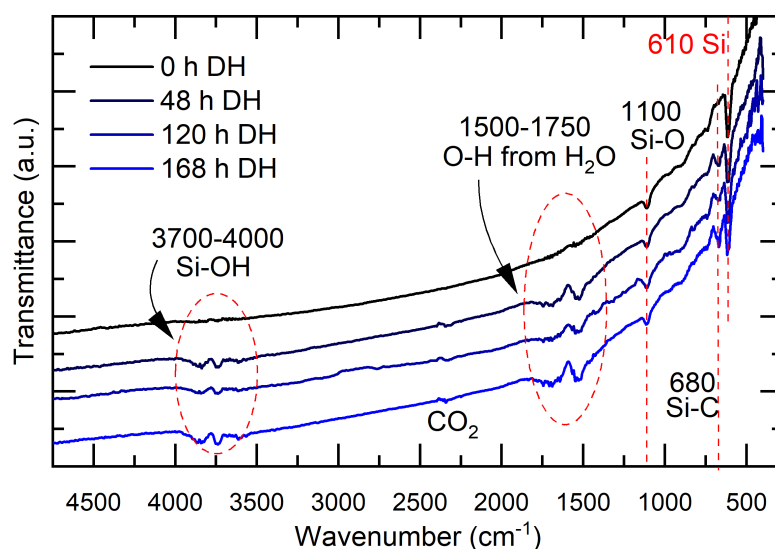


Figure 4.7: FTIR spectra performed on untetxtured Si wafer coated with *i/n a-Si* layers (Figure 4.3a) before and during damp heat aging. Upon exposure to DH, the formation of -OH group from  $\text{H}_2$  and Si-OH are observed.

### 4.3.5 The effect of moisture on different module structures

We manufactured and subjected to DH this set of samples: (1) a bare SHJ cell, (2) a SHJ encapsulated with EVA only, and (3) a SHJ encapsulated with EVA and a polymer ETFE foil. PL images were performed on all samples (at the start, after 500 hours, and after 1000 hours) and were compared to those of the glass-glass single-modules as shown in Figure 4.8.

As for the coated Si wafers, bare SHJ cells were fully exposed to a highly humid environment with no protection. In Section 3.3.2, we observed that the kinetics of the degradation were fast when the water concentration was almost at the saturation value. Thus, we expected a significant degradation (i.e. reduction of the PL signal) after a few hours of exposure – for which we assumed a condition of complete water saturation. Contrarily, as reported in Figure 4.8a after 500 hours, the PL showed a good signal on a large portion of the cell surface. We then extended the test to 1000 hours, and performed the analysis again. Despite a significant reduction in the PL signal, the cell remarkably exhibited some luminescence. Surprisingly, even better results were obtained on the SHJ encapsulated with EVA only, as shown in Figure 4.8b. The correlated PLs recorded during DH exposure for 1000 hours showed that the presence of only encapsulant foils did not lead to a significant degradation of cell performance, even if we expected the polymeric encapsulant to reach full water saturation after only some dozens of hours in a highly humid environment. Therefore, the exclusive role of water, in the previously observed module degradation, should be abandoned. Further, the formation of Si-OH bonds, which can be expected in the *a-Si* layers or at the *a-Si/c-Si* interface, is not enough to explain the whole picture. In other words, SHJ cells and modules have always been thought to be very sensitive to the presence of water (or moisture), but these results confirmed that this is not true.

Similarly, the PL images on the glass-free module in Figure 4.8c (manufactured with an ETFE foil in place of the external glass covers), demonstrated that this module structure is much less sensitive to water than the conventional glass-glass structure, in Figure 4.8d.

This was confirmed by comparing the I-V characteristic curves of the *glass-free* module with those of the G-G module. The results are reported in Figure 4.9: the strong  $I_{sc}$  reduction visible in the G-G layout is not observed when the ETFE layer was used.

If we focus on the PL images shown in Figure 4.8 (and on the I-V curves of Figure 4.9), we observe the impact of a water-induced degradation process after 1000 hours of operation in DH. A clear but limited reduction of the PL signal can be seen for the bare cell, and the *glass-free* module. Surprisingly, the *EVA-only* sample exhibited a lower reduction of the PL signal. The module structure that was most impacted by the DH test is the glass-glass structure, to our astonishment, it is the structure that we would have expected to provide the most substantial protection to the cell. These results point to the role of the glass cover in the degradation process that is triggered by an interplay between the presence of water and glass. Figure 4.10 summarizes and compares the main electrical parameters (i.e.  $P_{max}$ ,  $I_{sc}$ ,  $V_{oc}$  and FF) of the different tested SHJ encapsulation schemes.

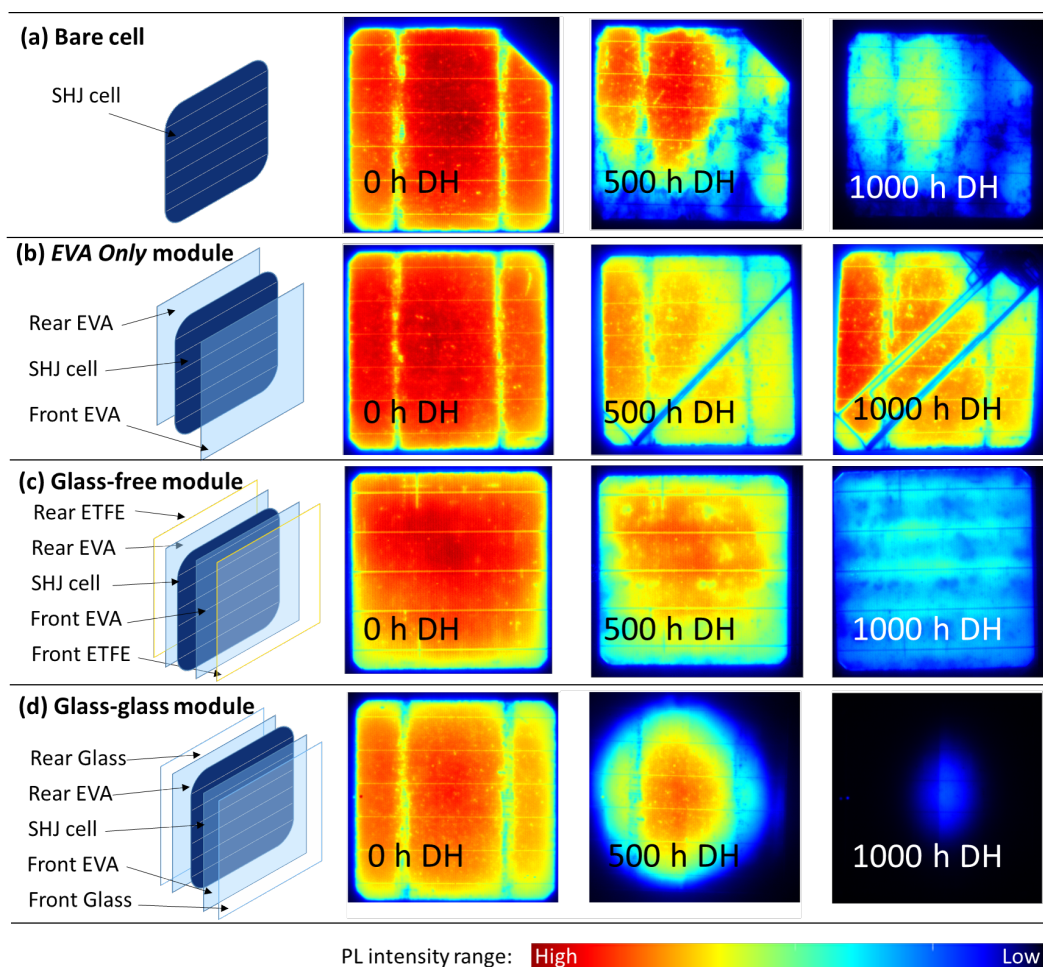


Figure 4.8: Photoluminescence images of the different module designs after 0, 500, and 1000 hours of DH test: (a) bare cell, (b) *EVA-only* (i.e. EVA-SHJ cell-EVA), (c) *glass-free* module with the replacement of the front and rear glass plates with the polymeric film of ETFE, (d) standard SHJ G-G module encapsulated with EVA.

#### 4.3.6 Glass corrosion and the role of sodium

Sodium (Na) (contained in standard solar-grade soda-lime glass) is generally associated with potential-induced degradation (PID), with an electric field extracting sodium ions ( $\text{Na}^+$ ) out of the glass. However, two recent publications have pointed at the role of Na in the DH degradation of SHJ cells (in the absence of an electric field) [125, 126].

In fact, the high temperature and humidity of the damp heat test can "*accelerate changes of surface and bulk chemistry representative of leaching process*" as recently reported by Guiheneuf *et al.* [127]. Their findings highlight the role of non-bridging oxygens (NBO) in the glass network: "*NBOs generate breaking links in Si-O-Si configuration and dangling bonds Si-O•. (...) It seems that monovalent cations like Na and K have a strong tendency to be released from the glass surface to a gel layer because hydration induces the bond breaking between cation*

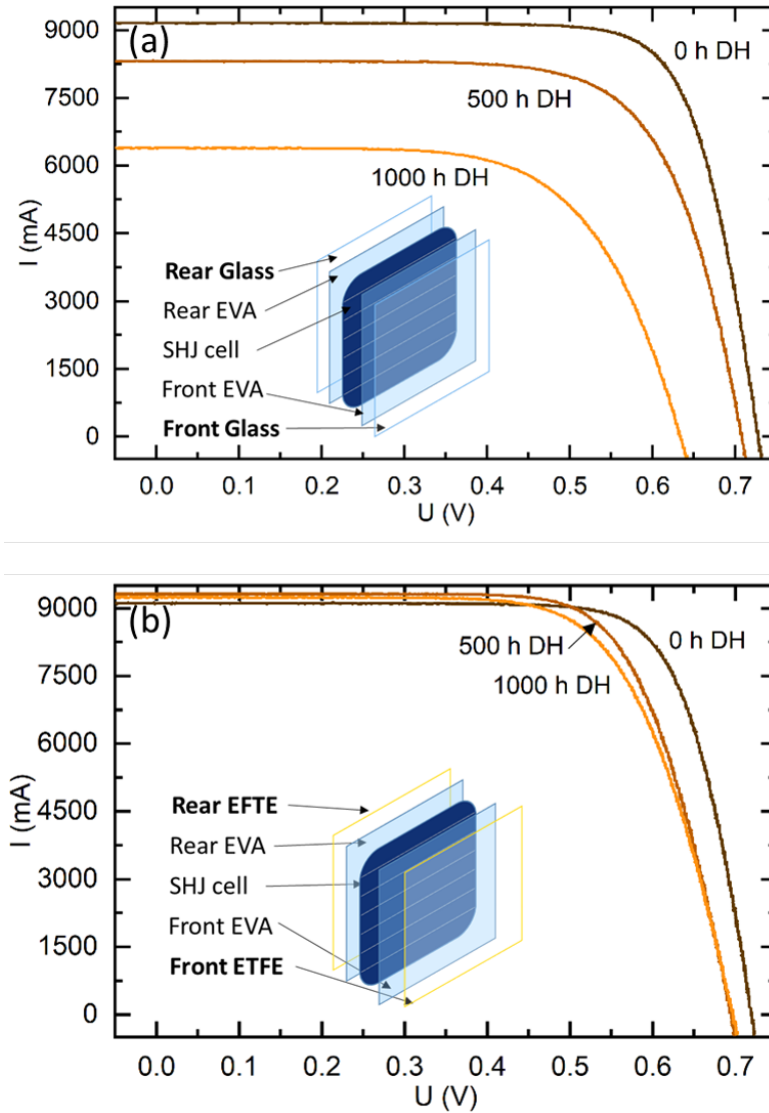


Figure 4.9: I-V characteristic curves recorded during damp heat aging test of standard 1 SHJ cell G-G module (a) and *glass-free* module with the glass plates at the front and rear side replaced by two ETFE foils (b).

and NBO". The corrosion mechanism, i.e. leaching process, generates  $\text{Na}^+$  ions bonded with  $\text{OH}^+$  groups which get dissolved in the water layer condensed onto the glass surface, up to a concentration of approximately 1at.-% after 1000 hours of exposure in DH conditions.

Our observations tend to confirm and reinforce this hypothesis and are pointing to a **combined role of water and Na in describing the DH degradation of SHJ cells**. Diffused water inside the EVA triggers the leaching corrosion mechanism. The released NaOH ions at the EVA/glass interface are then incorporated into the *wet* EVA. This aqueous solution ( $\text{NaOH}_{aq}$ ), according to our hypothesis, can percolate through the encapsulant and reach the EVA/cell interface.



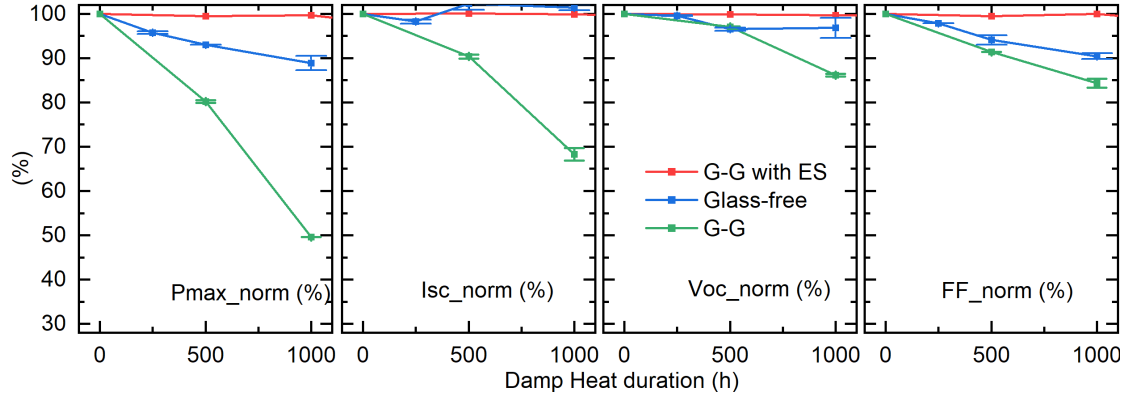


Figure 4.10: Normalized I-V electrical parameters of SHJ-EVA modules with different encapsulation structures taken before and during the execution of a DH test: standard G-G laminate (green curves), a G-G with the addition of an edge sealant (red curves), and the *glass-free* scheme where the glass plates are replaced with ETFE foils (blue curves).

#### 4.3.7 Na<sup>+</sup> droplet test

To test our hypothesis (the role of Na and the creation of an aqueous solution containing NaOH), we prepared water solutions with different NaOH concentrations (i.e. 0.01%, 0.05%, 0.1%, w/w), a test previously proposed by Adachi *et al.* [128]. We then placed two drops of each solution on top of the front side of an unencapsulated SHJ cell and let them evaporate before placing the cells in a DH chamber. The samples were characterized with PL imaging before and after the evolution of the DH test, and the results are reported in Figure 4.11a. As a comparison, the same test was run by using the more DH stable PERC cells (see Figure 4.11b). In fact, as previously shown in Chapter 3, **encapsulated PERC cells proved to be stable** during the whole 2000 hours of aging test without signs of degradation. The results confirmed the poor stability of the SHJ cell in the presence of Na<sup>+</sup> ions. A solution concentration of 0.01% w/w was sufficient to reduce the luminescence of the cell after only 4 hours of exposure to DH. Additionally, the part of the cell that was not in contact with a sodium droplet did not degrade, even if exposed to the high humid environment of the climatic chamber. The PERC cell shows some localized reduction in PL intensity at the higher concentrated NaOH droplet site (i.e. 0.05%, 0.1%, w/w) after 24 hours. This can be attributed to the high pH value of the NaOH solution, which can eventually attack the silicon solar cell. In fact, when using a less harsh Na<sup>+</sup> solution (i.e. NaCl<sub>aq</sub>) was used, PERC cells did not show any sign of degradation, whereas SHJs showed similar results (see Appendix D). This test reinforced the fact that **we are un-covering a degradation mechanism specific to SHJ technology**.

## 4.4 Degradation model

We now propose a **detailed microscopic model** which attempts to explain the root cause behind the observed degradation mechanism and the extreme sensitivity to water (and Na) of

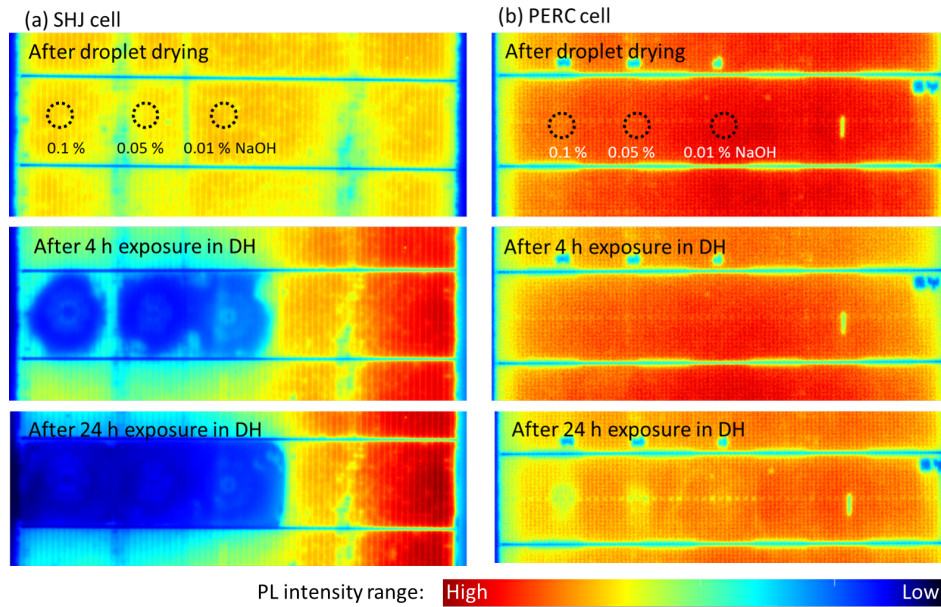


Figure 4.11: Droplet test performed with a NaOH aqueous solution . PL images of SHJ (a) and PERC (b) cells taken after the droplets drying for different NaOH concentrations (i.e. 0.01%, 0.05%, 0.1% w/w. ), and after 4 and 24 hours of exposure in damp heat conditions.

SHJ cells/modules. The model is sketched in Figure 4.12:

1. In our model, the role of EVA (with a relatively high WVTR and water absorption, compared to other encapsulants such as POs) is instrumental in allowing a progressive ingress of water from the edges, which tends to reach a saturation level. This is confirmed by EL, PL imaging and water diffusion modeling. The use of an edge seal or an encapsulant with a low WVTR (and water absorption coefficient) prevents (or delays) the ingress of water without triggering the corrosion process.
2. Water diffusion modeling (confirmed by EL and PL) tells us that the encapsulants reach water saturation relatively fast at the edges (after only 500 hours of exposure to DH), progressing towards the module center, where saturation is nearly reached after 1000 hours.
3. The contact of water with the inner face of the front (or rear) cover glass can promote a thermally activated corrosion process, described by Guiheneuf [127], in which the molecular water reacts with monovalent cations (like  $\text{Na}^+$ ) that are present in the soda-lime glass (whose composition is about 70% silica ( $\text{SiO}_2$ ), 15% soda (NaO), and 9% lime (CaO)). The cationic atoms are released from the glass network to the water film where they accumulate as a soluble precipitate with a mixture of molecular water and hydroxide ions [127].
4. The highly soluble NaOH forms an aqueous solution ( $\text{NaOH}_{aq}$ ) which is able to diffuse

through the polar matrix of the EVA polymer, reaching the SHJ cell surface. Depending on the morphology of the sputtered TCO layer (i.e. grain size, density of grain boundaries, presence of voids, etc.), it may prevent (or delay) the diffusion of the NaOH aqueous solution as reported in [126]. In our case, it eventually reaches the *a-Si:H* passivating layers and the *a-Si/c-Si* interface creating a loss in the cell's passivating properties, as confirmed by PL images. Once the Na reaches the *i/n a-Si:H* interface, it acts as a recombination state [129] reducing the passivation of the cell. Very likely, some Si-OH bonds – displacing Si-H – are contextually created at the cell interface, as observed by FTIR on the coated wafers exposed to DH (see Figure 4.7). This may similarly have an impact on the cell's properties, but the PL images clearly emphasize the additional role of Na in the degradation process (see Figure 4.8) when we compare the reduction of the PL signal after 500 and 1000 hours for the samples manufactured with a soda-lime glass cover (containing Na), the samples encapsulated without a glass cover, and the bare cell.

## 4.5 Mitigation strategies

To reduce the observed degradation, multiple strategies can be adopted at different levels:

### 1. Cell level - development of DH resistant cells by:

- (a) Depositing a more stable silicon nitride ( $\text{SiN}_x$ ) as in the case for the PERC cell (see Figure 4.11b);
- (b) Depositing a double anti reflection coating of high quality  $\text{SiN}_x$  and  $\text{SiO}_x$  as recently reported by Liu *et.al* [125];
- (c) Optimizing the TCO layer morphology to be as described above, and possibly thicker – could be another strategy to mitigate (or delay) the insurgence of the problem.

### 2. Module level:

- (a) Use of an edge sealant, as already reported in Section 4.3.1 (see Figure 4.5);
- (b) Use of an encapsulant with a lower WVTR value, such as a PO-based formulation: Figure 4.13 shows the I-V curves, and the corresponding EL images of single-cell SHJ G-G encapsulated with a poly-olefine (PO) formulation. The better stability of the electrical parameters during a DH test, up to a duration of 3000 hours, confirmed that the enhanced moisture barrier of a PO encapsulant reduces the water diffusion inside the module and the consequent glass degradation mechanism.
- (c) The deposition of a coating on the inner surface of the glass could be another strategy to avoid the generation and release of  $\text{Na}^+$ .



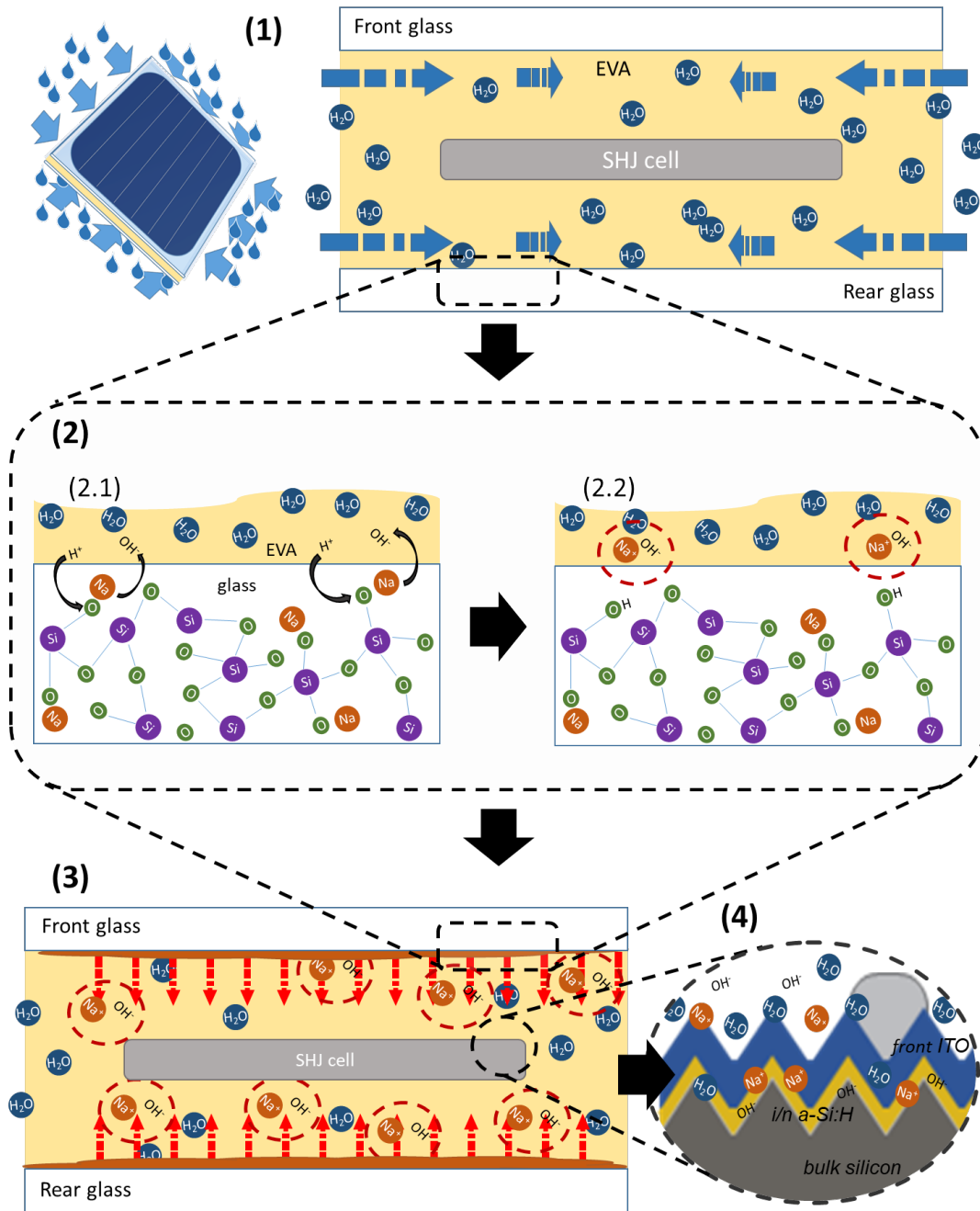


Figure 4.12: Schematic of the proposed microscopic model for the degradation mechanism of G-G SHJ modules encapsulated with EVA. (1) Water ingress through the EVA from the module edge; (2) Glass corrosion process: leaching occurs in the presence of water at the EVA-glass interface with the release of  $Na^+$  and  $OH^-$  ions which are dissolved in the encapsulant; (3)  $NaOH_{aq}$  solution diffuses through the EVA to the cell surface; (4)  $Na^+$  and  $OH^-$  ions cross the ITO and degrade the passivation layer at the  $a-Si:H$ /bulk Si interface.

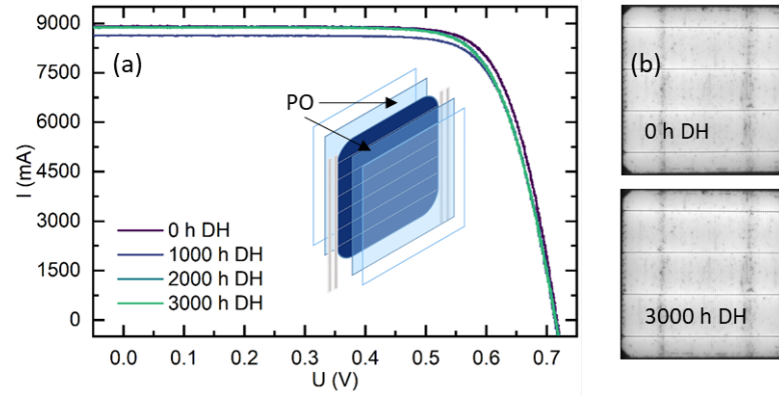


Figure 4.13: (a) I-V curves and (b) EL images of single-cell SHJ modules encapsulated with EVA and the use of the edge sealant after 3000 hours of DH exposure.

## 4.6 Conclusions

In this chapter, we studied the particular degradation mechanism related to SHJ modules encapsulated with a standard EVA under damp heat aging test. The incompatibility between SHJ and EVA is well known. In fact, SHJ cells are usually encapsulated using more recently developed PO formulations. However, POs are slightly more expensive and are more difficult to process, compared to the EVA. It is important to understand the degradation mechanism to research and propose suitable mitigation strategies.

The degradation was first correlated to the moisture diffusion from the open edges of the module through the EVA. However, by studying different sample configurations, we observed that the presence of the water alone was not sufficient to account for the considerable power loss occurring during damp heat. Particularly, we observed that the standard G-G structure underwent a loss of current and  $V_{oc}$ . Nevertheless, when the standard soda-lime glass plates were replaced with a sodium-free cover, the degradation was reduced, particularly the  $I_{sc}$  electrical parameter remained stable. We correlate the degradation with the presence of NaOH coming from corrosion of the glass, which gets dissolved in the moisture.

To our knowledge, we are the first to propose a detailed microscopic model explaining the sensitivity to water and DH of SHJ technology, when using EVA encapsulant and glass. In reality, the presence of water is only a contributing factor, as clearly indicated by the fact that to trigger the worst observed degradation modes, both water and glass are needed. The degradation phenomenon is not observed either by eliminating the presence of water is eliminated (with an edge seal or a low WVTR encapsulant) or the glass is replaced.

Our degradation model proposes the diffusion of an aqueous solution of NaOH through the encapsulant, due to the non-optimal WVTR of the EVA, and its intrinsic polarity. The  $\text{Na}^+$  and  $\text{OH}^-$  ions cross the ITO layer and react at the intrinsic passivation layer. Particularly, the hydroxide forms new bonds with the  $a\text{-Si}$ , by replacing the less stable  $a\text{-Si:H}$  bonds.  $\text{Na}^+$  ions

#### **Chapter 4. Insights into the sensitivity of SHJ modules to damp heat: a microscopic model**

---

instead act as recombination elements, especially on the n-doped side.

Finally, we evaluated two possible mitigation strategies. Specifically, the encapsulation scheme can be modified by (2a) adding an edge seal to improve the moisture barrier or (2b) replacing the EVA with a PO formulation with a lower WVTR value than the EVA.

Other potential mitigation propositions need further investigation. This work confirmed that moisture can diffuse inside a glass-glass PV module from the open edges. The studied degradation mechanism is specific to the SHJ cells. Al-BSF and PERC showed better stability in the presence of humidity. However, multiple outdoor stresses act simultaneously on the module under operational conditions. In a G-G configuration, when water is present inside the module - diffusing from the environment or already present inside the module after lamination - it cannot be diffused out as in the case of a breathable back-sheet. The trapped water, coupled with the UV radiation stressor, can potentially accelerate polymer degradation and cause premature failure of the module.

## 5 The Effect of Storage Conditions on the Long-Term Stability of EVA

### Summary

In this chapter, we evaluate the effect of storage conditions of uncured encapsulant rolls and the potential consequences on PV module performance. We show the impact of residual water trapped inside laminated double glass PV modules after lamination and during UV exposure. We focus on EVA and its stability over  $630 \text{ kWh/m}^2$  UV exposure (approximately equivalent to 10 years of outdoor exposure in a Central European country as Switzerland). Three storage conditions were tested by simulating different moisture contents including a dry environment (i.e.  $\text{RH}=30\%$ ), one realistic situation where the uncured encapsulant foils are not immediately used after cut and they are left in an uncontrolled environment (i.e.  $\text{RH}=65\%$ ), and one extreme poor storage condition (i.e. EVA is soaked in water). The presence of water during lamination had no apparent impact on module quality and performance after the fabrication but only became apparent during the aging test, after UV exposure of  $15 \text{ kWh/m}^2$ . The module power loss was directly related to the EVA chemical and physical degradation and varied depending on the storage history. Results show that when the storage is not too harsh, its effect can be somehow mitigated.

### 5.1 Introduction

The choice of a proper encapsulant is critical to ensuring optimal long-term performance of a module [130]. This is even more important with the rise of the solar cells with passivation layers, including passivated Emitter and Rear Cells (PERC) and silicon heterojunction (SHJ) cells. Despite not being the best performing encapsulant, Ethylene Vinyl Acetate (EVA) is still the primary polymer in use in the PV industry thanks to its long track record and good quality-price ratio. The instability issues of EVA during long-term outdoor exposure are, however, well documented in literature [52, 53, 65, 72]. UV radiation, moisture, and exposure to elevated temperatures are all stress factors that may lead to a degradation of polymers. This may induce a discoloration of the material, with reduction of transparency and consequently of the

photocurrent of the module. Acetic acid is one of the by-products of EVA degradation. In the presence of moisture and heat, a hydrolysis reaction will occur to produce acetic acid [109], lowering the pH and potentially leading to a corrosion of the metallic interconnections [110]. Moreover, with the addition of the UV radiation, the photodegradation initiates faster from vulnerable vinyl acetate groups, followed by further degradation in the main chain by Norrish type chemical reactions [131]. The EVA formulation has improved over the years with the modification of additives to reduce the degradation rate.

Material and process quality are critical to product quality and lifetime at all manufacturing stages, including before production. In fact, a PI Berlin survey of over 250 PV manufacturers observed that material storage and preparation is a major factor for a good PV module manufacturing quality [132]. Additionally, the limited number of modules (typically less than 10) tested by the manufacturer for qualification certificate is not representative of the whole production amount [44] and assumed flawless modules could instead rapidly degrade after installation because of poor material quality. It is good practice to store uncured rolls of encapsulants in dark, dry (relative humidity, RH <50%), and cool place (<30°C) before they are used [133]. Moreover, some encapsulant manufacturers state that the rolls should not be stored for more than six months and that active humidity control is necessary after the roll is open [134]. However, proper storage conditions are not always maintained, and seasonal variations in temperature and humidity may be present in the storage room or the manufacturing line. Additionally, after the roll is removed from its packaging, it should be used in a short time interval. Prolonged exposure to an uncontrolled environment and its usage after the recommended expiration date can affect the long-term performance of the module. Loss of adhesion, non-uniform cross-linking, and ultimately faster module power loss are reported as consequences of a low-quality encapsulant [135–137].

### 5.2 Experimental details

In this work, we manufactured single-cell glass-glass modules using conventional Al-BSF (Aluminum Back Surface Field) crystalline silicon (c-Si) cells and a commercial EVA. The EVA roll was stored in different conditions before lamination. Modules were then subjected to accelerated UV aging tests, with electrical performance and material changes monitored periodically.

Al-BSF cells were selected because of their presumed better UV stability with respect to newer architectures, such as PERC and SHJ (see results in Appendix E) [138, 139]. This allowed us to exclude the possibility of UV-induced cell degradation and instead attribute module changes to encapsulant degradation.

Before the lamination process, the uncured encapsulant polymer sheets were stored in varied conditions to simulate daily/seasonal variations that might occur if they are not kept under controlled temperature and humidity conditions. After lamination, modules were then exposed to UV up to a cumulative UV dose of 630 kWh/m<sup>2</sup>. This corresponds to an

Table 5.1: EVA storage conditions.

ID code	Temperature [°C]	Rel. Humidity [%]	Time [days]
<b>EVA-30</b>	20	30	5
<b>EVA-65</b>	30	65	5
<b>EVA-100</b>	20	soaked in water	5

outdoor exposure of about 10 years in a mid-latitude country with a temperate climate, such as Switzerland ( $\sim 60 \text{ kWh/m}^2/\text{y}$  of UV).

Module performance was regularly accessed using visual inspection, illuminated current-voltage (I-V) measurements, and electroluminescence (EL) images. Additionally, laminated glass-glass samples with only one layer of EVA (i.e. without solar cells) were fabricated to monitor the physical and chemical degradation of the polymer.

### 5.2.1 Storage conditions

Polymer manufacturers give optimal storage conditions for PV encapsulants [134]. For EVA, in general, an optimum temperature of  $22^\circ\text{C}$  and a relative humidity  $\leq 50\%$  are recommended after the roll is open [133]. In our experiment, the encapsulant foils were subjected to three different preconditioning conditions for five days before lamination (see Table 5.1) to simulate seasonal humidity variations that may occur in a manufacturing line or under non-optimal storage conditions. The EVA-30 foil corresponds to an uncured encapsulant roll stored under optimal conditions, as recommended by the supplier. The storage room was kept at constant relative humidity and temperature in the dark. EVA-65 reflects the situation in which the roll was kept in an uncontrolled indoor environment with a high RH. This was done by storing polymeric sheets inside a climatic chamber. The EVA-100 encapsulant is an extreme condition in which the roll was soaked in water. Desorption of water for EVA-65 inevitably occurs in the time between removal from the climate chamber, module layup, and lamination process (see Appendix F). So while the EVA-100 storage conditions are certainly unlikely, they ensure that moisture is present during the lamination process.

### 5.2.2 Samples design and fabrication

For each of the three EVA storage conditions, single-cell modules with c-Si Al-BFS solar cells were manufactured (glass/EVA/cell/EVA/glass). Additionally,  $7 \times 7 \text{ cm}^2$  coupons were prepared in order to check the degradation of the EVA. Some characterization techniques require extraction of the EVA, so two different sample structures were used (Figure 5.1):

1. Glass/EVA/cell/EVA/glass: single-cell modules with c-Si Al-BSF solar cells, to monitor the impact of storage conditions on module performance;

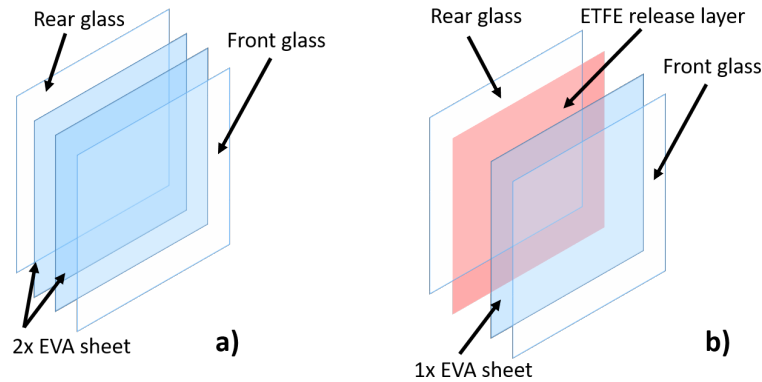


Figure 5.1: Schematic sketch of the coupons used to investigate the degradation of the EVA during UV aging: (a) G/EVA/G was used to study the optical properties; (b) G/EVA/ETFE/G was used for invasive techniques analysis such as FITR-ATR and DSC -due to the possibility of *opening up* the sample -.

Table 5.2: Aging tests conditions.

Test type	Air Temperature [°C]	Black panel Temperature [°C]	Relative Humidity [%]	UV intensity (@ 340 nm) [W/m <sup>2</sup> ]	Test duration
IEC 62788-7-2	65	90	20	0.8	630 kWh/m <sup>2</sup>

2. Glass/EVA/EVA/glass: EVA laminates to monitor encapsulant degradation, specifically the optical transmittance (Figure 5.1a);
3. Glass/EVA/ETFE/Glass: EVA laminates with an ETFE "release layer". This allowed "opening" of the modules for FTIR and DSC (Figure 5.1b).

### 5.2.3 Aging conditions

All laminates were aged using the IEC 62788-7-2 standard with A3 conditions for a total duration of 10000 hours. The setting inside the climatic chambers along with the test duration are reported in Table 5.2. The Xe-arc lamp with daylight filter has a UV dose corresponding to 63 W/m<sup>2</sup> (295 to 395 nm range).

### 5.2.4 Module inspection and performance

Visual images of samples were taken to check their appearance. The module performance was investigated by means of illuminated current-voltage (I-V) characteristics performed at standard test conditions (STC: AM1.5G, 25°C, 1000W/m<sup>2</sup>) using a LED-halogen based sun

simulator. Electroluminescence images were taken with the modules biased under maximum power point ( $V_{mpp} = 0.6V$ ,  $I_{mpp} = 7.5A$ ).

### 5.2.5 EVA properties

UV-vis-NIR spectroscopy was used to characterize the optical properties of the polymer by analyzing G/EVA/G coupons (*lamine type 2*). Spectra were recorded from 250 to 2500 nm.

To assess the effect of UV exposure on the structure of EVA, Fourier Transformed Infrared (FTIR) in attenuated total reflection (ATR) mode was used (*lamine type 3*). The spectra were recorded over the range  $650\text{-}4000\text{ cm}^{-1}$ . The measurements were obtained from an average of 64 scans.

Finally, differential scanning calorimetry (DSC) measurements were made on to verify changes in the crystal morphology and stability of the EVA (*lamine type 3*). Thermograms were recorded under a nitrogen atmosphere (80 ml/min), and the heating and cooling rate was 10 K/min. Samples of about 10 mg weight were cut from the *type 3 laminates*.

## 5.3 Results

### 5.3.1 After lamination – unaged samples

#### Module inspection and performance

After the lamination process, the module manufactured with the EVA-30 encapsulant did not show any visible defects. In contrast, the modules stored under non-optimal conditions showed a few minor aesthetic defects. As shown in Figure 5.2, modules encapsulated with EVA-65 and EVA-100 resulted in bubble formation along the edges, while visual quality above the cell appears normal. The higher the RH during the storage, the higher the dimensions and density of the bubbles, increasing in size from few millimeters up to 1 cm, for EVA-65 and EVA-100, respectively. The cell performance and properties (I-V and EL) showed no differences. This highlights the problem that quality issues may not be readily apparent from inspection on the production line.

#### EVA properties

The optical transmittance of the glass/polymer/glass samples manufactured with the three encapsulants did not show any difference between 250 and  $2000\text{ cm}^{-1}$  (results not shown here). This result is in good agreement with the fact that no difference was observed in the electrical performance of the modules manufactured with the same encapsulants.

The characterization of the chemical groups via FTIR spectroscopy for the three different stored EVA after lamination revealed characteristic bands for the unaged samples (Figure 5.3).



Typical peaks for EVA at 1370, 1463, 2850, and 2920  $\text{cm}^{-1}$  can be assigned to the symmetric, asymmetric and deformation vibrations of the  $\text{CH}_2$  and  $\text{CH}_3$  groups of the ethylene segments [89]. The absorption at 1736, 1238 and 1020  $\text{cm}^{-1}$  correspond to ester groups of the Vinyl Acetate segments [89]. The effect of the storage condition was most noticeable by the increase of the peak at 1695  $\text{cm}^{-1}$ , and became more pronounced going from EVA-65 to EVA-100. It can be attributed to  $\text{C}=\text{O}$  of a carboxylic group [140]. This means that the pre-absorbed moisture during simulated uncontrolled storage was already sufficient to trigger the generation of acetic acid. The presence of trapped water in EVA-100 was also well visible in the far IR range from 3000 to 3500  $\text{cm}^{-1}$ , a broad peak assigned to  $-\text{OH}$  groups.

Figure 5.4a compares the DSC curves of EVA-30, EVA-65 and EVA-100 recorded after the lamination. The first heating scan gives information relative to the history of the polymer, including both physical and chemical characteristics (i.e. lamination or aging effects). Following a cooling step, the second heating process is meant to erase the thermal history of the sample and shows only irreversible processes (i.e. chemical degradation). During the first heating step, EVA-30 shows the typical broad melting region for EVA with melting peaks at 46°C and 65°C [58] with an inset temperature at 42°C. These peaks are related to the existence of two predominant crystal sizes. The lower melting peak is usually named secondary crystallization peak. It is assigned to the melting of small ethylene crystals embedded in vinyl acetate (VA) units. The second corresponds to highly organized crystal polyethylene chains [58]. The other samples with EVA in non-optimal storage conditions (EVA-65, EVA-100) showed a comparably less stable crystal phase that melts at lower temperature with respect to the EVA-30. The melting temperature of the secondary crystallization peak decreases down to 41°C. Additionally, the

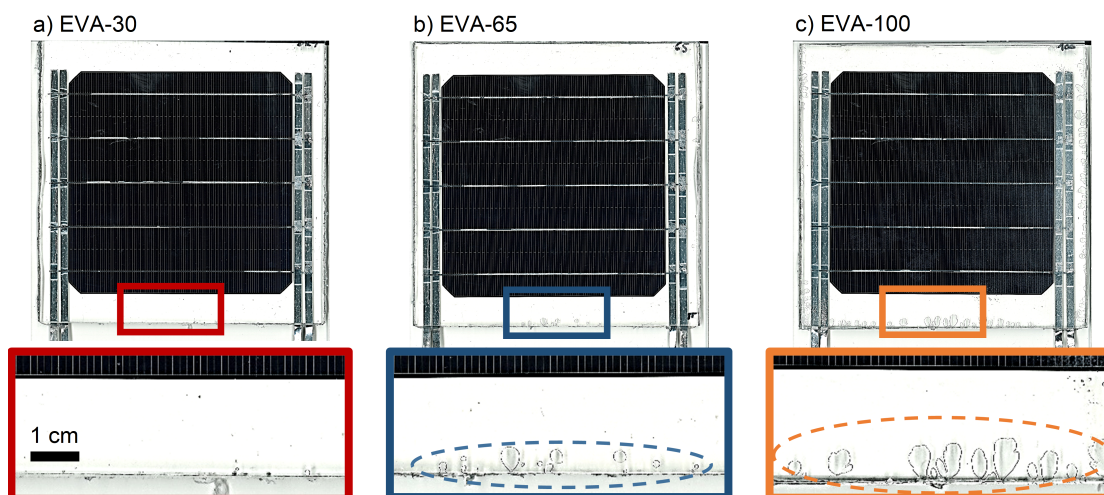


Figure 5.2: Visual inspection of the single-cell modules performed after the lamination process with a zoom in on the edges of modules highlighting the presence of bubbles for laminates encapsulated with poorly stored EVAs. The samples were encapsulated with the same polymer (EVA) stored in different conditions a) EVA-30, b) EVA-65, and c) EVA-100.

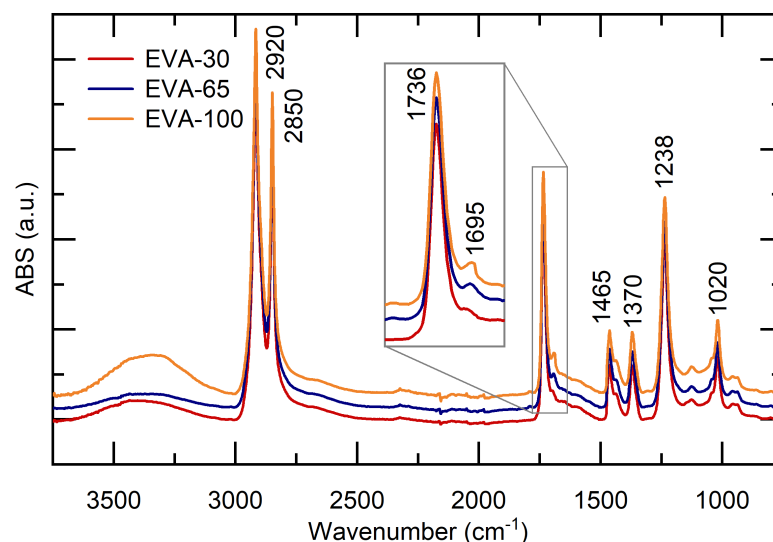


Figure 5.3: FTIR-ATR scans performed on the EVA encapsulant stored at different conditions (EVA-30, EVA-65, and EVA-100) after the lamination process. The zoom in highlights the increase in intensity of the peak at  $1695\text{ cm}^{-1}$  attributed to C=O of a carboxylic group.

primary over secondary crystallization intensity ratios (CIR) were calculated: EVA-30 showed the highest CIR of 1.55, whereas EVA-65 and EVA-100 encapsulants exhibited a lower value of 0.79. However, this effect was erased after the first cycle. The cooling and second heating scans show the same trends for all three conditions: the crystallization peak is set at  $40^{\circ}\text{C}$  during the cooling. The EVA starts to melt again at around  $65^{\circ}\text{C}$  (primary crystallization melting peak) when heated up the second time. The differences in the lower temperature melting peak and the comparable higher peak related to the second crystallization melting of EVA-65 and EVA-100 (i.e. same CIR) reveal that, regardless the RH level, a prolonged uncontrolled storage of the uncured encapsulant affects the morphological properties of the EVA developed during the curing process. The reduction of the secondary crystallization melting peak is a typical result in samples aged in damp heat conditions (i.e.  $85^{\circ}\text{C}$  and 85%RH) as reported by Ottersbock and Oreski [141, 142]. When moisture is present, the ethylene segments in VA moieties are less perfect and tend to form smaller and less stable crystals.

### 5.3.2 UV aging

#### Module inspection and performance

During UV exposure, the appearance and performance of the single-cell modules was checked at regular intervals. Figure 5.5 shows images from the visual inspections of the modules laminated with different the three different EVA preconditioning after the first  $15\text{ kW/hm}^2$  (i.e. after 250 h of aging test). By comparing these images with the ones taken directly after the lamination (see Figure 5.2), it is clear that the preconditioning had a direct effect on the aesthetic of the module, particularly on the encapsulant morphology. For the well-stored

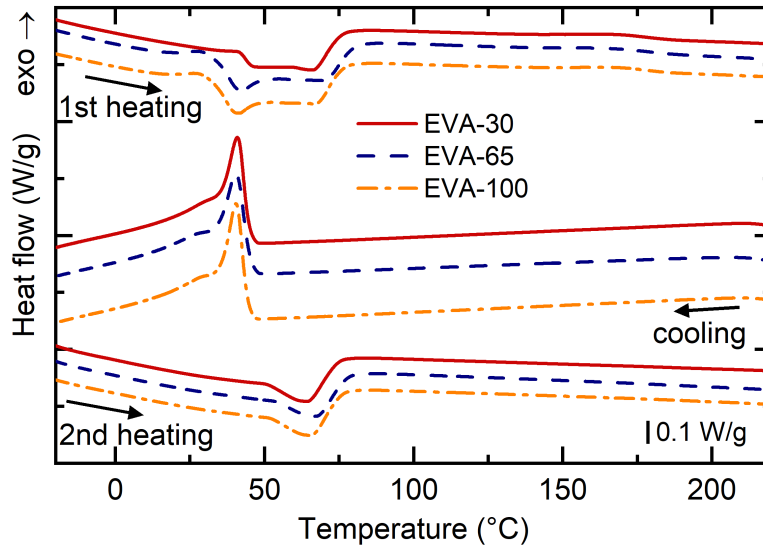


Figure 5.4: DSC thermographs performed on the G/ETFE/EVA/G coupons with EVAs stored at different conditions (EVA-30, EVA-65, and EVA-100) after the lamination process.

polymer (i.e. EVA-30 in Figure 5.5a), no defects were observed. On the module using EVA-65 (Figure 5.5b), it can be observed that the bubbles that had initially formed along the edges of the module were gettered and evacuated from the laminate. However, the extreme condition represented in the EVA-100 module (Figure 5.5c) reveals a different morphology: new bubbles were formed and pre-existing bubbles expanded, creating a network of channels across the whole module.

Figure 5.6 shows the I-V curves of single-cell modules encapsulated with EVA-30 and the related transmittance measured on G/EVA/G coupons. For modules with EVA-30 and EVA-65 the electrical performance was stable during the whole aging experiment duration (i.e. up to 630 kWh/m<sup>2</sup>).

However, for the EVA-100 module UV radiation had a major effect on performance. As shown in Figure 5.7, the power output of this sample remained stable up to a cumulative UV dose of about 200 kWh/m<sup>2</sup>, followed by a constant reduction of the current when exposed at higher UV doses. All other cell parameters remained unchanged (e.g. fill factor, and open-circuit voltage). No corrosion was detected on the ribbons, and EL (Figure 5.7) shows the Al-BSF solar cell remained stable up to a UV dose of 630 kWh/m<sup>2</sup>.

The optical measurements of the EVA shown in Figure 5.8a show the transmittance of encapsulant EVA-100 constantly decreasing in the low wavelength range starting from a dose of 189 kWh/m<sup>2</sup>. The yellowing index (YI) can be calculated, which was found to correlate with the cell current loss (Figure 5.8b). From this, it can be said that the current reduction on the module encapsulated with EVA-100 is an effect of the encapsulant discoloration, which blocks light from reaching the cell, and not corrosion or other effects.

### EVA properties

The transmittance of EVA-30 and EVA-65 was unchanged during the UV test. This contrasted with the significant changes to optical properties of EVA-100, described above in correlation to the module performance (Figure 5.8b).

The IR peaks of the EVA-30 and EVA-65 encapsulants from FTIR were similar during UV aging. The peaks remained stable during the whole aging test, up to a total UV dose of 630 kWh/m<sup>2</sup>, and showed no sign of photodegradation (see supporting information section). Figure 5.9 shows the FTIR-ATR spectra of the EVA-100 sample, which clearly underwent a strong degradation. Changes in the absorption peaks were visible starting from UV doses of about 126 kWh/m<sup>2</sup>. Notably, a reduction of the peaks at 1020 and 1238 cm<sup>-1</sup> assigned to the C-O-C stretching vibration of the VA moieties was observed [89]. Concurrently, the rise of the peak at 1160 cm<sup>-1</sup> indicated severe damage to the concentration of branches of OCOCH<sub>3</sub> acetate. This band is characteristic of the vibrational mode of C-O-C groups, which appear from the EVA chain scission [143]. The degradation of VA groups was additionally denoted by the decrease of the C=O peak at 1736 cm<sup>-1</sup>. This was replaced by the new bands at 1715 and 1720 cm<sup>-1</sup> assigned to the presence of C=O groups related to ketones generated from Norrish III photolysis reaction [131], and the shoulder at 1780 cm<sup>-1</sup> of gamma-lactones due to back-biting process. In parallel to the degradation of VA side groups, the ethylene main chain was affected during the UV aging. This was the result of intensity reduction of peaks at 1370, 2850, and 2920 cm<sup>-1</sup>, assigned to stretching and deformation vibration bands of ethylene and methylene groups. Note that we were able to record FTIR spectra of EVA-100

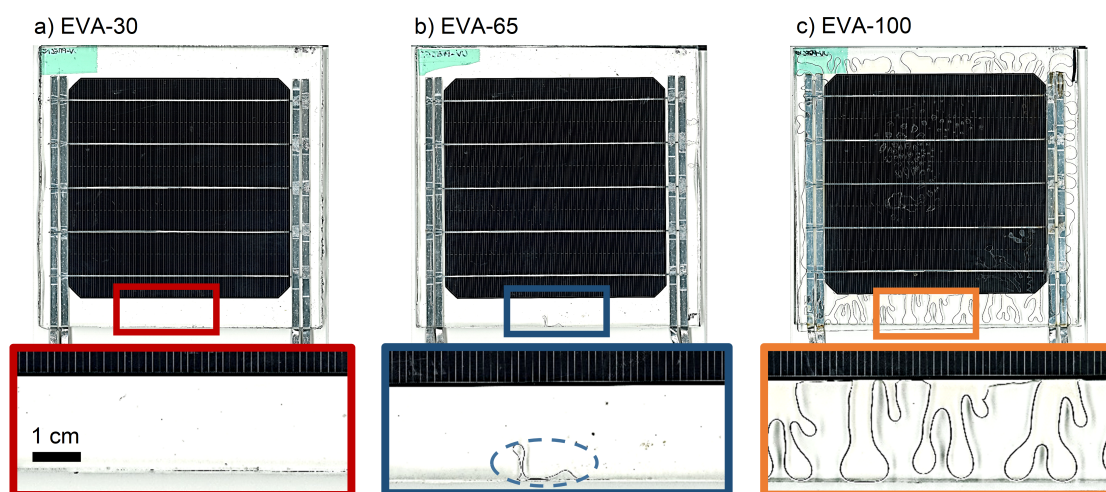


Figure 5.5: Visual inspection images of single-cell modules taken during UV aging (UV dose 15 kWh/m<sup>2</sup>) with a zoom in on the edges of modules. Samples encapsulated with EVA-30 (a), show no visual defects; in module encapsulated with EVA-65 (b) bubbles generated after lamination are gettered and evacuated from the edges; laminates with EVA-100 (c) clearly show that bubbles had spread on the whole module perimeter.

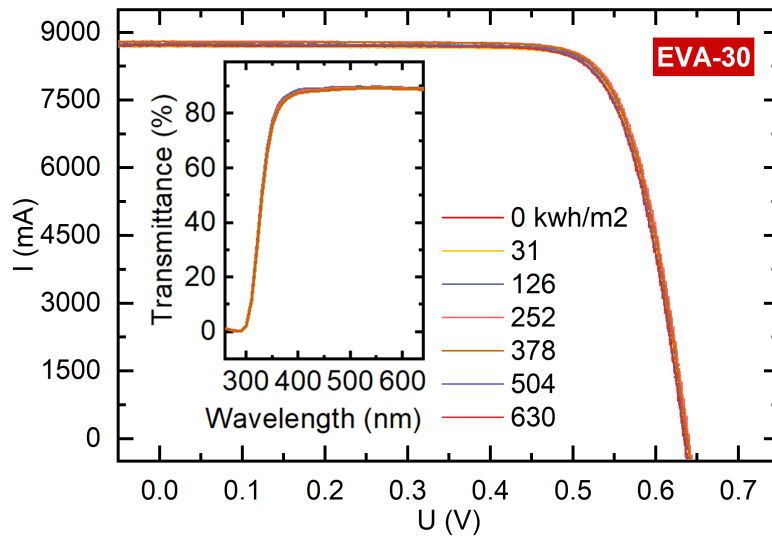


Figure 5.6: I-V curves of 1 cell modules and transmittance measurements of G/EVA/G samples encapsulated with well stored EVA-30, during UV aging (up to a total UV dose of 630 kWh/m<sup>2</sup>).

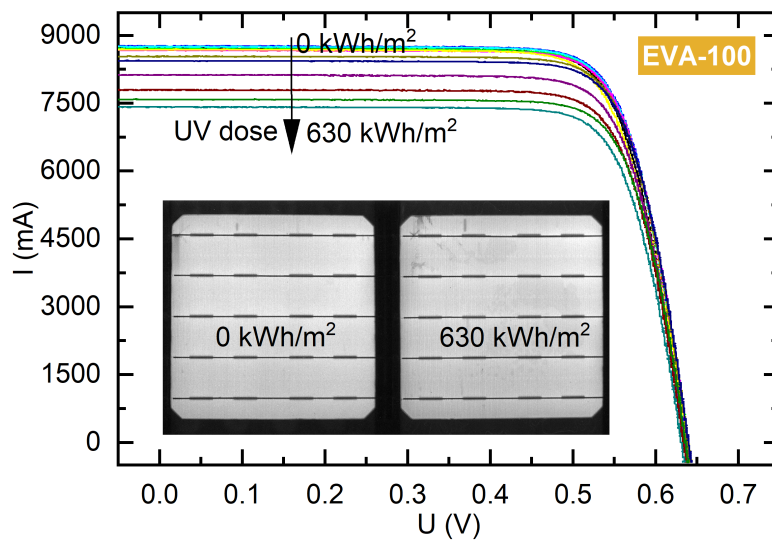


Figure 5.7: I-V curves and EL images of 1 cell modules encapsulated with EVA-100 during UV aging (up to a total UV dose of 630 kWh/m<sup>2</sup>).

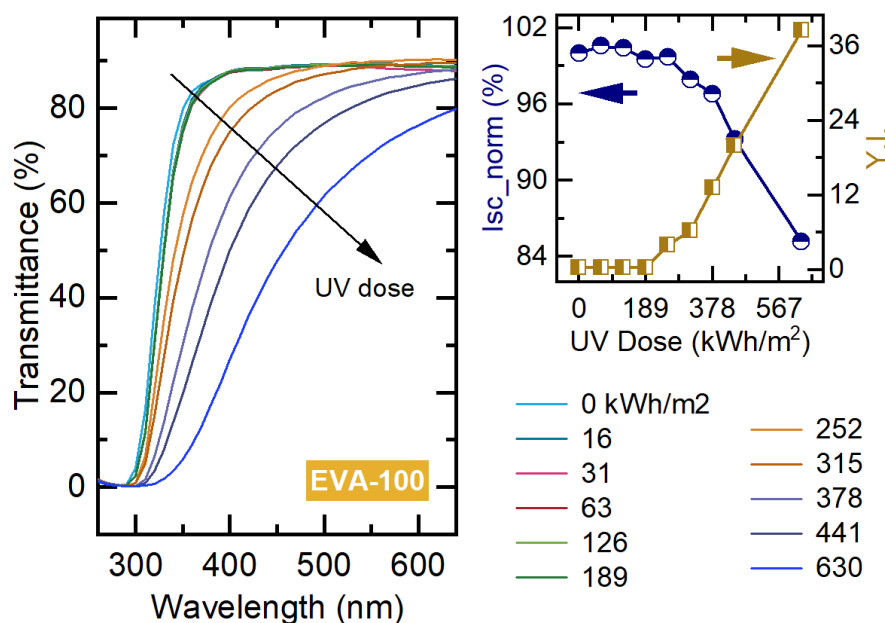


Figure 5.8: a) Transmittance changes of G/EVA/G samples in the UV-Vis range and b) correlation between  $I_{sc}$  and Yellowing Index of EVA-100 samples during UV aging, up to a UV dose of 630 kWh/m<sup>2</sup>.

only up to a total UV dose of 441 kWh/m<sup>2</sup>. After this dose, the encapsulant was too brittle to be measured by ATR. These chemical and structural changes closely match with recent works on the degradation of EVA aged by combined UV and high RH stresses [144].

DSC measurements of the EVAs were performed about halfway through the test, after a UV dose of 278 kWh/m<sup>2</sup>. Results for the three different EVAs are shown in Figure 5.10. Physical aging effects on the polymeric films were visible during the first heating scans: EVA-30 and EVA-65 showed similarities for both secondary and primary crystallization domains. The corresponding melting peaks were set at 46 and 60°C, respectively, with a CIR of 1.5 (EVA-65) and 1.4 (EVA-30). The appearance of a third melting peak at 86°C was attributed to the formation of smaller and more perfect ethylene crystals. The EVA samples exposed to temperatures close to the melting region (e.g. 60°C), could melt and recrystallize [85, 145, 146]. EVA-100 did not show any secondary or primary endothermic peaks in the typical 45 to 65°C interval. The cooling curves show that crystallization peaks are all shifted to higher values with respect to unaged conditions, from the initial 40°C to 48°C for EVA-30, 45°C for EVA-65, and a smaller exothermic peak at 70°C for EVA-100. This was attributed to chain scission due to the UV load combined with high humidity levels [85]. In the second heating thermograph, EVA-30 and EVA-65 showed again one single melting peak at 65 and 64°C, respectively. The comparison with the unaged sample confirmed the better stability of these two samples during UV aging with respect to the EVA-100. No peaks were detectable for EVA-100, indicating a generalized physical and chemical degradation of the polymer and loss of long-range crystal order.



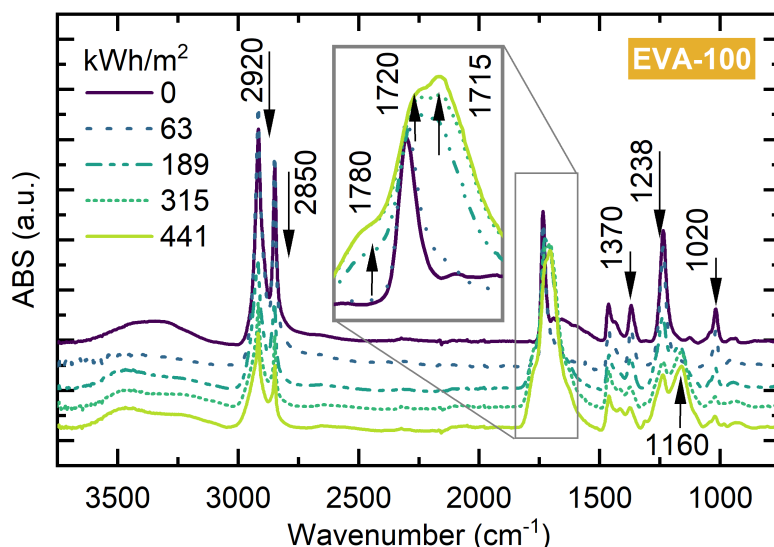


Figure 5.9: FTIR-ATR absorption spectra performed on G/ETFE/EVA/G EVA-100 coupons during UV exposure (up to a UV dose of 441 kWh/m<sup>2</sup>). Arrows refer to the intensity increase (arrows pointing up) and decrease (arrows pointing down) of the different peaks during UV aging. The zoom in highlights the increase in intensity of the bands at 1715 and 1720 cm<sup>-1</sup> attributed to ketones formation and at 1780 cm<sup>-1</sup> assigned to gamma-lactones.

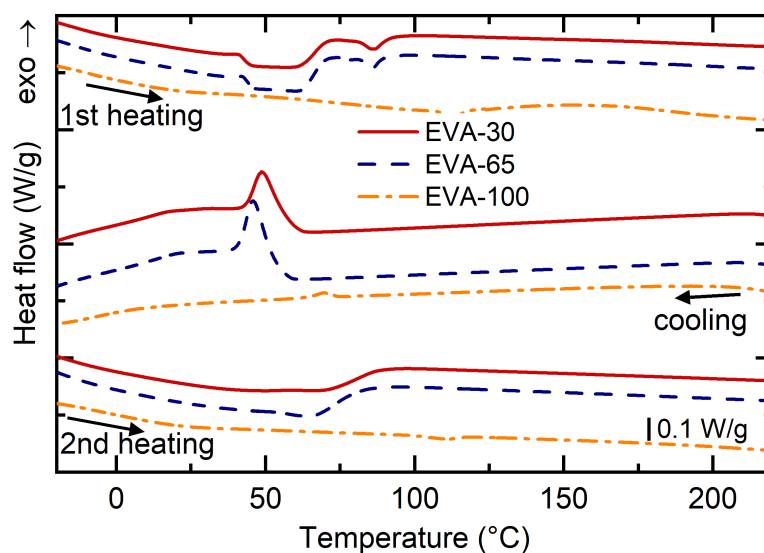


Figure 5.10: DSC thermographs performed on the G/ETFE/EVA/G coupons with EVAs stored at different conditions (EVA-30, EVA-65, and EVA-100) during UV aging, after a UV dose of 278 kWh/m<sup>2</sup>.

## 5.4 Summary and discussion

The storage condition of an uncured EVA roll can affect the long-term performance of a G-G module by accelerating degradation of the encapsulant. A priori, directly after the lamination process, no major notable differences could be observed between the modules encapsulated with optimally or poorly stored EVA. Only some minor physical defects (such as bubble generated along the edges of the modules) were detected by visual inspection.

More in-depth material analysis revealed that moisture from poorly stored EVAs was not entirely outgassed during the lamination process and that residual acidic species were present. Additionally, DSC showed that both poorly stored EVAs had a comparable crystal morphology, namely, forming a less stable crystal structure after the curing step. Nevertheless, this had no direct impact on the as-laminated performance of modules.

During the exposure of the samples to UV, different aging behaviors were observed. The optimally stored EVA (EVA-30) and first poorly stored EVA (EVA-65) showed no signs of degradation during the whole duration of the experiment. This result was well in accordance with the changes in the crystal morphology observed by DSC: exposure to temperatures close to the melting region of EVA-65 favored a rearrangement of the crystal morphology of this sample to resemble the properties of the more stable EVA-30 encapsulant. During the recrystallization process, the residual moisture had been partially outgassed, and this result was attributed to the aging temperature and not to the UV exposure.

Moreover, we emphasize the fact that the performance of the single-cell modules laminated with these polymers (EVA-30 and EVA-65) was very stable up to a cumulative UV dose of 630 kWh/m<sup>2</sup>, which is approximately equivalent to 10 years of outdoor exposure in a mid-latitude country. Therefore, this UV dose is sufficient to understand the early- to mid-life effects of residual trapped water on module degradation.

To reach this cumulative UV dose took more than one year of testing. Therefore, to understand how the modules' potential wear-out mechanism – after 25-30 years of field operation, particularly in a hot and humid environment - may look like, we have decided to use the extreme storage condition of EVA-100 in which the roll was soaked in water.

For these samples, the visual inspection of the modules encapsulated with EVA-100 showed that UV exposure resulted in fast degradation of the polymer. New bubbles were generated in the center of the module, and considerable shrinkage occurred along the edges of the module. A constant reduction in the current  $I_{sc}$  of the modules (and consequently of the power  $P_{max}$ ) was correlated to the increasing yellowing of the encapsulant, starting from a cumulative UV dose of about 189 kWh/m<sup>2</sup>.

The chemical degradation of the polymer observed by FTIR (Figure 5.9) was assigned to the VA moieties chain breaking and the generation of ketones and lactones by-products. It also showed severe degradation of the ethylene main chain. Finally, the EVA encapsulant eventually



became rigid and brittle due to these multiple chemical and structural changes. Therefore, the results observed for the EVA-100 mini-modules tell us that the combination of UV radiation and moisture can already considerably affect module performance on this time scale. However, in geographical zones where the humidity levels are not so high during the year, these results tend to suggest that EVA can still be a viable solution to encapsulate double-glass PV modules if good polymer storage and handling practices are carefully respected.

On the contrary, if these conditions are not respected, or in the event of module operation in a hot and humid climate, we believe that this may impact the long-term performance of glass/glass c-Si modules encapsulated with EVA. Understandably, in the first case, sign of polymer degradation would be evenly spread throughout the module. In the latter case polymer degradation would start from the edges and slowly propagate to the center, leading to an inhomogeneous degradation pattern.

We run some mathematical simulations to model the water ingress inside a G-G module encapsulated with a standard EVA for a total exposure of 20 years in two different climates, such as hot and humid (i.e. in Mumbai) and hot and dry (i.e. in Sharurah). The detailed information and procedures regarding the methodology to obtain the diffusion properties of the EVA the modeling and can be found in Appendix A and G. Results of the simulations are shown in Figure 5.11. For each climatic region, three different points inside the module were evaluated as depicted in Figure 5.11a, specifically, at the edge of the module, in the center of the first cell (C1), i.e. at a distance of 20 cm from the external edge of the module, and in the center of the second cell (C2), i.e. at a distance of 36 cm from the external edge of the module. By comparing Figure 5.11b and c, we can observe that in the case of an installation in a tropical climate, the edge of the module shows a "sinusoidal" shape reflecting the seasonality difference in humidity. However, water concentration under the first cell (i.e. C1 line in Figure 5.11b) is not negligible, and some water can yet reach the inner cell (i.e. C2 line in Figure 5.11c). Lower moisture values are reported when using the meteorological data of a hot and dry climate as reported in Figure 5.11c. The water concentration never reaches the saturation value, and the concentration at the edges stays always lower the half of the value compared to the tropical climate.

### 5.5 Conclusions

This chapter investigated the potential and criticalities of using EVA as an encapsulant material to manufacture glass-glass solar PV modules. The generation of acetic acid as a by-product of EVA photodegradation combined with a non-permeable glass-glass architecture may create a barrier to the adoption of this polymer for glass-glass modules. In particular, we simulated the effect of pre-absorbed water by the uncured EVA roll due to an uncontrolled storage environment or daily/seasonal variations in relative humidity that may be experienced in a non-optimally controlled manufacturing environment. Then we simulated a UV outdoor exposure of approximately 10 years, which is sufficient to understand the early- to mid-life

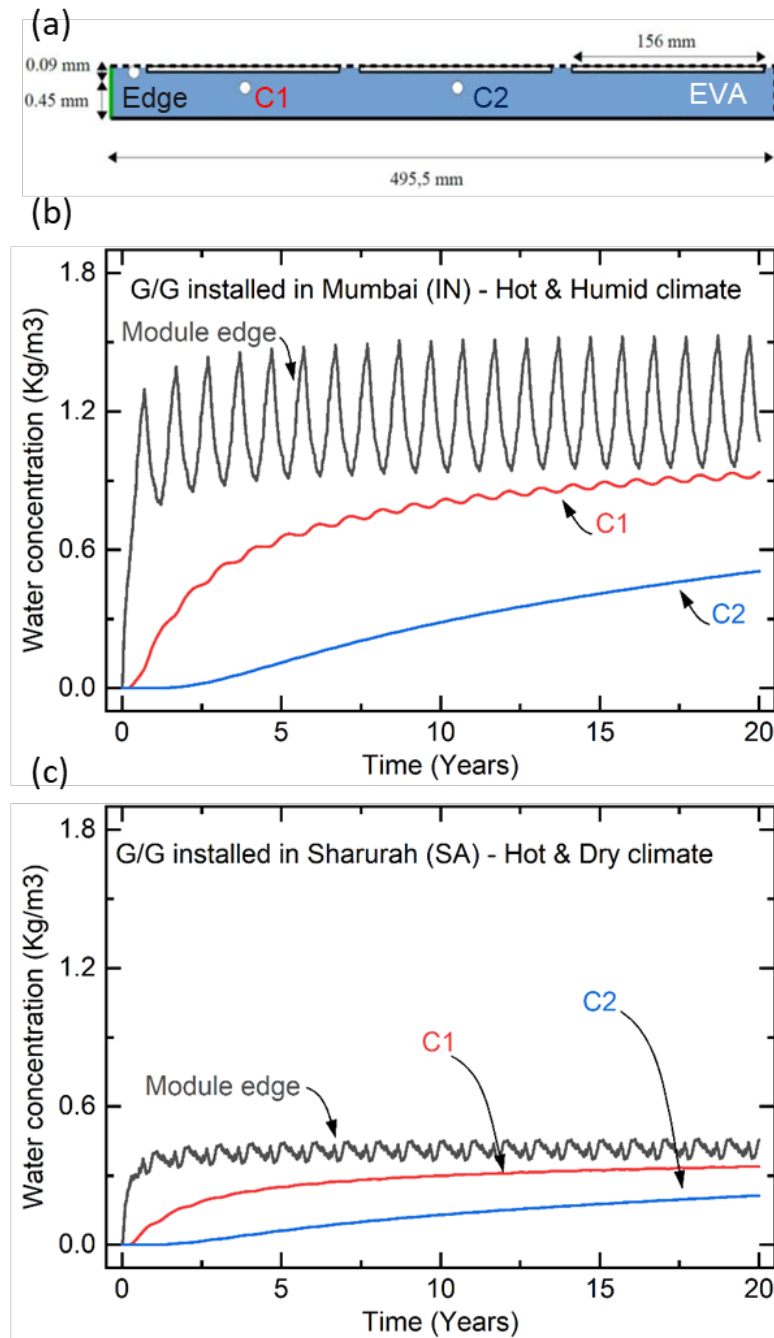


Figure 5.11: Modeling of water concentration of a 60-cells G-G module encapsulated with an EVA. (a) representative scheme of the module section with the 3 points at which the water concentration has been evaluated: module edge, in the middle of the first cell (C1), and in the middle of the second cell (C2). Models simulate the water concentration during 20 years of exposure in a hot and humid climate as in Mumbai (b), and hot and dry climate as Sharurah (c).

effects of residual trapped water on module degradation.

Based on our observations, we leave a door open to the adoption of high-quality EVA polymers in the manufacturing of glass-glass modules. However, the storage and handling conditions prescribed by the supplier should be carefully respected. In addition, good manufacturing practices should include:

- When uncured polymer rolls cannot be stored in a controlled environment, it is recommendable to cut only the needed quantity of material and to restore the remaining roll back in the original wrapping – under controlled environmental conditions - to reduce the exposure of the polymer surface to the air.
- When this condition cannot be satisfied, another possibility is to make some modifications to the lamination process steps: (1) increasing the initial pre-heating degas step time or (2) extending the cooling step after lamination and leaving modules at a temperature of about 65°C for 10-15 minutes. These adjustments prolong the lamination time, however, can allow potentially trapped water to degas out the module, and the encapsulant can rearrange the crystal morphology to a more stable form.

This work showed that the EVA formulation had been improved to resist against UV radiation. However, the presence of trapped water inside the module can trigger the degradation of the polymer with the consequent degradation and generation of by products such as acidic species. One major concern on the long-term durability is the stability of the metallization. The corrosion of metallic ribbons and screen-printed fingers due to EVA degradation can lead to the failure of the PV module. However, the effect of the corrosion can not be easily studied or reproduced using standard aging tests on a reasonable time scale. In the next chapter, we will show the results related to the quantitative measurements of the generated acetic acid upon delamination, and we propose a relatively fast methodology to test the stability of the interconnections against corrosion.

## 6 Corrosion testing of solar cells: Wear-out degradation behavior

### Summary

Corrosion is one of the main end-of-life degradation and failure modes in photovoltaic (PV) modules. However, it is a gradual process and can take many years to become a major risk factor because of the slow accumulation of water and acetic acid (from encapsulant ethylene vinyl acetate (EVA) degradation). In this work, an accelerated aging test for acetic acid corrosion was developed to probe wear-out and end-of-life behavior and facilitate screening of new cell, metallization, and interconnection technologies. In the tests, the top glass and EVA layers were removed from PV modules to expose the solar cells and interconnects. These “opened” modules were then placed in acid baths under varying conditions, including acid concentration, temperature, and electrical bias. Three cell technologies were tested, including Al-back surface field (BSF), passivated emitter and rear contact (PERC), and silicon heterojunction (SHJ). For all conditions, the presence of acid accelerated module power loss compared to control tests with water. Increased temperature accelerated the rate of degradation by several times. Application of electrical bias led to an initial drop in short-circuit current, but these modules eventually outperformed the non-biased modules. In all tests, lead oxides were the primary degradation products detected, and found to accumulate mostly along the printed metallization, especially in proximity to the busbar. SHJ cells with a silver paste-based interconnection outperformed Al-BSF and PERC cells with a solder-based interconnection. The accelerated corrosion test methods can be optimized to match corrosion behavior observed in field modules with greater precision and shorter times than standard damp heat tests, and can be applied to a variety of corrosion sensitive PV materials and components to assess their long-term durability.

### 6.1 Introduction

The lifetime of a photovoltaic (PV) module is influenced by a variety of degradation and failure phenomena. While there are several performance and accelerated aging tests to assess

design quality and early- or mid-life failure modes, there are few to probe the mechanisms and impacts of end-of-life degradation modes such as corrosion. The damp heat test is the main accelerated test for corrosion in PV modules [40, 147, 148]. However, the conditions are very aggressive – 85°C and 85% relative humidity – and may overstress modules, inducing degradation that is not observed in field operation [149]. Moreover, the test only includes water as a chemical stressor, even though it is known that acetic acid is present in field modules in concentrations up to at least 0.13% v/v (volume/volume) after several years [149, 150]. Therefore a more accurate test for corrosion in PV modules should include acetic acid as a stressor and be performed at lower temperatures [147, 148].

Acetic acid in modules is generated by the degradation of ethylene vinyl acetate (EVA) encapsulants, and it can take several years to accumulate to appreciable levels [149, 151]. This is because the degradation of EVA is an autocatalytic process, and the rates of generation and accumulation of degradation products such as acetic acid are not linear with time. At first it will increase slowly, and then rapidly, with the module performance decreasing correspondingly [86, 147, 148]. In the damp heat test it can take 3000 hours or more for appreciable amounts of acetic acid to accumulate [152–154]. Highly accelerated tests may achieve degradation faster, but extrapolation of test results to field performance remains a challenge [155, 156]. Kyranaki *et al* and Tanahashi *et al* [147, 148] have developed acetic acid-based corrosion tests for solar cells that are much shorter in duration, the former by bath immersion and the latter by vapor exposure. They both observe mostly current and fill factor losses, but propose two different mechanisms, either solder or finger corrosion. Additionally, the variety of test variables means that methods must be optimized to produce meaningful results, ideally to match corrosion behavior observed in field modules (e.g. as in [157, 158]).

In this work, an accelerated corrosion test method was developed based on the immersion of modules into acetic acid baths. Single cell modules had the top glass/EVA removed after lamination so that only the front-side of the cells were exposed. Three test conditions were varied, including acetic acid concentration, temperature, and electrical bias. Tests were performed on modules with three different cell technologies, including aluminum-back surface field (Al-BSF), passivate emitter and rear contact (PERC), and silicon heterojunction (SHJ). The test to failure methodology developed in this work can be used on a variety of cell, metallization, and interconnection technologies to assess and compare their corrosion susceptibility, especially their end-of-life behavior. Ultimately, this would feed into more robust and reliable design of these materials and technologies by greatly reducing test time with respect to outdoor monitoring or damp heat testing.

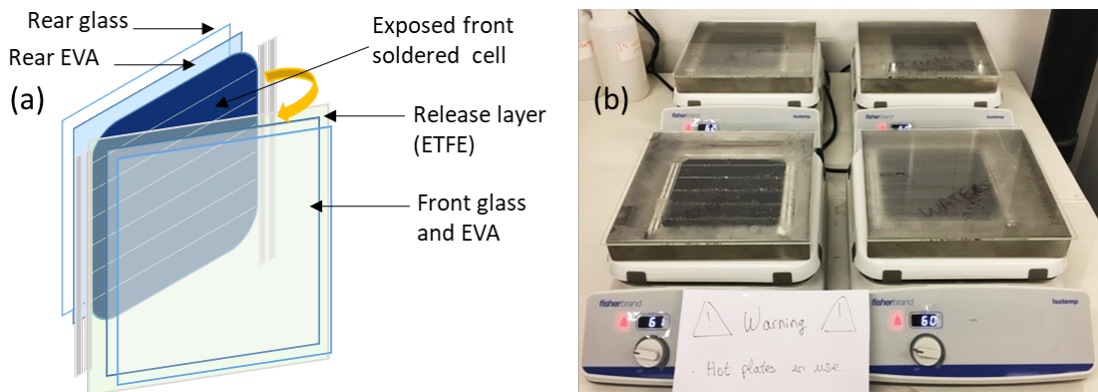


Figure 6.1: (a) Schematic of half-laminated module construction: after the lamination process the top layers (i.e. the front glass cover, front EVA, and ETFE release layer) were removed to expose the front surface of the cell. (b) Photograph of the accelerated corrosion test setup for high temperature and electrical bias.

## 6.2 Experimental methods

### 6.2.1 Module fabrication

Single cell monocrystalline silicon modules with Al-BSF, PERC, or SHJ solar cells were prepared with a half-laminated or “open” structure as illustrated in Figure 6.1a. The laminate structure included glass front and back covers and an ethylene vinyl acetate (EVA) encapsulant. An ethylene tetrafluoroethylene (ETFE) release layer was placed between the solar cell and top layer EVA so that it formed a weakly adhered interface [159]. After lamination, the top layer glass/EVA/ETFE was pried off the module, resulting in a half-laminated construction that leaves the cell, metallization, and interconnects exposed for the corrosion tests. This structure isolated the bottom of the cell so the acid baths only affected the front of the cells. The structure also ensured the cells were flat and able to be handled without breakage during the tests. The solar cell top metallization was based on screen printed silver with five (Al-BSF and PERC) or four (SHJ) busbars, and cell interconnects were 1.5 mm wide flat copper wires coated with a lead-tin based solder. For Al-BSF and PERC cells these were soldered onto the busbars, and for SHJ cells they were attached using a silver-based electrically conductive adhesive (ECA).

### 6.2.2 Corrosion testing

Modules were immersed in acetic acid baths using the conditions shown in Table 6.1. The three test variables included acid concentration (0% to 10% v/v), temperature (20°C or 60°C), and cell electrical bias (0 A or 8.5 A). These stress levels were selected to mimic or intensify field conditions. Pure (i.e. deionized) and mineral (i.e. ionized) water were used as control conditions. As for acetic acid, field modules have been measured containing up to 0.13% v/v

## Chapter 6. Corrosion testing of solar cells: Wear-out degradation behavior

Table 6.1: Accelerated corrosion test variables and levels. Not all combinations of levels were tested.

Acid conc. [% v/v]	Temperature [°C]	Electrical bias [A]	Cell technology
0 (pure or mineral)	20	0	Al-BFS
0.1	30	65	PERC
1	-	-	SHJ
5	-	-	-
10	-	-	-

acid [149, 150], and in this work higher concentrations were also used to accelerate corrosion processes. For simplification, in the rest of this work acid concentrations are referred to as percentages, instead of % v/v. For temperature, 60°C is a typical field module operating temperature in temperate climates [160]. Finally, for electrical bias, 8.5 A corresponds approximately to the max power point current of the solar cells under AM1.5 illumination.

The baths and modules were placed inside of stainless steel trays and covered during the tests to minimize evaporation of the acid solutions. For the elevated temperatures, hot plates were used to heat the solutions. For biasing, the modules were connected to a power supply as seen in Figure 6.1b and left in the dark. During the development of the test methodology not all possible combinations of conditions were explored.

### 6.2.3 Module and material characterization

Periodically during the corrosion tests the modules were removed from their solutions, rinsed, and dried before being characterized. Modules were visually inspected, and then light current-voltage (I-V) characteristics were measured under AM1.5 conditions. The main optoelectronic properties that were monitored included the power at maximum power point (PMPP), short-circuit current ( $I_{sc}$ ), open-circuit voltage ( $V_{oc}$ ), and fill factor (FF). Electroluminescence was measured with the modules around 8.5 to 9.0 A bias, the maximum power point current of the cells before the corrosion tests. After these tests, the modules were reintroduced to their acid baths. Corrosion tests were carried out for up to 600 hours of total exposure (n.b. compared to >3000 hours for noticeable corrosion effects in damp heat testing) [147, 153].

For some tests, small specimens up to 2 x 2 cm<sup>2</sup> were cut for optical and scanning electron microscopy (SEM) to examine changes to cell and metallization microstructure. Identification of degradation product composition and phase was done by energy dispersive x-ray spectroscopy (EDX) at 15 kV acceleration voltage and Raman spectroscopy with 514 nm excitation.

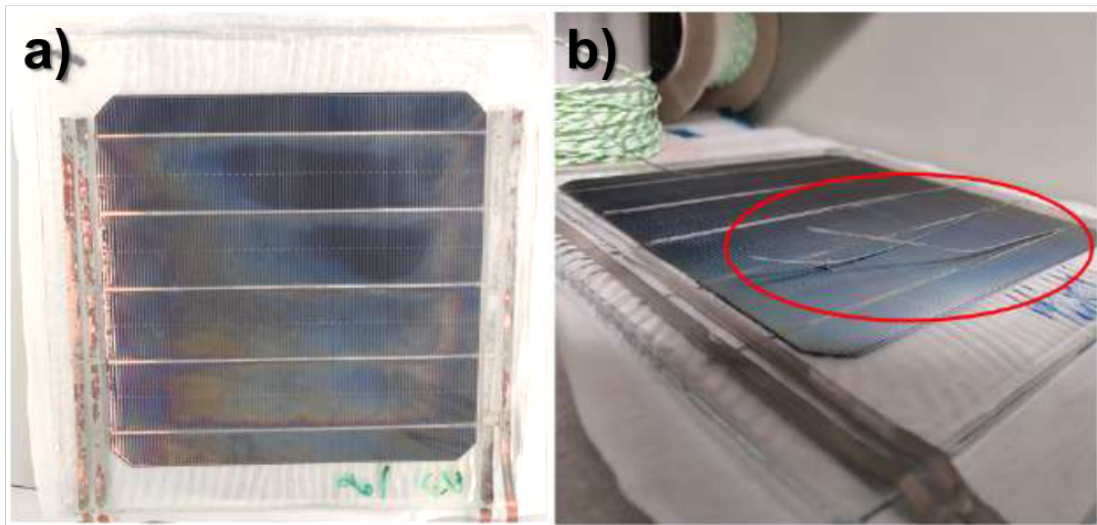


Figure 6.2: Visual inspection of Al-BSF modules during the corrosion tests, showing discoloration (a) and detachment of cell interconnect ribbons (b).

## 6.3 Results and discussion

Most of the tests in this work utilized Al-BSF cells. Many advanced solar cell technologies (e.g. PERC) utilize similar front metallization and interconnect materials, based on printed silver pastes and soldered interconnects. Thus, Al-BSF cells were used to establish a baseline for developing the test methods. Some tests were performed on PERC and SHJ solar cells, specifically, unbiased at 60°C with water, 0.1%, and 1% acid.

### 6.3.1 Al-BSF modules

#### Visual inspection

The visual aspect of the modules underwent significant change over the course of the tests. Most notable was a discoloration of the acid exposed modules (Figure 6.2a). This likely came from accumulation on the surface of corrosion products, such as lead oxides, which can be yellow, brown, or red in color depending on their oxidation state and layer thickness. In the high acid concentration tests (>1%) ribbon detachment was fairly common (Figure 6.2b), a behavior also observed in [147]. This detachment failure tended to occur before significant degradation was observed (i.e. >5% change in optoelectronic properties), so the remainder of the corrosion tests used water, 0.1%, or 1% acid. After extended exposure the solder on the cell and string interconnect ribbons began corroding away, even leaving the copper core exposed. Thus by visual inspection it appeared that the solder joint to the busbar was the cell component most likely to fail, a finding consistent with the lower oxidation potentials of lead-tin solder compared to copper and silver [161].



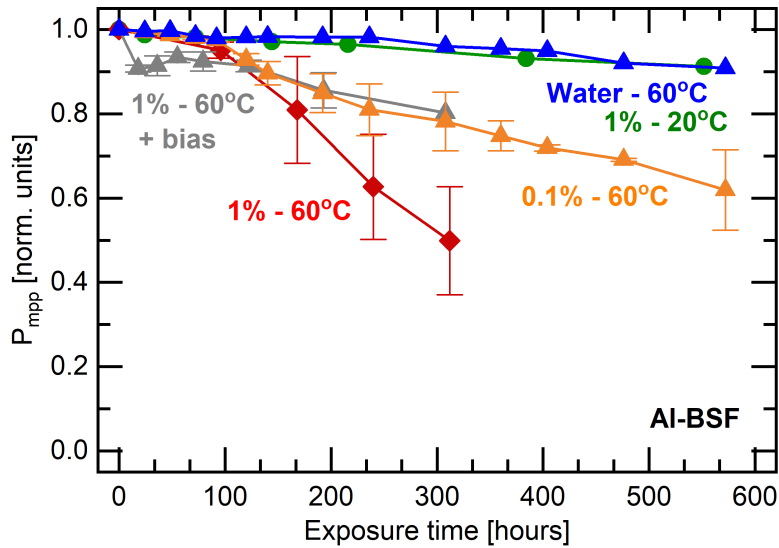


Figure 6.3: Normalized maximum cell power as a function of exposure time for water and acid (0.1% and 1%) exposed Al-BSF cells at 20°C and 60°C, with and without electrical bias.

### Electrical performance

Figure 6.3 shows the evolution of normalized maximum power (PMPP) over time for some of the Al-BSF module tests, including water and acid (0.1% and 1%). Other cell parameters (FF,  $I_{sc}$ ,  $V_{oc}$ ) are not shown. Max cell power was the main value that changed, caused mostly by reductions in the fill factor (FF). Short-circuit current ( $I_{sc}$ ) generally did not change significantly. Open-circuit voltage ( $V_{oc}$ ) was relatively stable for all tests, not decreasing more than 3% of their initial values.

As for the effect of acid concentration, in all tests, the presence of acid accelerated module degradation compared to the water tests. In fact, power loss was less than 10% for water tests in any test conditions, even up to 600 hours of exposure. Moreover, the type of water, pure or mineral, resulted in no differences in performance. The initial rate of power loss was similar for acid concentrations from 1% to 10% (not shown), indicating that acetic acid was not a rate-limiting reactant for these accelerated conditions. In 0.1% acid the rates were slower, reaching 60% initial power in more than twice the time as 1% acid modules ( $\approx 600$  hours vs.  $\approx 250$  hours respectively). Ribbon detachment eventually occurred in all tests with acid concentration above 1%. When detachment occurred, cell power would drop by tens of percent, and even to zero in the most severe cases, similar to behavior in [147]. Because of this, it was not possible to decouple gradual corrosion effects with this sudden detachment. Considering this ribbon detachment, further optimization of the test method focused acid concentrations  $\leq 1\%$ .

As for the effect of bath temperature, increasing temperature (60°C versus 20°C) resulted in a much faster rate of power loss. After 300 hours modules in the low temperature tests had undergone about 4% power loss, compared to nearly 50% for modules in the high temperature

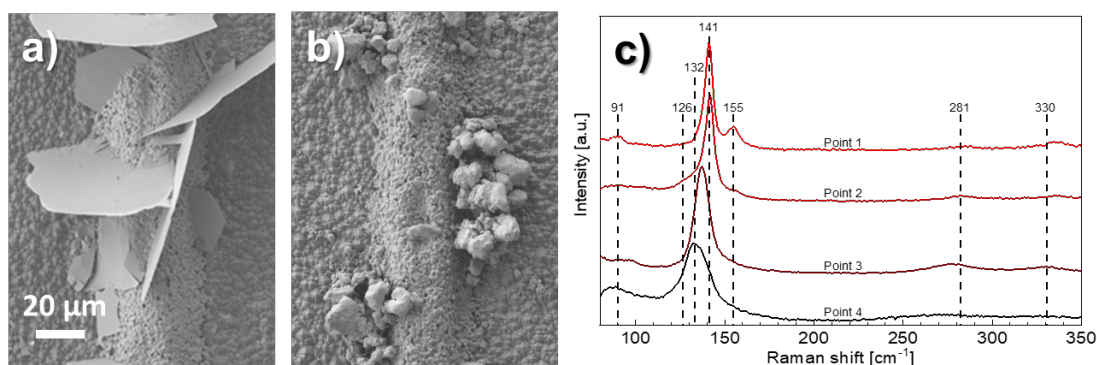


Figure 6.4: SEM along the finger of solar cells exposed at 20°C in water (a) and 1% acid (b), and Raman spectra of corrosion products in acid exposed cells indicating the presence of lead oxides (c).

tests. Even up to nearly 600 hours the modules at low temperature had only lost 9% of their initial power. Because corrosion is a chemical process it is thermally activated, thus corrosion rates would be accelerated during the daytime when modules are warmest.

As for the effect of electrical bias, the application of bias to the cells resulted in a rapid reduction in short-circuit current (about 8%) in the first few hours of exposure. After this, current remained stable, and fill factor losses became the main contributor to power loss. These modules outperformed the unbiased modules up to 300 hours, with power loss of only 20%, compared to 50%. Because corrosion is an electrochemical process, it was expected that an electrical bias would alter the mechanism and rate of power loss. Electroplating of copper was observed on the biased cells, and this process may have contributed to the improved performance over the unbiased cells.

### Material-level characterization

SEM was used to examine the cell microstructure during the tests. The most notable feature included accumulation and growth of microstructures along the printed metallization, a feature also observed in field modules [158, 161]. In water these had a flake-like morphology (Figure 6.4a), while in acid they exhibited a fine, cluster-like morphology (Figure 6.4b). EDX showed these features to be rich in lead and oxygen and their Raman spectra (Figure 6.4c) showed characteristic peaks of  $\text{PbO}_2$ , most notably in the region from 120 to 160  $\text{cm}^{-1}$  [162]. Peak shape and position sometimes varied by point, which may be a laser-induced heating effect of the structures with low crystal quality, similar to behavior observed in [162]. Metal acetates and other oxides were not detected at any points.

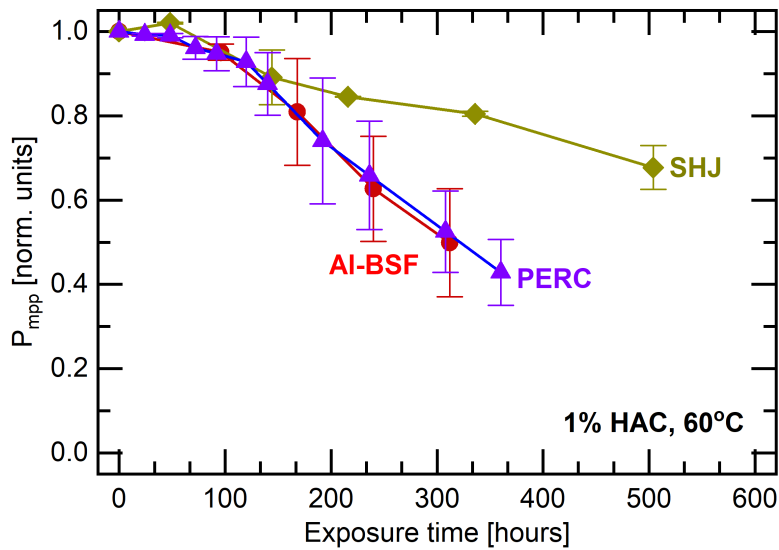


Figure 6.5: Normalized maximum cell power as a function of exposure time for three cell technologies (Al-BSF, PERC, and SHJ) in 1% acid at 60°C without electrical bias.

### 6.3.2 PERC and SHJ modules

PERC cells have rapidly become the dominant technology in the PV market. The front structure and metallization are similar to Al-BSF cells, with silver based metallization and soldered interconnects. The back structure is different, with a passivated rear contact (with  $\text{Al}_2\text{O}_3$  or  $\text{SiN}_x$  layers), but because of the half-laminated construction of the modules it is not exposed in these corrosion tests.

SHJ solar cells are a high efficiency technology based on crystalline silicon coated on both sides with amorphous silicon layers. This passivates the cell surface, giving rise to higher cell voltages than for Al-BSF or PERC cells. Typically cell interconnect ribbons are attached with an ECA instead of solder, because the thin amorphous silicon layers are sensitive to high process temperatures. For PERC and SHJ the visual appearance during testing was similar to the Al-BSF modules (Figure 6.5), with discoloration of the acid exposed modules. Normalized power versus test time for Al-BSF, PERC, and SHJ modules is shown in Figure 6.5 in 1% acid. In water no significant corrosion was observed for any cell type (not shown). The behavior between Al-BSF and PERC is very similar throughout the tests, as may be expected because of their similar front structure. Thus despite improvements in device structure for PERC to increase efficiency, they still remain susceptible to the corrosion phenomena that occur in Al-BSF technologies. As for SHJ, the initial rate of power loss is similar up to 150 hours (about 10%), but after this the Al-BSF and PERC cells degraded much more quickly. After 300 hours the Al-BSF and PERC cells had lost 50% of their initial power, compared to only 20% for the SHJ cells. The cell interconnect ribbons are attached by a silver-based ECA, which is clearly more resistant to acid-induced corrosion than the lead-tin solder. This is also evident from the limited corrosion observed along silver fingers for all types of cells.

## 6.4 Applications to module development

Conventional tests for corrosion in PV modules, specifically the damp heat test, do not accurately reproduce field behavior [158, 161]. This is because 1) the test conditions are not correlated to any realistic module operating conditions (extreme humidity), and 2) acetic acid is absent as a chemical stressor, except in extended testing. On these points the accelerated acid corrosion test developed in this work is aimed at more reliable assessment vis-à-vis long-term field performance of EVA encapsulated modules by probing this wear-out degradation mechanism. Moreover, the tests are much shorter, requiring up to a few hundred hours to achieve the same level of power loss seen in >3000 hours (>125 days) of damp heat testing [147, 153].

EVA remains the encapsulant of choice for most PV module manufacturers, in spite of the known challenges of environmental degradation, including acetic acid generation [30, 109]. Additionally, the variety of solar cell, metallization, and interconnection technologies in the market is evolving and expanding very rapidly [30, 163]. From the material side, there are major pushes towards reduced silver content and lead-free solders. On the process side, there are continuous modifications to screen printing and soldering processes, and increased use of alternatives such as electroplating. Finally, in terms of cell design, there are an increasing number of busbars, while cutting, shingling, and back contacting of solar cells are also growing. While two busbars were standard up to ten years ago, it is now common to see 9+ busbars per cell. These then have a much smaller connection area with a higher surface to volume ratio, potentially making them more susceptible to corrosion.

Thus, there are ample concerns about acetic acid corrosion in the foreseeable future that warrant improved testing, even if alternative encapsulants that do not generate acetic acid are slowly entering the market [30]. The accelerated corrosion test in this work requires the use of a release layer to expose the cells, and is well suited to material and component (mini-module) testing to optimize materials and processes for improved corrosion resistance. Based on this work, two test conditions can be proposed. The first, to mimic expected field conditions, should be performed at 60°C in 0.1% acid. The second allows moderate acceleration (at least two times the first condition), and should be performed at 60°C in 1% acid. In these conditions comparative analyses can be made between test specimens in a time frame of some days or a few weeks. Further improvements to this test method could include extraction of temperature dependencies (Arrhenius) for modelling purposes, and better understanding of the improved performance seen in biased solar cells.

## 6.5 Conclusions

Most module manufacturers will continue to use acid generating EVA encapsulants in the near- to mid-term. Moreover, there is a rapidly expanding variety of materials, processes, and designs in solar cell, metallization, and interconnection technologies. Thus, an accelerated

acid corrosion test to probe wear-out degradation behavior has great relevance to module development. In that regard, in this work an accelerated corrosion test method was developed with major improvements on damp heat testing. In a few hundred hours it achieves the same level of power degradation that takes >3000 hours in a damp heat test. The tests to failure included immersion of half-laminated solar cells (front-side exposed) in acetic acid baths of varying concentration, temperature, and cell bias. High acid concentrations (>1%), resulted in rapid degradation due to ribbon detachment. Higher temperatures accelerated module power loss by several times, mostly by fill factor reduction, and features matched those seen in field modules with corrosion-related degradation. The application of electrical bias initially led to a drop in current, but eventually these cells outperformed non-biased cells. Finally, SHJ cells were more resistant to corrosion effects than Al-BSF and PERC cells, a behavior likely related to the use of a silver-based ECA for cell interconnection. An optimized test can be used to screen and improve design for a variety of solar cell, metallization, and interconnection technologies that are susceptible to corrosion.

## 7 Conclusions and perspectives

### 7.1 Summary

The adoption of crystalline silicon (c-Si) photovoltaic (PV) modules based on glass-glass (G-G) structures is still limited compared to the more conventional glass-foil structure. However, glass-glass modules are gaining momentum because of the possibility of manufacturing bifacial panels, collecting light from the rear side. Despite not being an optimal material, ethylene vinyl acetate (EVA) has become the dominant encapsulant material in the PV industry. Nevertheless, upon exposure to UV at high temperatures in the presence of moisture, EVA may photo-degrade, leading to the generation of acetic acid (HAc). HAc will lead to the corrosion of the metallic interconnects inside the module, generally impacting the durability of the modules. In glass-foil structures, HAc can be partially outgassed from the module laminate through the breathable back-sheet polymeric foil. This helps mitigate (or delay) the degradation process. However, the presence of a rear cover glass in G-G modules does not allow the acid to be released from the module. For this reason, the industry is developing alternative polymers such as polyolefins (PO) in non-permeable glass-glass structures. Nevertheless, some manufacturers continue or would like to continue using EVA in manufacturing double glass laminates because of the lower cost, the much longer track record, and easier processability of EVA compared to the alternatives. In this work, we primarily focus on the long-term reliability of glass-glass module structures and try to answer the question of whether it is possible to use EVA in their manufacturing. To do this, we use a combination of multiple solar cell technologies (all wafer-based c-Si ones), different encapsulant materials, and edge seals.

In Chapter 3, we study **the sensitivity to water and moisture of different c-Si cell technologies exposed to damp heat**:

- The diffusion of water inside the EVA encapsulant (from the edges of the module) does not impact its optical and chemical properties. No noticeable signs of degradation are detected during the whole duration of the test (i.e. 2000 hours).
- The effect of the water on the module power output depends on the type of solar cell. In

particular, Al-BSF and PERC modules are reasonably stable in DH. However, we observe an instability of the metallic interconnects (BB and fingers) specific to the tested Al-BSF cells. The similar soldering process used for both BSFs and PERCs should be comparable under the same test conditions. This inconsistent result inspired us to develop a specific test to compare different interconnection technologies.

- We observe a strong degradation for the SHJ G-G modules encapsulated with EVA after 500 hours of exposure to DH. Both  $I_{sc}$  and  $V_{oc}$  are damaged. The degradation pattern follows the water diffusion inside the module.

In Chapter 4, we propose **a detailed microscopical model explaining the sensitivity of the SHJ technology to water:**

- The known instability concern regarding the encapsulation scheme of G-G SHJ modules using EVA is studied with great care to understand the specific degradation mechanism.
- In reality, the presence of water (favored by the use of EVA) is only a contributing factor, as clearly indicated by the fact that to trigger the degradation process, both water and the presence of glass are needed. Here we point at the role of a glass corrosion process and of  $\text{Na}^+$  and  $\text{OH}^-$  in damaging the properties of the cell's passivating layers.
- We are the first to propose a detailed microscopical model that attempts to explaining the root cause behind the observed degradation mechanism and the extreme sensitivity to water - and sodium - of SHJ cells/modules in the presence of EVA and glass.
- We provide valid mitigation strategies, such as (i) the use of an edge sealant to avoid/minimize water ingress or (ii) the use of an alternative encapsulant with a lower water vapor transmission rate, such as a poly-olefine formulation.

In Chapter 5, we study **the impact of EVA storage conditions on lamination quality and ultraviolet (UV) degradation:**

- We evaluate the combined effect of moisture and UV radiation on EVA degradation. Specifically, we simulated the effect of pre-absorbed water by the uncured EVA roll due to a non-optimally controlled manufacturing environment or the daily/seasonal outdoor variations.
- After the lamination process we observed only minor aesthetic defects in the modules encapsulated with a poorly stored EVA.
- After a UV outdoor exposure simulation of approximately 10 years in a central European temperate climate, the well stored EVA showed an excellent UV stability. No significant degradation of chemical or optical properties is detected.

## 7.2 General conclusion on the use of EVA in a glass-glass PV module

---

- On the contrary, the effect of a poorly stored EVA occurs upon UV exposure. A gradual module loss of the  $I_{sc}$  parameter is correlated to the degradation of the EVA, which causes the discoloration of the polymeric material.
- When the storage condition is not too harsh (i.e 65% RH), a thermal recovery of the EVA crystal morphology is possible after the lamination. We observe a rearrangement to a more stable conformation - comparable to the well stored EVA - if the module is kept at temperatures close to the melting temperature range of the EVA (i.e. 65-70 °C).
- If good polymer storage and handling practices are carefully respected, these results suggest that EVA can still be a viable solution to encapsulate double glass PV modules for deployment in geographical zones where the humidity levels are not so high during the year (i.e. temperate climates). On the contrary, if these conditions are not respected, or in the event of module operation in a hot and humid climate, we believe that this may impact the long-term performance of glass-glass c-Si modules encapsulated with EVA.

In Chapter 6, an **accelerated aging test for acetic acid corrosion** is developed:

- The rapid expansion of material varieties, processes and designs in solar cell metallization, and interconnection technologies call for a specific test method to evaluate the stability of different interconnects in presence of water and more specifically to probe wear-out degradation behaviors due to acid corrosion. An accelerated corrosion test method is developed with major improvements on damp heat testing. In a few hundred hours it achieves the same level of power degradation that takes >3000 hours in a DH test.
- We observed that high acid concentrations (>1%), resulted in rapid degradation due to ribbon detachment. Higher temperatures accelerated module power loss by several times, mostly by fill factor reduction, and features matched those seen in field modules with corrosion-related degradation.
- Among the tested cell and metallization schemes, SHJ cells were more resistant to corrosion effects than Al-BSF and PERC cells, a behavior likely related to the use of a silver-based ECA for cell interconnection.

## 7.2 General conclusion on the use of EVA in a glass-glass PV module

Based on our results, EVA can be a valid option for G-G modules, provided that optimal storage conditions of uncured rolls are followed. In addition, the use of an edge sealant is recommended to reduce water ingress. In fact, a dry EVA has proven to withstand prolonged UV exposure better and mitigate SHJ DH and potential induced degradation (PID), as recently reported by some colleagues at PV-Lab [164]. The possible use of EVA with SHJs is further encouraged by the remarkable stability of the ECA when referring to the long-term corrosion



wear-out. However, the glass-glass EVA encapsulation scheme for PERC cells might still be an issue for the PID effect as it will likely allow  $\text{Na}^+$  to go through the  $\text{SiN}_x$  layer, even in dry conditions [165].

This is a hot topic in the PV industry. We approached several companies during conferences and work-shops, which confirmed the urge to understand and address the EVA limitations, particularly in a G-G structure. Therefore our investigations are in agreement with the challenges that the PV market is currently facing. Our key findings could be helpful not only for the scientific community but also for the main industrial PV players.

### 7.3 Perspectives

#### Can G-G modules with SHJ cells be manufactured with EVA and an edge seal?

We observed excellent resistance of SHJ cells against both damp heat and potential-induced degradation if the EVA remains *dry*. In addition, the use of a high-quality EVA (i.e. optimally stored until its usage) allows to preserve its chemical and optical properties upon exposure to relatively high UV doses. Further, SHJ cells with a silver paste-based interconnection exhibited better stability to acetic acid corrosion than other cell types (i.e. Al-BSF and PERC). Therefore, the good electrical performances of this structure should be guaranteed even in the occurrence of the EVA photodegradation - with the consequent generation of acetic acid. However, we have observed a reduction of the  $I_{sc}$  when SHJs are exposed to UV (see Appendix E).

In view of an exhaustive answer to the initial question, more investigations are required to understand the causes of the UV-induced degradation of the SHJ cells and develop suitable solutions. From our preliminary results, the damage occurs at the early stage of the test, and it seems to stabilize at more prolonged UV exposure. Given that we have already verified the stability of the optical properties of the EVA, one hypothesis is that the current reduction is somewhat related to an incompatibility at the EVA/ITO interface. Hence, we should further extend the test duration and perform more specific analyses (i.e. SEM images) to verify our hypothesis. If the UV-induced degradation is mitigated, these module structures should be investigated to target the extended service lifetime of SHJ modules (i.e. 35+ years).

#### Update the microscopical model

The specific degradation mechanism of SHJs cells in the presence of moisture, EVA, and glass can be further implemented as follow:

- We have observed that the degradation occurs when the water content inside the EVA is at its quasi-saturation concentration. However, the reaction kinetics of the glass corrosion and the time needed to the dissolved  $\text{Na}^+$  ions to diffuse through the EVA thickness is unknown. The required water concentration in the EVA, the activation

energy of the process (i.e. its dependence on the temperature), and the diffusion rate need to be evaluated to estimate the potential occurrence of the problem during outdoor exposure. In particular, knowing that the leaching process of glass cannot occur under a certain moisture concentration will allow estimating the specific climatic zone in which an edge seal is recommended.

- In parallel, we can investigate other mitigation strategies, such as the improved barrier ability of the ITO. Different ITO morphologies (i.e. the crystallinity and the crystal's grain size) and other TCO formulations (such as aluminium-doped zinc oxide (AZO) or indium tungsten oxide (IWO)) should be tested with the *droplet* methodology to have a fast insight into their stability. In addition, the inner surface of the glass (i.e. the one in contact with the EVA) could be coated with a specific *Na-repelling layer*.

### **Development of more precise water measurements and more effective UV aging testing methodologies**

In Chapter 5 we investigated the importance of uncured EVA rolls' storage conditions and we distinguished three different scenarios. However, we could not quantify the concentration of residual water inside the module after the lamination process. In Appendix F, we showed the potential of using the Karl Fisher method to quantify water content inside the EVA accurately. This technique measures water inside the encapsulant under any condition. However, it is essential to develop a consistent and accurate design of experiment to reduce the uncertainty of the measurement (after the lamination, it is hard to get access to the encapsulant without the use of time-consuming operations that will modify/contaminate the sample).

To simulate an outdoor exposure in a temperate climate of ~10 years, corresponding to a cumulative UV dose of 630 kWh/m<sup>2</sup>, the aging test lasted more than one year. Therefore, the test duration should be extended to additional two years to investigate wear-out mechanisms occurring after 30 years in operation and confirm our hypothesis. In view of a more realistically applicable testing methodology, a more effective and faster UV-soaker source/chamber should be developed (i.e. an array of UV-LEDs with spatial uniformity, which well matches the sun spectrum).

### **Optimization of the corrosion testing procedure**

The accelerated acid corrosion test could be further improved by conducting tests at different temperatures to include extraction of temperature dependencies (i.e. Arrhenius) for modeling purposes. In addition, the *accelerator factor* observed by changing the acid concentration needs more investigations to find the optimal experimental conditions trade-off between the test duration and the trustworthiness of the results.



# A Evaluation of the diffusion properties of EVA

The first step to run mathematical simulation to evaluate the water ingress process inside a glass-glass module was to determine the needed material properties of the polymeric encapsulant (i.e. EVA).

The most used approach in the literature to characterize the diffusivity properties of the polymers used in PV (i.e. encapsulant and back-sheet) is measuring its water vapor transmission rate (WVTR) [166–168].

## Water vapor transmission rate measurements

The WVTR is defined as "*the flux of water through the material, i.e. the amount of water flowing per unit time through a unit area of the material surface*" [169]. Units for WVTR are typically  $[\text{g}/\text{m}^2/\text{day}]$ .

WVTR measurements were performed in two laboratories: at the Packaging Laboratory (LEC) of the University of Applied Sciences Western Switzerland (HEIG-VD) based in Yverdon-les-Bains (CH), using a Mocon Permatran twin 3/33, and at the Laboratory for Processing of Advanced Composites (LPAC) at EPFL, using a permeation analyzer (Systech Instrument 7001).

The measurement methodology for the 2 instruments is similar. The EVA sample, was set between two chambers. The relative humidity of the chambers was always maintained constant at 90% and 0%, respectively. This was done by flowing only nitrogen,  $N_2$  in the *dry chamber*, and a specific controlled mixture of  $N_2$  and water vapour in the *wet chamber*. Initially, during the test the sample started absorbing water from the wet chamber, while the water concentration on the dry side was kept null. The concentration gradient within the polymer film evolved (i.e. transient regime) and eventually reached a linear profile (i.e. stationary regime). The test was stopped after reaching the stable stationary regime.

The measured WVTR data was then fitted with the equation for the WVTR curve (obtained by solving Fick's first law of diffusion with Fourier series):

$$WVTR(t) = \frac{D \cdot c_{sat}}{L} \left( 1 + 2 \cdot \sum_{n=1}^{\infty} (-1)^n \exp\left(\frac{-D \cdot n^2 \cdot \pi^2 \cdot t}{L^2}\right) \right) \quad (A.1)$$

where  $t$  is time,  $D$  is the diffusion coefficient,  $c_{sat}$  is the polymer water saturation concentration, expressed in  $[g/m^3]$  and  $L$  is the thickness of the sample. Both  $D$  and  $c_{sat}$  depend on the measurement temperature.

An example of typical WVTR curve with the fitting line is displayed in Figure A.1 highlighting the two distinguished experimental regimes: an initial transient regime followed by a stationary one when the water concentration inside the polymer film reaches its saturation value.

The steady-state value of WVTR was calculated by taking the limit of Equation A.1 for  $t \rightarrow \infty$ :

$$WVTR(steady-state) = \lim_{t \rightarrow \infty} WVTR(t) = \frac{D \cdot c_{sat}}{L} \quad (A.2)$$

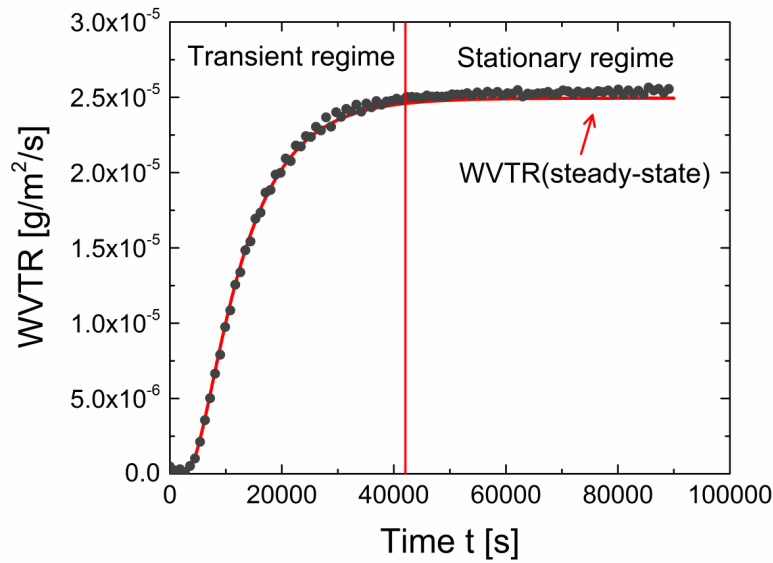


Figure A.1: Typical WVTR curve of a back-sheet as measured (black dots) and its fitting curve (red line) obtained with Equation A.1. After an initial increase (transient regime), the WVTR values eventually reach a steady-state value.

### Procedure for the diffusivity properties evaluation

With the purpose of simulating water diffusion at any environmental temperature, we measured for each material the WVTR at three different temperatures. The diffusivity properties of the encapsulant and its dependency with the temperature were then calculated for each temperature with the corresponding activation energy ( $E_a$ ) extrapolated with the Arrhenius-type

---

function.

The following described procedure, was previously set up by former PV-Lab colleagues, Valentin Chapuis, Federico Galliano and Eleonora Annigoni.

- By fitting the measured curve of the WVTR with Equation A.1, the diffusion coefficient  $D$  and the factor  $D \cdot c_{sat}$  are extracted. The latter is the value of the plateau of the curve, WVTR(steady-state).
- We used the following definition of permeability  $P$ :

$$P = D \cdot S, \left[ \frac{g}{m \cdot s \cdot mbar} \right] \quad (A.3)$$

where  $S$  is the solubility of the material.

By expressing the concentration of water at the surface of the polymer film in Equation A.1 with Henry's law we get:

$$c_{sat} = S \cdot p_{H_2O}, \left[ \frac{g}{m^3} \right] \quad (A.4)$$

where  $p_{H_2O}$  is the water vapor partial pressure. Inside the "wet" chamber the relative humidity (RH) is kept constant (i.e. RH=90%), thus by its definition we can write  $p_{H_2O}$  as:

$$p_{H_2O} = RH \cdot p_{H_2O}^{sat}, [mbar] \quad (A.5)$$

where  $p_{H_2O}^{sat}$ , the water saturation pressure is calculated with the Arden Buck equation:

$$p_{H_2O}^{sat}(T) = 6.1121 \cdot \exp \left( \left( 18.678 - \frac{T}{234.5} \right) \cdot \frac{T}{T + 257.14} \right) \quad (A.6)$$

We can now calculate the permeability as:

$$P = \frac{WVTR(steady-state) \cdot L}{RH \cdot p_{H_2O}^{sat}} \quad (A.7)$$

- The solubility  $S$  is computed from the permeability definition from Equation A.3.
- Finally, the saturation concentration is obtained from the fitted value of  $D \cdot c_{sat}$ .

## Results

Figure A.2 shows the experimental data and the corresponding fitted WVTR curves for the EVA film. The evaluated diffusivity properties for the 3 tested temperatures are resumed in Table A.1:

## Appendix A. Evaluation of the diffusion properties of EVA

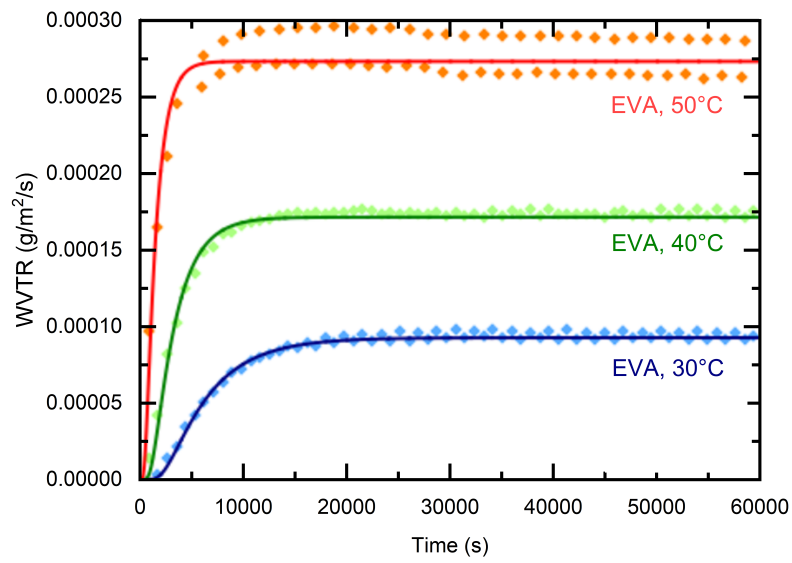


Figure A.2: WVTR experimental points and fitted curves for the tested EVA encapsulant at three different temperatures: 30, 40 and 50°C.

Table A.1: Diffusivity properties of EVA at three different temperature with the corresponding activation energies.

	<b>D [m<sup>2</sup>/s]</b>	<b>P [g/m/s/mbar]</b>	<b>S [g/m<sup>3</sup>/mbar]</b>	<b>WVTR [g/m<sup>2</sup>/s]</b>
30°C	5.739E-11	3.723E-9	64.87	9.177E-5
40°C	1.126E-10	3.988E-9	35.41	1.698E-4
50°C	2.379E-10	3.799E-9	15.97	2.707E-4
<b>E<sub>a</sub></b>	57.86 kJ/mol	0.88 kJ/mol	-56.98 kJ/mol	44.1 kJ/mol

## B Water ingress simulations during indoor DH test

The moisture ingress was modeled as a diffusion problem using the *Transport of Diluted Species interface* in Comsol Multiphysics (version 5.3). In steady conditions (i.e. constant temperature and relative humidity during time) other programs, such as Mathematica or MatLab can be used as well.

The following described procedure, was previously set up by former PV-Lab colleagues, Valentin Chapuis, Federico Galliano and Eleonora Annigoni.

For the purpose of this work (see Chapter 3), FEM simulations were employed to model the water ingress into a glass-glass 1 cell module exposed to the specific aging conditions of the Damp Heat test (i.e. 85°C and 85% RH). By knowing the diffusivity properties of the EVA and the related activation energies (evaluated as described in Appendix A), it was easy to calculate the needed values at 85°C by applying an Arrhenius plot. The extrapolated values, used for the simulation are reported in Table B.1.

The conditions we imposed for the FEM simulations are the following:

- Initial conditions: we assumed the EVA initially dry;
- Boundary conditions: we supposed that the external surfaces of the EVA and of the BS are in equilibrium with the environment. Therefore the water concentration at the boundaries (i.e the edges of the module) were calculated using the Arden Buck equation to calculate the water saturation pressure ( $p_{H_2O}^{sat}(85^{\circ}C)$ ), then we applied the Henry's law to calculate the water vapor partial pressure ( $p_{H_2O}(85^{\circ}C)$ ) at 85% of RH. Finally, the

Table B.1: Diffusion coefficient (D) and solubility coefficient (S) values for EVA at 85°C.

D (T=85°C) [ $m^2/s$ ]	S (T=85°C) [ $g/m^3/mbar$ ]
1.89E-9	2.09



## Appendix B. Water ingress simulations during indoor DH test

saturation concentration at the EVA external surface was evaluated:

$$c_{sat}(85^{\circ}C, 85\%RH) = S \cdot p_{H_2O} = 57.08 \text{ mol/m}^3.$$

The 2-dimensional (2-D) geometry drawn in Comsol, replicating a 1 cell glass-glass module sample is schematically represented in Figure B.1 along with the points (i.e. at the cell edge, and in the center of the cell) at which the water ingress model was computed. The simulations were replicated a DH test duration of 2000 hours with an evaluation frequency of 1 point every 3600 sec (i.e. 1 hour).

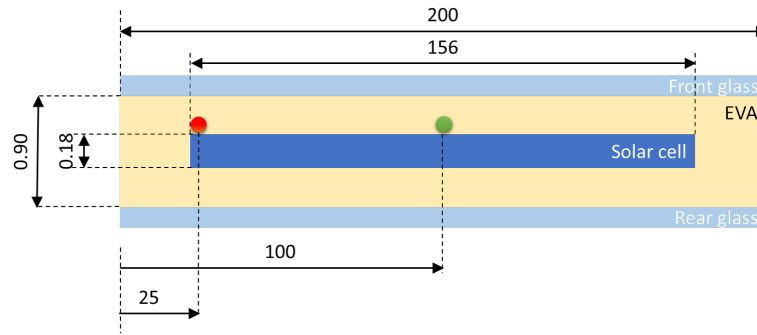


Figure B.1: Schematic representation of the cross-section of the geometry used for the 2D water ingress modeling during Damp Heat aging test. The chosen size replicates a 1 cell glass-glass module sample. The red and green dots represent the evaluated points (at the edge and in the center of the cell).

## C Effect of moisture on SHJ passivating cell layers and interface: i/p a-Si:H and i/pa-Si:H with ITO samples

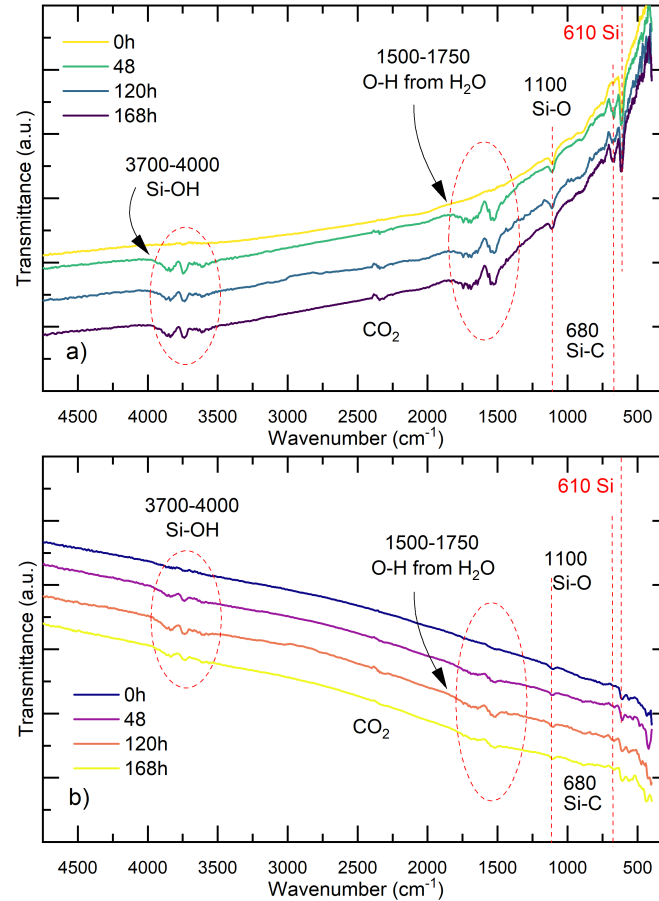


Figure C.1: FTIR spectra performed on untetxtured Si wafer coated with *i/p a-Si* layers (a) and *i/p a-Si* with ITO layers (b), before and during Damp Heat aging. Upon exposure to DH, the formation of -OH group from  $\text{H}_2$  and Si-OH are observed.



## D Effect of the $\text{NaCl}_{aq}$ on SHJ cells exposed to DH

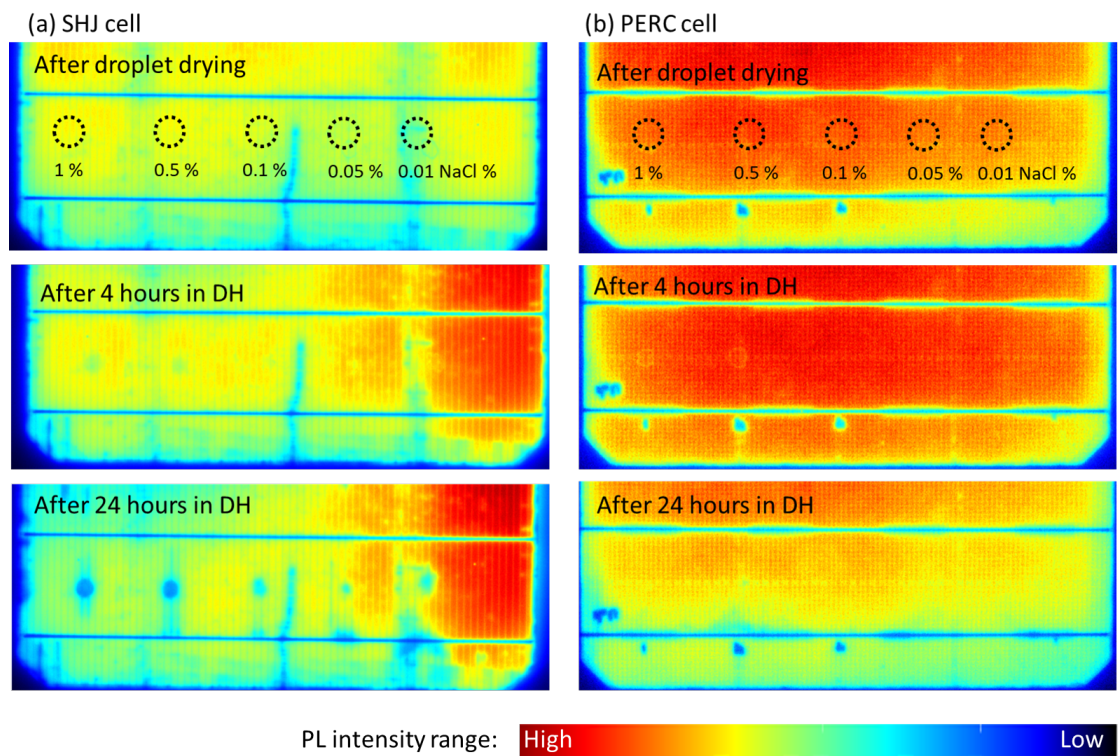


Figure D.1: NaCl aqueous solution droplet test. PL images of SHJ (a) and PERC (b) cells taken after the droplets drying with different NaCl concentrations (i.e. 1%, 0.5%, 0.1%, 0.05% and 0.01% w./w. ), and 4 and 24 hours of exposure in Damp Heat conditions.



## E Effect of the UV on Al-BSF, PERC, and SHJ G-G modules

A first indoor aging test was performed using the same encapsulation scheme reported in Chapter 3. We used the same set of 1-cell G-G modules including Al-BSF, PERC and SHJ cell types.

After the lamination process, modules were subjected to the method A-3 from the IEC 62788-7-2 standard [98]. The setting inside the climatic chambers along with the test duration are reported in Table E.1. The Xe-arc lamp with daylight filter has a UV dose corresponding to 63 W/m<sup>2</sup> (295 to 395 nm range).

The UV aging test was stop after 1000 hours, corresponding to a cumulative UV dose of 63 kWh/m<sup>2</sup>. This value corresponds to an outdoor exposure of approximately 1 year in a temperate climate in middle Europe country, such as Switzerland. However, some useful results could be observed.

The I-V curves and EL images related to Al-BSF modules are reported in Figure E.1a and b. This type of cells showed a good stability during the whole test. All recorder I-V curves well overlap and no sign of degradation is visible from the EL images. The I-V curves of PERC (Figure E.1c) and SHJ (Figure E.1e) modules instead showed the same  $I_{sc}$  reduction already after a UV dose of 20kWh/m<sup>2</sup>. The ring shape observed from the EL images of the PERC cells was attributed to a the poor quality of the wafer after production, specifically do to the presence of oxygen precipitates during the ingot growth [170]. The sensitivity to the UV exposure of these *novel* cell architectures was also observed by Witteck [171] and more recently

Table E.1: Aging tests conditions.

Test type	Air Temperature [°C]	Black panel Temperature [°C]	Relative Humidity [%]	UV intensity (@ 340 nm) [W/m <sup>2</sup> ]	Test duration
IEC 62788-7-2	65	90	20	0.8	63 kWh/m <sup>2</sup>

## Appendix E. Effect of the UV on Al-BSF, PERC, and SHJ G-G modules

---

by Sinha [139], with an addition reduction of the  $V_{oc}$ . The degradation was attributed to the higher energetic UV photons, which are able to pass the encapsulant and break the Si-H bond reach in the SiN-Si and in the n/a-Si interfaces of PERC and SHJ, respectively. This leads to an increased surface recombination. However, our results did not show any  $V_{oc}$  reduction, hence the degradation mechanism might be different in this specific case. To understand the cause of this degradation, occurring especially on novel c-Si cell architectures more investigations are needed.

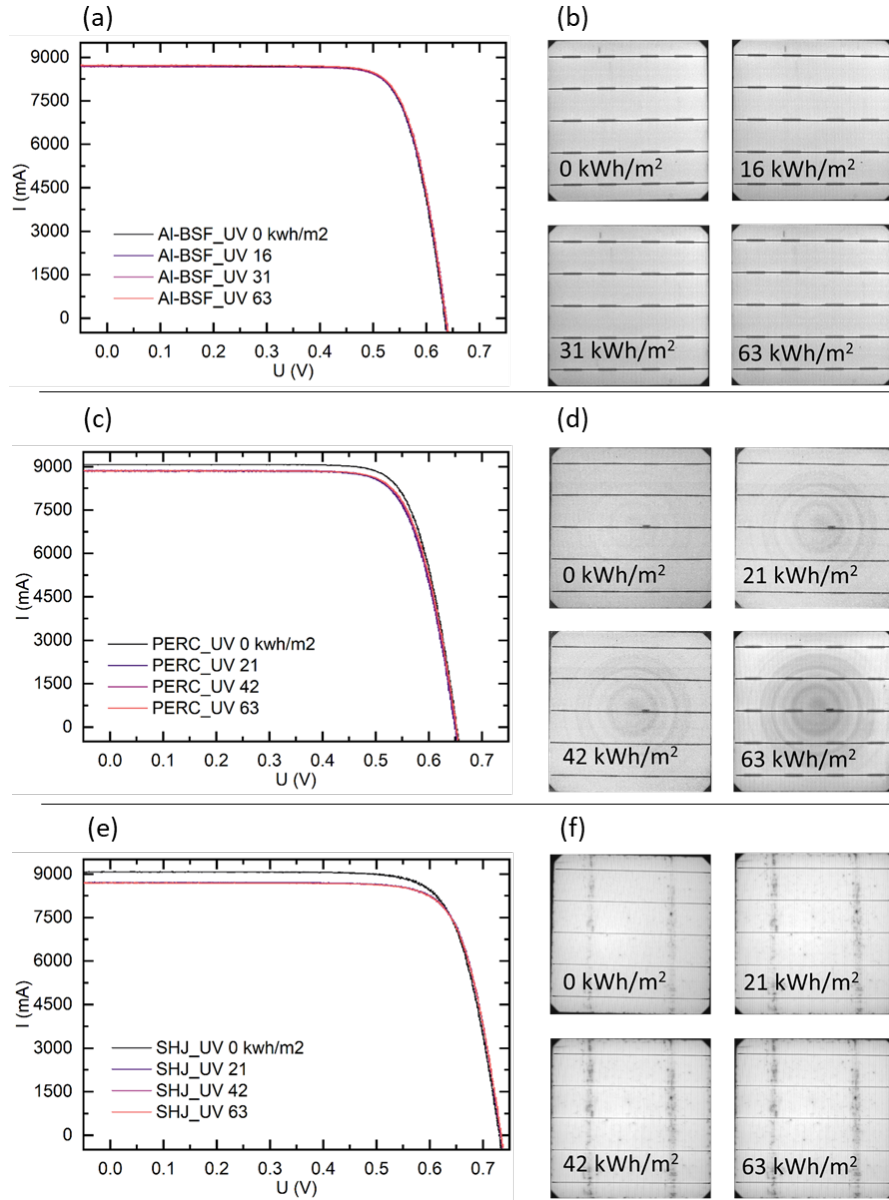


Figure E.1: I-V measurements and EL images of G-G EVA single cell modules using Al-BSF (a-b), PERC (c-d), and SHJ (e-f) during UV aging test up to a cumulative UV dose of 63kWh/m<sup>2</sup>. Al-BSF cells are stable during the whole test duration. PERC and SHJ cells suffer  $I_{sc}$  degradation already after a UV dose of 20kWh/m<sup>2</sup>.





## **F Measurements of the water content in uncured EVA foils after storage**

The choice of the three storage conditions used in Chapter 5 (i.e. EVA-30, EVA-65, and EVA-100) was the result of a pre-study conducted to quantify the water absorbed by the polymer in environments with different relative humidity (RH). The EVA foil were stored in a climatic chamber for 5 days at different RH values. Inside the climatic chamber the relative humidity was kept constant at the set value. Samples were then taken out the chamber to measure the absorbed water. During the time interval between the opening of the climatic chamber and the measurement (i.e. preparation time), the RH was not constant (i.e. the ventilation system inside the laboratory keeps the RH at lower values compared to the ones set inside the climatic chamber). Hence, during the "*preparation time*" a moisture gradient between the conditioned samples and the surrounding environment existed.

To measure the water concentration in the EVA film we used a Coulometric C30 Karl Fisher Titrator (from Metler Toledo). To extract all the absorbed water from a solid sample, such as the EVA film, the titrator machine was coupled with a Stromboli Oven. EVA samples were first inserted in a vial and then heated up in the oven at 170°C to evaporate all the trapped water. A nitrogen flux carried the extrated water from the vial to the titration cell. The titration measurement time was set at 600 seconds.

We observed a correlation between the measured water concentration in the EVA and the "*preparation time*". Figure E1 shows the water concentration as a function of the "*preparation time*" for different pre-conditioning conditions (i.e. 60°C and 30, 65 and 85% RH). When the *preparation time* was prolonged, the measured water was less.

This results is important to understand the adopted storage strategy. The estimated *preparation time* for the 1-cell modules, could not be reduced down to ~70 seconds. For such *preparation time* duration the water concentration inside the samples was already halved compared to the extrapolated value at 0 seconds (i.e. the estimated water saturation concentration reached inside the climatic chamber). Consequently, the EVA-100 condition was chosen as this extreme condition assured that a considerable quantity of moisture was present until the lamination process starts, regardless the *preparation time*.

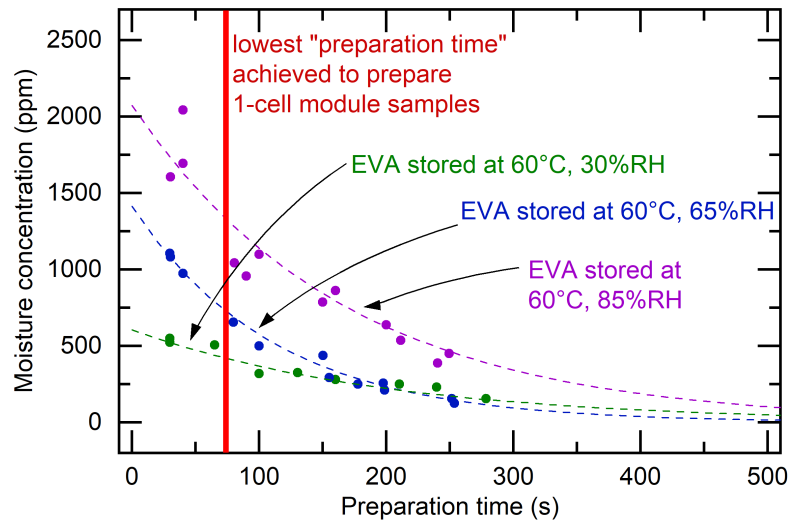


Figure F1: Water concentration as a function of the *preparation time* for different storage conditions. The colored points indicate the experimentally measured values. Dotted curves are the corresponding moisture concentration functions.

# G Water ingress simulations during real outdoor exposure

The moisture ingress was modeled as a diffusion problem using the *Transport of Diluted Species interface* in Comsol Multiphysics (version 5.3). For the purpose of this work (see Chapter 5), FEM simulations are employed to model the water ingress into a standard 60 cells glass-glass module exposed during 20 years in two different climates. The meteorological data for the chosen climatic zones (i.e. Mumbai (IN) and Sharurah (SA)) were downloaded from the Solcast web platform.

The following described procedure, was previously set up by former PV-Lab colleagues, Valentin Chapuis, Federico Galliano and Eleonora Annigoni.

In order to model the water ingress of a field exposed PV module, the temperature dependency of the EVA diffusivity properties must be inserted in Comsol.

## Module temperature evaluation

As the EVA properties varies with the temperature, the initial step was to use the King's equation [172] to evaluate the temperature of the module depending on the mounting structure, module configuration and meteorological data, such as air temperature, wind speed and solar irradiance. The temperature at the back-side of the module is given by Equation G.1.

$$T_{mod}(t) = T_{air}(t) + E \cdot \exp(a + b \cdot SW) \quad (G.1)$$

where:

- $T_{air}$  is the ambient temperature;
- $E$  is the solar irradiance incident on module surface;
- $a$  is an empirically-determined coefficient establishing the upper limit for module temperature at low wind speeds and high solar irradiance;

## Appendix G. Water ingress simulations during real outdoor exposure

---

- $b$  empirically-determined coefficient establishing the rate at which module temperature drops as wind speed increases;
- $WS$  is the wind speed.

The empirical values  $a$  and  $b$  were chosen from [172] for an open-rack glass-glass module type.

The temperature of the EVA was set equal to the module temperature.

### Water surface concentration and diffusion coefficient

The water concentration at the surface of the module was calculated following the Equations reported in the Appendix A and the related EVA diffusivity properties as a function of the temperature.

Particularly, the water saturation pressure was computed as a function of the air temperature with the Arden-Buck equation (Equation A.6). The actual vapor pressure was then computed with the Equation A.5:

$$p_{H_2O}(t) = RH(t) \cdot p_{H_2O}^{sat} \quad (G.2)$$

In parallel, solubilities of water in EVA as a function of  $T_{mod}$  are re-written from Equation A.3 as:

$$S_{EVA}(T_{mod}, t) = S_{30^\circ C} \cdot \exp\left(\frac{-E_{a,S}}{R} \left(\frac{1}{T_{mod}(t) + 273.15} - \frac{1}{30 + 273.15}\right)\right) \quad (G.3)$$

where:

- $S_{30^\circ C}$  is the solubility value of water in EVA at 30°C (calculated in Appendix A);
- $E_{a,S}$  is the activation energy for the solubility, reported in in Appendix A, Table A.1;
- $R$  is the gas universal constant (8.314 J/mol/K)

Finally, the water concentration at the external EVA surface is evaluated:

$$c_{surf}(T_{mod}, t) = S_{EVA}(T_{mod}, t) \cdot p_{H_2O}(t) \quad (G.4)$$

The diffusion coefficient as a function of the  $T_{mod}(t)$  was calculated with the same Arrhenius function as for the solubility:

---


$$D_{EVA}(T_{mod}, t) = D_{30^{\circ}C} \cdot \exp\left(\frac{-E_{a,D}}{R} \left(\frac{1}{T_{mod}(t) + 273.15} - \frac{1}{30 + 273.15}\right)\right) \quad (G.5)$$

where:

- $D_{30^{\circ}C}$  is the diffusion coefficient at 30°C (calculated in Appendix A);
- $E_{a,D}$  is the activation energy for the diffusion, reported in in Appendix A, Table A.1;
- $R$  is the gas universal constant (8.314 J/mol/K)

Simulations were run with a time step of 7200 sec (i.e.2 hours) over a time of 20 years.



# Bibliography

- [1] Working Group 1, “AR6 Climate Change 2021: The Physical Science Basis,” 2021.
- [2] C. J. Rhodes, “The 2015 paris climate change conference: Cop21,” *Science Progress*, vol. 99, no. 1, pp. 97–104, 2016, pMID: 27120818. [Online]. Available: <https://doi.org/10.3184/003685016X14528569315192>
- [3] British Petroleum. (2020) bp Statistical Review of World Energy 2020. [Online]. Available: [bp.com/en/global/corporate/energy-economics/statistical-review-of-world-energy.html](https://www.bp.com/en/global/corporate/energy-economics/statistical-review-of-world-energy.html)
- [4] U. IEA, “Global energy review 2020,” *Ukraine*. [Online] [https://www. iea. org/coun-tries/ukraine](https://www.iea.org/countries/ukraine) [Accessed: 2020-09-10], 2020.
- [5] International Energy Agency. (2021) Net Zero by 2050: A Roadmap for the Global Energy Sector. [Online]. Available: [iea.li/nzedata](https://www.iea.li/nzedata)
- [6] G. G. Jones and L. Bouamane, ““power from sunshine”: A business history of solar energy,” *Harvard Business School Working Paper Series*, 2012.
- [7] International Energy Agency. (2021) Snapshot of global PV markets. [Online]. Available: <https://iea-pvps.org/snapshot-reports/snapshot-2021/>
- [8] I. E. Agency, *Renewables 2021*, 2021. [Online]. Available: <https://www.oecd-ilibrary.org/content/publication/6dcd2e15-en>
- [9] Fraunhofer Institute for Solar Energy Systems. (2022) Photovoltaics Report. [Online]. Available: [ise.fraunhofer.de/en/publications/studies/photovoltaics-report.html](https://www.ise.fraunhofer.de/en/publications/studies/photovoltaics-report.html)
- [10] K. Branker, M. Pathak, and J. M. Pearce, “A review of solar photovoltaic levelized cost of electricity,” *Renewable and sustainable energy reviews*, vol. 15, no. 9, pp. 4470–4482, 2011.
- [11] G. Fisher, M. R. Seacrist, and R. W. Standley, “Silicon crystal growth and wafer technologies,” *Proceedings of the IEEE*, vol. 100, no. Special Centennial Issue, pp. 1454–1474, 2012.



- [12] D. C. Jordan, S. R. Kurtz, K. VanSant, and J. Newmiller, "Compendium of photovoltaic degradation rates," *Progress in Photovoltaics: Research and Applications*, vol. 24, no. 7, pp. 978–989, 2016.
- [13] A. D. International Renewable Energy Agency, *Renewable Power Generation Costs in 2020*, 2021.
- [14] M. A. Green, "The passivated emitter and rear cell (perc): From conception to mass production," *Solar Energy Materials and Solar Cells*, vol. 143, pp. 190–197, 2015.
- [15] P. T. news. Trina solar sets 210mm perc cell efficiency record of 23.56%.
- [16] J. Melskens, B. W. van de Loo, B. Macco, L. E. Black, S. Smit, and W. Kessels, "Passivating contacts for crystalline silicon solar cells: From concepts and materials to prospects," *IEEE Journal of Photovoltaics*, vol. 8, no. 2, pp. 373–388, 2018.
- [17] G. Nogay, A. Ingenito, E. Rucavado, Q. Jeangros, J. Stuckelberger, P. Wyss, M. Morales-Masis, F.-J. Haug, P. Löper, and C. Ballif, "Crystalline silicon solar cells with coannealed electron-and hole-selective sic x passivating contacts," *IEEE Journal of Photovoltaics*, vol. 8, no. 6, pp. 1478–1485, 2018.
- [18] J. Solar, "Jinkosolar large-area n-type monocrystalline silicon solar cell reaches record-breaking new high efficiency of 25.25%."
- [19] S. De Wolf, A. Descoeudres, Z. C. Holman, and C. Ballif, "High-efficiency silicon heterojunction solar cells: A review," *green*, vol. 2, no. 1, pp. 7–24, 2012.
- [20] J. Liu, Y. Yao, S. Xiao, and X. Gu, "Review of status developments of high-efficiency crystalline silicon solar cells," *Journal of Physics D: Applied Physics*, vol. 51, no. 12, p. 123001, 2018.
- [21] M. Taguchi, A. Terakawa, E. Maruyama, and M. Tanaka, "Obtaining a higher voc in hit cells," *Progress in photovoltaics: research and applications*, vol. 13, no. 6, pp. 481–488, 2005.
- [22] K. Yoshikawa, H. Kawasaki, W. Yoshida, T. Irie, K. Konishi, K. Nakano, T. Uto, D. Adachi, M. Kanematsu, H. Uzu *et al.*, "Silicon heterojunction solar cell with interdigitated back contacts for a photoconversion efficiency over 26%," *Nature energy*, vol. 2, no. 5, pp. 1–8, 2017.
- [23] International Energy Agency, "Review of failures of photovoltaic modules," 01 2014.
- [24] S. Braun, G. Hahn, R. Nissler, C. Pönisch, and D. Habermann, "The multi-busbar design: an overview," *Energy Procedia*, vol. 43, pp. 86–92, 2013.
- [25] A. Faes, M. Despeisse, J. Levrat, J. Champiaud, N. Badel, M. Kiaee, T. Söderström, Y. Yao, R. Grischke, M. Gragert *et al.*, "Smartwire solar cell interconnection technology," in *Proc. 29th Eur. Photovoltaic Sol. Energy Conf*, 2014, pp. 2555–2561.

- 
- [26] A. Virtuani, *Solar Module Technology*. Cham: Springer International Publishing, 2020, pp. 219–247.
- [27] J. Escarré, H.-Y. Li, L. Sansonnens, F. Galliano, G. Cattaneo, P. Heinsteins, S. Nicolay, J. Bailat, S. Eberhard, C. Ballif *et al.*, “When pv modules are becoming real building elements: White solar module, a revolution for bipv,” in *2015 IEEE 42nd Photovoltaic Specialist Conference (PVSC)*. IEEE, 2015, pp. 1–2.
- [28] G. Oreski, G. C. Eder, Y. Voronko, A. Omazic, L. Neumaier, W. Mühleisen, G. Ujvari, R. Ebner, and M. Edler, “Performance of pv modules using co-extruded backsheets based on polypropylene,” *Solar Energy Materials and Solar Cells*, vol. 223, p. 110976, 2021.
- [29] A. Sinha, D. B. Sulas-Kern, M. Owen-Bellini, L. Spinella, S. Ulicna, S. A. Pelaez, S. Johnston, and L. T. Schelhas, “Glass/glass photovoltaic module reliability and degradation: a review,” *Journal of Physics D: Applied Physics*, 2021.
- [30] M. Fischer, M. Woodhouse, S. Herritsch, and J. Trube, “International technology roadmap for photovoltaic (itrpv),” Technical Report, Tech. Rep., 2020.
- [31] G. Oreski, A. Omazic, G. C. Eder, Y. Voronko, L. Neumaier, W. Mühleisen, C. Hirschl, G. Ujvari, R. Ebner, and M. Edler, “Properties and degradation behaviour of polyolefin encapsulants for photovoltaic modules,” *Progress in Photovoltaics: Research and Applications*, vol. 28, no. 12, pp. 1277–1288, 2020.
- [32] I. E. Commission *et al.*, “Iec 60050-191, 1990–12: International electrotechnical vocabulary. chapter 191: Dependability and quality of service.”
- [33] Z. Campeau, M. Anderson, E. Hasselbrink, D. Kavulak, Y. Shen, R. Lacerda, A. Terao, S. Caldwell, Z. Defreitas, L. Leonard *et al.*, “Sunpower module degradation rate,” *Sun-Power Corpor*, pp. 1–61, 2013.
- [34] P. O’Connor and A. Kleyner, *Practical reliability engineering*. John Wiley & Sons, 2012.
- [35] D. Kececioglu, *Reliability engineering handbook*. DEStech Publications, Inc, 2002, vol. 1.
- [36] D. DeGraaff, R. Lacerda, Z. Campeau *et al.*, “Degradation mechanisms in si module technologies observed in the field; their analysis and statistics,” in *NREL 2011 Photovoltaic Module Reliability Workshop*, vol. 20, 2011.
- [37] G. C. Eder, Y. Voronko, G. Oreski, W. Mühleisen, M. Knausz, A. Omazic, A. Rainer, C. Hirschl, and H. Sonnleitner, “Error analysis of aged modules with cracked polyamide backsheets,” *Solar Energy Materials and Solar Cells*, vol. 203, p. 110194, 2019.
- [38] M. Quintana, D. King, T. McMahon, and C. Osterwald, “Commonly observed degradation in field-aged photovoltaic modules,” in *Conference Record of the Twenty-Ninth IEEE Photovoltaic Specialists Conference, 2002*. IEEE, 2002, pp. 1436–1439.

- [39] G. Jorgensen and T. McMahon, "Accelerated and outdoor aging effects on photovoltaic module interfacial adhesion properties," *Progress in Photovoltaics: Research and Applications*, vol. 16, no. 6, pp. 519–527, 2008.
- [40] I. E. Commission *et al.*, "Iec 61215/2016. crystalline silicium terrestrial photovoltaic (pv) modules—design qualification and type approval," *International Electrotechnical Commission (IEC): Geneva, Switzerland*, 2016.
- [41] Oliveira Martins, Ana Cristina, "Glass free lightweight PV building elements solutions to minimize weight and maximize durability," 2019.
- [42] J. H. Wohlgemuth, D. W. Cunningham, P. Monus, J. Miller, and A. Nguyen, "Long term reliability of photovoltaic modules," in *2006 IEEE 4th World Conference on Photovoltaic Energy Conference*, vol. 2. IEEE, 2006, pp. 2050–2053.
- [43] D. C. Jordan, T. J. Silverman, J. H. Wohlgemuth, S. R. Kurtz, and K. T. VanSant, "Photovoltaic failure and degradation modes," *Progress in Photovoltaics: Research and Applications*, vol. 25, no. 4, pp. 318–326, 2017.
- [44] C. Osterwald and T. McMahon, "History of accelerated and qualification testing of terrestrial photovoltaic modules: A literature review," *Progress in Photovoltaics: Research and Applications*, vol. 17, no. 1, pp. 11–33, 2009.
- [45] A. Virtuani, M. Caccivio, E. Annigoni, G. Friesen, D. Chianese, C. Ballif, and T. Sample, "35 years of photovoltaics: analysis of the tiso-10-kw solar plant, lessons learnt in safety and performance—part 1," *Progress in Photovoltaics: Research and Applications*, vol. 27, no. 4, pp. 328–339, 2019.
- [46] E. Annigoni, A. Virtuani, M. Caccivio, G. Friesen, D. Chianese, and C. Ballif, "35 years of photovoltaics: Analysis of the tiso-10-kw solar plant, lessons learnt in safety and performance—part 2," *Progress in Photovoltaics: Research and Applications*, vol. 27, no. 9, pp. 760–778, 2019.
- [47] W. Gambogi, T. Felder, S. MacMaster, K. Roy-Choudhury, B.-L. Yu, K. Stika, H. Hu, N. Phillips, and T. J. Trout, "Sequential stress testing to predict photovoltaic module durability," in *2018 IEEE 7th World Conference on Photovoltaic Energy Conversion (WCPEC)(A Joint Conference of 45th IEEE PVSC, 28th PVSEC & 34th EU PVSEC)*. IEEE, 2018, pp. 1593–1596.
- [48] M. Owen-Bellini, S. L. Moffitt, A. Sinha, A. M. Maes, J. J. Meert, T. Karin, C. Takacs, D. R. Jenket, J. Y. Hartley, D. C. Miller *et al.*, "Towards validation of combined-accelerated stress testing through failure analysis of polyamide-based photovoltaic backsheets," *Scientific reports*, vol. 11, no. 1, pp. 1–13, 2021.
- [49] M. Owen-Bellini, P. Hacke, D. C. Miller, M. D. Kempe, S. Spataru, T. Tanahashi, S. Mitterhofer, M. Jankovec, and M. Topič, "Advancing reliability assessments of photovoltaic

- modules and materials using combined-accelerated stress testing,” *Progress in Photovoltaics: Research and Applications*, vol. 29, no. 1, pp. 64–82, 2021.
- [50] I. E. Commission *et al.*, “Iec ts 63209-1:2021: Photovoltaic modules—extended-stress testing-part 1: Modules,” *International Electrotechnical Commission (IEC): Geneva, Switzerland*, 2021.
- [51] M. Koehl, S. Hoffmann, and S. Wiesmeier, “Evaluation of damp-heat testing of photovoltaic modules,” *Progress in Photovoltaics: Research and Applications*, vol. 25, no. 2, pp. 175–183, 2017.
- [52] A. Czanderna and F. Pern, “Encapsulation of pv modules using ethylene vinyl acetate copolymer as a pottant: A critical review,” *Solar energy materials and solar cells*, vol. 43, no. 2, pp. 101–181, 1996.
- [53] M. C. C. de Oliveira, A. S. A. D. Cardoso, M. M. Viana, and V. d. F. C. Lins, “The causes and effects of degradation of encapsulant ethylene vinyl acetate copolymer (eva) in crystalline silicon photovoltaic modules: A review,” *Renewable and Sustainable Energy Reviews*, vol. 81, pp. 2299–2317, 2018.
- [54] M. A. Green, “Silicon photovoltaic modules: a brief history of the first 50 years,” *Progress in Photovoltaics: Research and applications*, vol. 13, no. 5, pp. 447–455, 2005.
- [55] E. Cuddihy, W. Carroll, C. Coulbert, A. Gupta, and R. Liang, “Photovoltaic-module encapsulation design and materials selection: Volume 1,” Jet Propulsion Lab., Pasadena, CA (USA), Tech. Rep., 1982.
- [56] P. Willis, “Investigation of materials and processes for solar cell encapsulation,” *Final Report of JPL Contract*, no. 954527, pp. 16–18, 1986.
- [57] A. M. Henderson, “Ethylene-vinyl acetate (eva) copolymers: a general review,” *IEEE Electrical Insulation Magazine*, vol. 9, no. 1, pp. 30–38, 1993.
- [58] B. K. Sharma, U. Desai, A. Singh, and A. Singh, “Effect of vinyl acetate content on the photovoltaic-encapsulation performance of ethylene vinyl acetate under accelerated ultra-violet aging,” *Journal of Applied Polymer Science*, vol. 137, no. 2, p. 48268, 2020.
- [59] E. Cuddihy, C. Coulbert, A. Gupta, and R. Liang, “Electricity from photovoltaic solar cells: flat-plate solar array project final report. volume vii: Module encapsulation,” 1986.
- [60] F. Pern, “Ethylene-vinyl acetate (eva) encapsulants for photovoltaic modules: Degradation and discoloration mechanisms and formulation modifications for improved photostability,” *Die Angewandte Makromolekulare Chemie: Applied Macromolecular Chemistry and Physics*, vol. 252, no. 1, pp. 195–216, 1997.
- [61] A. Jentsch, K.-J. Eichhorn, and B. Voit, “Influence of typical stabilizers on the aging behavior of eva foils for photovoltaic applications during artificial uv-weathering,” *Polymer Testing*, vol. 44, pp. 242–247, 2015.

## Bibliography

---

- [62] R. F. Lange, Y. Luo, R. Polo, and J. Zahnd, "The lamination of (multi) crystalline and thin film based photovoltaic modules," *Progress in Photovoltaics: Research and Applications*, vol. 19, no. 2, pp. 127–133, 2011.
- [63] J. Dong and B. Lin, "Preparation, characterization and application of eva film containing eu<sup>3+</sup> complex with 1-tridecanecarboxylic acid ligand," *Materials Research Express*, vol. 4, no. 11, p. 116202, 2017.
- [64] H. Wenger, J. Schaefer, A. Rosenthal, B. Hammond, and L. Schlueter, "Decline of the carrisa plains pv power plant: the impact of concentrating sunlight on flat plates," in *The Conference Record of the Twenty-Second IEEE Photovoltaic Specialists Conference-1991*. IEEE, 1991, pp. 586–592.
- [65] F. Pern, "Factors that affect the eva encapsulant discoloration rate upon accelerated exposure," *Solar energy materials and solar cells*, vol. 41, pp. 587–615, 1996.
- [66] C. Peike, L. Purschke, K.-A. Weiss, M. Köhl, and M. Kempe, "Towards the origin of photochemical eva discoloration," in *2013 IEEE 39th Photovoltaic Specialists Conference (PVSC)*. IEEE, 2013, pp. 1579–1584.
- [67] J. L. Hodgson and M. L. Coote, "Clarifying the mechanism of the denisov cycle: how do hindered amine light stabilizers protect polymer coatings from photo-oxidative degradation?" *Macromolecules*, vol. 43, no. 10, pp. 4573–4583, 2010.
- [68] B. Adothu, S. Chattopadhyay, P. Bhatt, P. Hui, F. R. Costa, and S. Mallick, "Early-stage identification of encapsulants photobleaching and discoloration in crystalline silicon photovoltaic module laminates," *Progress in Photovoltaics: Research and Applications*, vol. 28, no. 8, pp. 767–778, 2020.
- [69] E. Kaplani, "Detection of degradation effects in field-aged c-si solar cells through ir thermography and digital image processing," *International Journal of Photoenergy*, vol. 2012, 2012.
- [70] M. Köntges, G. Oreski, U. Jahn, M. Herz, P. Hacke, and K.-A. Weiß, *Assessment of Photovoltaic Module Failures in the Field: International Energy Agency Photovoltaic Power Systems Programme: IEA PVPS Task 13, Subtask 3: Report IEA-PVPS T13-09: 2017*. International Energy Agency, 2017.
- [71] B.-Å. Sultan and E. Sörvik, "Thermal degradation of eva and eba—a comparison. i. volatile decomposition products," *Journal of applied polymer science*, vol. 43, no. 9, pp. 1737–1745, 1991.
- [72] F. Pern and A. Czanderna, "Characterization of ethylene vinyl acetate (eva) encapsulant: Effects of thermal processing and weathering degradation on its discoloration," *Solar Energy Materials and Solar Cells*, vol. 25, no. 1-2, pp. 3–23, 1992.

- 
- [73] U. Desai, B. K. Sharma, A. Singh, and A. Singh, "Enhancement of resistance against damp heat aging through compositional change in pv encapsulant poly (ethylene-co-vinyl acetate)," *Solar Energy*, vol. 211, pp. 674–682, 2020.
- [74] H. Yin, Y. Zhou, S. Sun, W. Tang, W. Shan, X. Huang, and X. Shen, "Optical enhanced effects on the electrical performance and energy yield of bifacial pv modules," *Solar Energy*, vol. 217, pp. 245–252, 2021.
- [75] L. Wang, Y. Tang, S. Zhang, F. Wang, and J. Wang, "Energy yield analysis of different bifacial pv (photovoltaic) technologies: Topcon, hjt, perc in hainan," *Solar Energy*, vol. 238, pp. 258–263, 2022.
- [76] R. Kopecek and J. Libal, "Bifacial photovoltaics 2021: Status, opportunities and challenges," *Energies*, vol. 14, no. 8, p. 2076, 2021.
- [77] G. Raina and S. Sinha, "A simulation study to evaluate and compare monofacial vs bifacial perc pv cells and the effect of albedo on bifacial performance," *Materials Today: Proceedings*, vol. 46, pp. 5242–5247, 2021.
- [78] C. D. Rodríguez-Gallegos, M. Bieri, O. Gandhi, J. P. Singh, T. Reindl, and S. Panda, "Monofacial vs bifacial si-based pv modules: Which one is more cost-effective?" *Solar Energy*, vol. 176, pp. 412–438, 2018.
- [79] P. Tillmann, K. Jäger, and C. Becker, "Minimising the levelised cost of electricity for bifacial solar panel arrays using bayesian optimisation," *Sustainable Energy & Fuels*, vol. 4, no. 1, pp. 254–264, 2020.
- [80] W. Gambogi, M. Demko, B.-L. Yu, S. Kurian, S. MacMaster, K. R. Choudhury, J. Tracy, D. Hu, and H. Hu, "Transparent backsheets for bifacial photovoltaic modules," in *2020 47th IEEE Photovoltaic Specialists Conference (PVSC)*. IEEE, 2020, pp. 1651–1657.
- [81] A. P. Patel, A. Sinha, and G. Tamizhmani, "Field-aged glass/backsheets and glass/glass pv modules: encapsulant degradation comparison," *IEEE Journal of Photovoltaics*, vol. 10, no. 2, pp. 607–615, 2019.
- [82] P. M. Thorat, S. P. Waghmare, A. Sinha, A. Kumar, and G. TamizhMani, "Reliability analysis of field-aged glass/glass pv modules: Influence of different encapsulant types," in *2020 47th IEEE Photovoltaic Specialists Conference (PVSC)*. IEEE, 2020, pp. 1816–1822.
- [83] J. Tang, C. Ju, R. Lv, X. Zeng, J. Chen, D. Fu, J.-N. Jaubert, and T. Xu, "The performance of double glass photovoltaic modules under composite test conditions," *Energy Procedia*, vol. 130, pp. 87–93, 2017.
- [84] Chinese pv industry brief: Higher cell prices and plans for 36 gw of new cell capacity. [Online]. Available: <https://www.pv-magazine.com/2020/08/12/chinese-pv-industry-brief-higher-cell-prices-and-plans-for-36-gw-of-new-cell-capacity/>

- [85] C. Barretta, G. Oreski, S. Feldbacher, K. Resch-Fauster, and R. Pantani, "Comparison of degradation behavior of newly developed encapsulation materials for photovoltaic applications under different artificial ageing tests," *Polymers*, vol. 13, no. 2, p. 271, 2021.
- [86] M. Köntges, S. Kurtz, C. Packard, U. Jahn, K. A. Berger, K. Kato, T. Friesen, H. Liu, M. Van Iseghem, J. Wohlgemuth *et al.*, "Review of failures of photovoltaic modules," 2014.
- [87] P. Devices—Part, "3: Measurement principles for terrestrial photovoltaic (pv) solar devices with reference spectral irradiance data," *International Organization for Standardization, ISO Central Secretariat, Geneva, Switzerland, ISO/IEC*, pp. 60 904–3, 2008.
- [88] J. Ahmad, A. Ciocia, S. Fichera, A. F. Murtaza, and F. Spertino, "Detection of typical defects in silicon photovoltaic modules and application for plants with distributed mppt configuration," *Energies*, vol. 12, no. 23, p. 4547, 2019.
- [89] N. S. Allen, M. Edge, M. Rodriguez, C. M. Liauw, and E. Fontan, "Aspects of the thermal oxidation of ethylene vinyl acetate copolymer," *Polymer Degradation and Stability*, vol. 68, no. 3, pp. 363–371, 2000.
- [90] D. C. Miller, J. Bengoechea, J. G. Bokria, M. Köhl, N. E. Powell, M. E. Smith, M. D. White, H. R. Wilson, and J. H. Wohlgemuth, "Examination of an optical transmittance test for photovoltaic encapsulation materials," in *Reliability of Photovoltaic Cells, Modules, Components, and Systems VI*, vol. 8825. International Society for Optics and Photonics, 2013, p. 882509.
- [91] C. Hirschl, M. Biebl-Rydlo, M. DeBiasio, W. Mühleisen, L. Neumaier, W. Scherf, G. Oreski, G. Eder, B. Chernev, W. Schwab *et al.*, "Determining the degree of crosslinking of ethylene vinyl acetate photovoltaic module encapsulants—a comparative study," *Solar Energy Materials and Solar Cells*, vol. 116, pp. 203–218, 2013.
- [92] W. Stark and M. Jaunich, "Investigation of ethylene/vinyl acetate copolymer (eva) by thermal analysis dsc and dma," *Polymer Testing*, vol. 30, no. 2, pp. 236–242, 2011.
- [93] M. Brogly, M. Nardin, and J. Schultz, "Effect of vinylacetate content on crystallinity and second-order transitions in ethylene—vinylacetate copolymers," *Journal of applied polymer science*, vol. 64, no. 10, pp. 1903–1912, 1997.
- [94] M. Kempe, "Rheological and mechanical considerations for photovoltaic encapsulants," National Renewable Energy Lab.(NREL), Golden, CO (United States), Tech. Rep., 2005.
- [95] H. Li, L.-E. Perret-Aebi, R. Theron, C. Ballif, Y. Luo, and R. FM Lange, "Towards in-line determination of eva gel content during pv modules lamination processes," in *Proceedings of the 25th PVSC Conference*, no. CONF, 2010.
- [96] S. I. 11357-3, "Plastics—differential scanning calorimetry (dsc)—part 3: Determination of temperature and enthalpy of melting and crystallization," 1999.

- 
- [97] H.-Y. Li, L.-E. Perret-Aebi, R. Théron, C. Ballif, Y. Luo, and R. F. Lange, "Optical transmission as a fast and non-destructive tool for determination of ethylene-co-vinyl acetate curing state in photovoltaic modules," *Progress in Photovoltaics: Research and Applications*, vol. 21, no. 2, pp. 187–194, 2013.
- [98] I. T. 62788-7-2, "Measurement procedures for materials used in photovoltaic modules—part 7-2: Environmental exposures—accelerated weathering tests of polymeric materials," 2017.
- [99] Trinasolar, "Datasheet peg5 cn 2016 a," [https://static.trinasolar.com/sites/default/files/PS-M-0472%20B%20Datasheet\\_Duomax%20M%20Plus\\_DEG5.XX%28II%29\\_US\\_Jan2018\\_TS4\\_0.pdf](https://static.trinasolar.com/sites/default/files/PS-M-0472%20B%20Datasheet_Duomax%20M%20Plus_DEG5.XX%28II%29_US_Jan2018_TS4_0.pdf), 2016, datasheet.
- [100] —, "600w datasheet vertex deg20c20 en 2020 pa2 web," [https://static.trinasolar.com/sites/default/files/MA\\_Datasheet\\_Vertex\\_DEG20C.20\\_202009.pdf](https://static.trinasolar.com/sites/default/files/MA_Datasheet_Vertex_DEG20C.20_202009.pdf), 2020, datasheet.
- [101] Panasonic, "Approaches to the long-term stability of silicon heterojunction modules," 2021, presented at the 4th International SHJ Workshop.
- [102] Y. Ino, S. Asao, K. Shirasawa, and H. Takato, "Effect of soldering on the module degradation along bus bar in dh test and pct for crystalline si pv modules," in *2018 IEEE 7th World Conference on Photovoltaic Energy Conversion (WCPEC)(A Joint Conference of 45th IEEE PVSC, 28th PVSEC & 34th EU PVSEC)*. IEEE, 2018, pp. 3552–3557.
- [103] R. E. Kumar, G. Von Gastrow, N. Theut, A. M. Jeffries, T. Sidawi, A. Ha, F. DePlachett, H. Moctezuma-Andraca, S. Donaldson, M. I. Bertoni *et al.*, "Glass vs. backsheets: Deconvoluting the role of moisture in power loss in silicon photovoltaics with correlated imaging during accelerated testing," *IEEE Journal of Photovoltaics*, vol. 12, no. 1, pp. 285–292, 2021.
- [104] N. Kim and C. Han, "Experimental characterization and simulation of water vapor diffusion through various encapsulants used in pv modules," *Solar energy materials and solar cells*, vol. 116, pp. 68–75, 2013.
- [105] D. B. Sulas-Kern, M. Owen-Bellini, P. Ndione, L. Spinella, A. Sinha, S. Uličná, S. Johnston, and L. T. Schelhas, "Electrochemical degradation modes in bifacial silicon photovoltaic modules," *Progress in Photovoltaics: Research and Applications*, 2021.
- [106] J. Zhu, M. Owen-Bellini, D. Montiel-Chicharro, T. R. Betts, and R. Gottschalg, "Effect of viscoelasticity of ethylene vinyl acetate encapsulants on photovoltaic module solder joint degradation due to thermomechanical fatigue," *Japanese Journal of Applied Physics*, vol. 57, no. 8S3, p. 08RG03, 2018.
- [107] S. Mitterhofer, C. Barretta, L. F. Castillon, G. Oreski, M. Topič, and M. Jankovec, "A dual-transport model of moisture diffusion in pv encapsulants for finite-element simulations," *IEEE Journal of Photovoltaics*, vol. 10, no. 1, pp. 94–102, 2019.



## Bibliography

---

- [108] M. Mittag, U. Eitner, and T. Neff, "Tpedge: progress on cost-efficient and durable edge-sealed pv modules," *33rd EUPVSEC*, pp. 25–29, 2017.
- [109] M. D. Kempe, G. J. Jorgensen, K. M. Terwilliger, T. J. McMahon, C. E. Kennedy, and T. T. Borek, "Acetic acid production and glass transition concerns with ethylene-vinyl acetate used in photovoltaic devices," *Solar energy materials and solar cells*, vol. 91, no. 4, pp. 315–329, 2007.
- [110] B. Ketola and A. Norris, "Degradation mechanism investigation of extended damp heat aged pv modules," *26th EUPVSEC*, 2011.
- [111] M. D. Kempe and J. H. Wohlgemuth, "Evaluation of temperature and humidity on pv module component degradation," in *2013 IEEE 39th Photovoltaic Specialists Conference (PVSC)*. IEEE, 2013, pp. 0120–0125.
- [112] W. Herrmann and N. Bogdanski, "Outdoor weathering of pv modules—effects of various climates and comparison with accelerated laboratory testing," in *2011 37th IEEE Photovoltaic Specialists Conference*. IEEE, 2011, pp. 002 305–002 311.
- [113] M. Jankovec, E. Annigoni, C. Ballif, and M. Topič, "In-situ determination of moisture diffusion properties of pv module encapsulants using digital humidity sensors," in *2018 IEEE 7th World Conference On Photovoltaic Energy Conversion (Wcpec)(A Joint Conference Of 45Th Ieee Pvsc, 28Th Pvsec & 34Th Eu Pvsec)*. IEEE, 2018, pp. 0415–0417.
- [114] D. Adachi, J. L. Hernández, and K. Yamamoto, "Impact of carrier recombination on fill factor for large area heterojunction crystalline silicon solar cell with 25.1% efficiency," *Applied Physics Letters*, vol. 107, no. 23, p. 233506, 2015.
- [115] X. Ru, M. Qu, J. Wang, T. Ruan, M. Yang, F. Peng, W. Long, K. Zheng, H. Yan, and X. Xu, "25.11% efficiency silicon heterojunction solar cell with low deposition rate intrinsic amorphous silicon buffer layers," *Solar energy materials and solar cells*, vol. 215, p. 110643, 2020.
- [116] M. A. Green, E. D. Dunlop, J. Hohl-Ebinger, M. Yoshita, N. Kopidakis, and X. Hao, "Solar cell efficiency tables (version 58)," *Progress in Photovoltaics: Research and Applications*, vol. 29, no. 7, pp. 657–667, 2021.
- [117] J. Haschke, O. Dupré, M. Boccard, and C. Ballif, "Silicon heterojunction solar cells: Recent technological development and practical aspects-from lab to industry," *Solar Energy Materials and Solar Cells*, vol. 187, pp. 140–153, 2018.
- [118] D. Andronikov, A. Abramov, S. Abolmasov, K. Emtsev, G. Ivanov, I. Nyapshaev, D. Orekhov, A. Semenov, G. Shelopin, E. Terukova *et al.*, "A successful conversion of silicon thin film solar cell module production to high efficiency heterojunction technology," in *Proceedings of 33rd European PV Solar Energy Conference and Exhibition, September*, pp. 25–29.

- [119] W. Favre, G. Condorelli, A.-S. Ozanne, A. Canino, D. Muñoz, P. Rotoli, A. Battaglia, J.-F. Lerat, A. Moustafa, A. Valla, J. Stendera, F. Medlege, M. Fernandes, V. Barth, A. Ragonesi, P.-J. Ribeyron, M. Guercio, and C. Gerardi, "From advanced thin-films modules to high efficiency silicon heterojunction technology at 3sun," 09 2017.
- [120] G. Cattaneo, J. Levrat, H. Li, V. Barth, L. Sicot, A. Richter, C. Colletti, F. Rametta, M. Izzi, M. Despeisse, and C. Ballif, "Encapsulant materials for high reliable bifacial heterojunction glass/glass photovoltaic modules," in *2020 47th IEEE Photovoltaic Specialists Conference (PVSC)*, 2020, pp. 1056–1061.
- [121] J. Karas, A. Sinha, V. S. P. Buddha, F. Li, F. Moghadam, G. TamizhMani, S. Bowden, and A. Augusto, "Damp heat induced degradation of silicon heterojunction solar cells with cu-plated contacts," *IEEE Journal of Photovoltaics*, vol. 10, no. 1, pp. 153–158, 2019.
- [122] S. Hava, J. Ivri, and M. Auslender, "Wavenumber-modulated patterns of transmission through one-and two-dimensional gratings on a silicon substrate," *Journal of Optics A: Pure and Applied Optics*, vol. 3, no. 6, p. S190, 2001.
- [123] K. Kusová, O. Cibulka, K. Dohnalová, I. Pelant, J. Valenta, A. Fucikova, K. Zidek, J. Lang, J. Englich, P. Matejka *et al.*, "Brightly luminescent organically capped silicon nanocrystals fabricated at room temperature and atmospheric pressure," *ACS nano*, vol. 4, no. 8, pp. 4495–4504, 2010.
- [124] Y. Sun, P. Gao, J. He, S. Zhou, Z. Ying, X. Yang, Y. Xiang, and J. Ye, "Rear-sided passivation by sin x: H dielectric layer for improved si/pedot: Pss hybrid heterojunction solar cells," *Nanoscale Research Letters*, vol. 11, no. 1, pp. 1–7, 2016.
- [125] W. Liu, L. Zhang, X. Yang, J. Shi, L. Yan, L. Xu, Z. Wu, R. Chen, J. Peng, J. Kang *et al.*, "Damp-heat-stable, high-efficiency, industrial-size silicon heterojunction solar cells," *Joule*, vol. 4, no. 4, pp. 913–927, 2020.
- [126] X. Li, W. Liu, W. Zhao, S. Huang, W. Huang, J. Shi, A. Han, J. Li, H. Chen, L. Zhang *et al.*, "Highly crystallized tungsten doped indium oxide film stabilizes silicon heterojunction solar cells in sodium environment," *Solar Energy Materials and Solar Cells*, vol. 233, p. 111387, 2021.
- [127] V. Guiheneuf, F. Delaleux, O. Riou, P.-O. Logerais, and J.-F. Durastanti, "Investigation of damp heat effects on glass properties for photovoltaic applications," *Corrosion Engineering, Science and Technology*, vol. 52, no. 3, pp. 170–177, 2017.
- [128] D. Adachi, T. Terashita, T. Uto, J. L. Hernández, and K. Yamamoto, "Effects of siox barrier layer prepared by plasma-enhanced chemical vapor deposition on improvement of long-term reliability and production cost for cu-plated amorphous si/crystalline si heterojunction solar cells," *Solar Energy Materials and Solar Cells*, vol. 163, pp. 204–209, 2017.

## Bibliography

---

- [129] K. Ohdaira, S. Yamaguchi, and A. Masuda, "Potential-induced degradation of silicon heterojunction photovoltaic modules," in *3rd International Workshop on Silicon Heterojunction Solar Cells: Science and Industry Technology*.
- [130] G. Oreski, B. Ottersböck, and A. Omazic, "Degradation processes and mechanisms of encapsulants," in *Durability and Reliability of Polymers and Other Materials in Photovoltaic Modules*. Elsevier, 2019, pp. 135–152.
- [131] J. Jin, S. Chen, and J. Zhang, "Uv aging behaviour of ethylene-vinyl acetate copolymers (eva) with different vinyl acetate contents," *Polymer degradation and stability*, vol. 95, no. 5, pp. 725–732, 2010.
- [132] P. Berlin, "Industry trends in pv module quality from over 250 factory audits," 2019.
- [133] S. Krauter, R. Pénidon, B. R. Lippke, M. Hanusch, and P. Grunow, "Pv module lamination durability," 2011.
- [134] S. PHOTOCAP®. Storage conditions for photocap® pv encapsulants. [Online]. Available: <http://www.strsolar.com/technical-info/technical-tips/storage-and-shelf-life/>
- [135] F. J. Pern, "Pv module encapsulation—materials, process, and reliability," in *16 th Workshop on Crystalline Silicon Solar Cells and Modules: Materials and Processes*, 2006, p. 111.
- [136] T. S. E. Malguth, B. Buhl, "Fast and non-destructive determination of the eva cross-linking degree for in-line and off-line application," in *28th European Photovoltaic Solar Energy Conference and Exhibition*, 2013, pp. 472 – 475.
- [137] K. Brecl, C. Barretta, G. Oreski, B. Malič, and M. Topič, "The influence of the eva film aging on the degradation behavior of pv modules under high voltage bias in wet conditions followed by electroluminescence," *IEEE Journal of Photovoltaics*, vol. 9, no. 1, pp. 259–265, 2018.
- [138] R. Witteck, H. Schulte-Huxel, B. Veith-Wolf, M. R. Vogt, F. Kiefer, M. Kontges, R. Peibst, and R. Brendel, "Reducing uv induced degradation losses of solar modules with c-si solar cells featuring dielectric passivation layers," in *2017 IEEE 44th Photovoltaic Specialist Conference (PVSC)*. IEEE, 2017, pp. 1366–1370.
- [139] A. Sinha, K. Hurst, S. Uličná, L. T. Schelhas, D. C. Miller, and P. Hacke, "Assessing uv-induced degradation in bifacial modules of different cell technologies," in *2021 IEEE 48th Photovoltaic Specialists Conference (PVSC)*. IEEE, 2021, pp. 0767–0770.
- [140] X. Yi, Z. Xu, Y. Liu, X. Guo, M. Ou, and X. Xu, "Highly efficient removal of uranium (vi) from wastewater by polyacrylic acid hydrogels," *RSC advances*, vol. 7, no. 11, pp. 6278–6287, 2017.

- 
- [141] B. Ottersböck, G. Oreski, and G. Pinter, "Comparison of different microclimate effects on the aging behavior of encapsulation materials used in photovoltaic modules," *Polymer Degradation and Stability*, vol. 138, pp. 182–191, 2017.
- [142] G. Oreski and G. M. Wallner, "Damp heat induced physical aging of pv encapsulation materials," in *2010 12th IEEE Intersociety Conference on Thermal and Thermomechanical Phenomena in Electronic Systems*. IEEE, 2010, pp. 1–6.
- [143] A. Badiie, R. Wildman, and I. Ashcroft, "Effect of uv aging on degradation of ethylene-vinyl acetate (eva) as encapsulant in photovoltaic (pv) modules," in *Reliability of Photovoltaic Cells, Modules, Components, and Systems VII*, vol. 9179. International Society for Optics and Photonics, 2014, p. 91790O.
- [144] C. Barretta, G. Oreski, N. Kyranaki, D. E. Mansour, T. R. Betts, L. P. Bauermann, and K. Resch-Fauster, "Effects of artificial ageing tests on eva degradation: influence of microclimate and methodology approach," in *2021 IEEE 48th Photovoltaic Specialists Conference (PVSC)*. IEEE, 2021, pp. 0312–0315.
- [145] G. W. Ehrenstein, G. Riedel, and P. Trawiel, *Thermal analysis of plastics: theory and practice*. Carl Hanser Verlag GmbH Co KG, 2012.
- [146] J. C. Schlothauer, K. Grabmayer, I. Hintersteiner, G. M. Wallner, and B. Röder, "Non-destructive 2d-luminescence detection of eva in aged pv modules: Correlation to calorimetric properties, additive distribution and a clue to aging parameters," *Solar Energy Materials and Solar Cells*, vol. 159, pp. 307–317, 2017.
- [147] N. Kyranaki, J. Zhu, R. Gottschalg, and T. Betts, "Investigating the degradation of front and rear sides of c-si pv cells exposed to acetic acid," 2018.
- [148] T. Tanahashi, N. Sakamoto, H. Shibata, and A. Masuda, "Electrical detection of gap formation underneath finger electrodes on c-si pv cells exposed to acetic acid vapor under hygrothermal conditions," in *2016 IEEE 43rd Photovoltaic Specialists Conference (PVSC)*. IEEE, 2016, pp. 1075–1079.
- [149] T. J. Trout, W. Gambogi, T. Felder, K. Choudhury, L. Garreau-Iles, Y. Heta, and K. Stika, "Pv module durability-connecting field results, accelerated testing, and materials," in *2017 IEEE 44th Photovoltaic Specialist Conference (PVSC)*. IEEE, 2017, pp. 2312–2317.
- [150] A. Masuda, S. Suzuki, Y. Hara, S. Sakamoto, and T. Doi, "Possible measure of reliability for crystalline-si photovoltaic modules," in *Proc. 29th European Photovoltaic Solar Energy Conf. Exhibition*, 2014, pp. 2566–2569.
- [151] U. Weber, R. Eiden, C. Strubel, T. Soegding, M. Heiss, P. Zachmann, K. Nattermann, H. Engelmann, A. Dethlefsen, and N. Lenck, "Acetic acid production, migration and corrosion effects in ethylene-vinyl-acetate-(eva-) based pv modules," in *27th European Photovoltaic Solar Energy Conference and Exhibition*, 2012, pp. 2992–2995.

## Bibliography

---

- [152] T. Shioda, "Acetic acid production rate in eva encapsulant and its influence on performance of pv modules," in *2nd Atlas/NIST PV Materials Durability Workshop*, 2013.
- [153] A. Masuda, N. Uchiyama, and Y. Hara, "Degradation by acetic acid for crystalline si photovoltaic modules," *Japanese Journal of Applied Physics*, vol. 54, no. 4S, p. 04DR04, 2015.
- [154] J. Zhu, D. Montiel-Chicharro, M. Owen-Bellini, T. R. Betts, and R. Gottschalg, "The role of eva encapsulation in the degradation of wafer based pv modules," 2016.
- [155] S. Suzuki, T. Tanahashi, T. Doi, and A. Masuda, "Acceleration of degradation by highly accelerated stress test and air-included highly accelerated stress test in crystalline silicon photovoltaic modules," *Japanese Journal of Applied Physics*, vol. 55, no. 2, p. 022302, 2016.
- [156] Y. Ino, S. Asao, K. Shirasawa, and H. Takato, "Investigation of degradation mode spreading interconnectors by pressure-cooker testing of photovoltaic cells," *IEEE Journal of Photovoltaics*, vol. 10, no. 1, pp. 188–196, 2019.
- [157] M. Bolivar-Telleria, C. Turbay, L. Favarato, T. Carneiro, R. S. de Biasi, A. A. R. Fernandes, A. Santos, and P. Fernandes, "Second-generation bioethanol from coconut husk," *BioMed research international*, vol. 2018, 2018.
- [158] N. Park, J. Jeong, B. Kang, and D. Kim, "The effect of encapsulant discoloration and delamination on the electrical characteristics of photovoltaic module," *Microelectronics Reliability*, vol. 53, no. 9-11, pp. 1818–1822, 2013.
- [159] L. Gnocchi, A. Virtuani, A. Vallat-Michel, A. Fairbrother, H.-Y. Li, and C. Ballif, "Measuring and modelling the generation of acetic acid in aged ethylene-vinyl acetate-based encapsulants used in solar modules," in *36th Eur. Photovolt. Sol. Energy Conf. Exhib.*, 2019, pp. 1069–1072.
- [160] I. E. Commission, T. IEC *et al.*, "63126: 2020 guidelines for qualifying pv modules, components and materials for operation at high temperatures," *International Electrotechnical Commission: Geneva, Switzerland*, 2020.
- [161] W. Oh, S. Kim, S. Bae, N. Park, S.-I. Chan, Y. Kang, H.-S. Lee, and D. Kim, "Migration of sn and pb from solder ribbon onto ag fingers in field-aged silicon photovoltaic modules," *International Journal of Photoenergy*, vol. 2015, 2015.
- [162] L. Burgio, R. J. Clark, and S. Firth, "Raman spectroscopy as a means for the identification of plattnerite (pbo<sub>2</sub>), of lead pigments and of their degradation products," *Analyst*, vol. 126, no. 2, pp. 222–227, 2001.
- [163] G. Beaucarne, L. Tous, J. Lossen, and G. Schubert, "Summary of the 9th workshop on metallization and interconnection for crystalline silicon solar cells," in *AIP Conference Proceedings*, vol. 2367, no. 1. AIP Publishing LLC, 2021, p. 020001.

- 
- [164] O. A. Arruti, L. Gnocchi, F. Lisco, A. Virtuani, and C. Ballif, "Optimized module packaging for silicon heterojunction solar cells and increased pid resistance," *EUPVSEC*, 2020.
- [165] K. Sporleder, V. Naumann, J. Bauer, S. Richter, A. Hähnel, S. Großer, M. Turek, and C. Hagendorf, "Local corrosion of silicon as root cause for potential-induced degradation at the rear side of bifacial perc solar cells," *physica status solidi (RRL)–Rapid Research Letters*, vol. 13, no. 9, p. 1900163, 2019.
- [166] M. D. Kempe, "Modeling of rates of moisture ingress into photovoltaic modules," *Solar Energy Materials and Solar Cells*, vol. 90, no. 16, pp. 2720–2738, 2006.
- [167] D. Wisniewski, R. Lv, S. V. Nair, J.-N. Jaubert, T. Xu, and H. E. Ruda, "Measurement and modelling of water ingress into double-glass photovoltaic modules," *Progress in Photovoltaics: Research and Applications*, vol. 27, no. 2, pp. 144–151, 2019.
- [168] A. Dadaniya and N. V. Datla, "Water diffusion simulation in photovoltaic module based on the characterization of encapsulant material using in-situ gravimetric technique," *Solar Energy Materials and Solar Cells*, vol. 201, p. 110063, 2019.
- [169] A. F1249-13, "Standard test method for water vapor transmission rate through plastic film and sheeting using a modulated infrared sensor," 2013.
- [170] P. Liu, C. Luo, L. Chen, H. Deng, R. Zhou, Z. Ma, L. Zhang, and L. Deng, "The influencing factors and formation mechanism of the dark ring of monocrystal silicon cells," in *2015 China Semiconductor Technology International Conference*. IEEE, 2015, pp. 1–3.
- [171] R. Witteck, B. Veith-Wolf, H. Schulte-Huxel, A. Morlier, M. R. Vogt, M. Köntges, and R. Brendel, "Uv-induced degradation of perc solar modules with uv-transparent encapsulation materials," *Progress in Photovoltaics: Research and Applications*, vol. 25, no. 6, pp. 409–416, 2017.
- [172] D. King, W. Boyson, and J. Kratochvil, "Photovoltaic array performance model, photovoltaic system r&d department," *Sandia National Laboratories*, 2004.



# Publication list

Update: 03.06.2022

## Publications as first author

1. L. Gnocchi, O. Arriga Arruti, A. Virtuani, and C. Ballif, *Insights into the sensitivity of SHJ modules to Damp Heat: a microscopic model* (working title), manuscript in preparation (2022)
2. L. Gnocchi, A. Virtuani, A. Fairbrother and C. Ballif, *The Effect of Storage Conditions on the Long-Term Stability of EVA used in glass/glass modules*, to be submitted to *Progress in Photovoltaics* (2022)

## Publications as co-author

1. A. W. Fairbrother, L. Gnocchi, A. Virtuani, C. Ballif, *Corrosion testing of solar cells: Wear-out degradation behavior*, submitted to *Solar Energy Materials and Solar Cells* (2022)
2. O. A. Arruti, L. Gnocchi, Q. Jeangros, A. Virtuani, C. Ballif, *Potential Induced Degradation Mechanism in Rear-Emitter Bifacial Silicon Heterojunction Solar Cells Encapsulated in Different Module Structures*, Proceedings of the 48th IEEE Conference on Photovoltaic Specialists (2021)
3. O. A. Arruti, L. Gnocchi, A. Virtuani, C. Ballif, *Encapsulant Selection for PID Resistant Modules made with Silicon Heterojunction Solar Cells*, Proceedings of the 37th European Photovoltaic Solar Energy Conference (2020)
4. O. A. Arruti, L. Gnocchi, F. Lisco, A. Virtuani, C. Ballif, *Optimized Module Packaging for Silicon Heterojunction Solar Cells and Increased PID Resistance*, Proceedings of the 37th European Photovoltaic Solar Energy Conference (2020)
5. A. W. Fairbrother, L. Gnocchi, A. Virtuani, C. Ballif, *Delamination of c-Si Module Encapsulation: Insight into Causes and Long-Term Effects*, Proceedings of the 37th European Photovoltaic Solar Energy Conference (2020)



6. A. Ingenito, G. Nogay, J. Stuckelberger, P. Wyss, L. Gnocchi, C. Allebé, J. Horzel, M. Despeisse, F. J. Haug, P. Löper, C. Ballif *Phosphorous-doped silicon carbide as front-side full-area passivating contact for double-side contacted c-Si solar cells*, IEEE Journal of Photovoltaics (2019)

## Conference Presentations

1. L. Gnocchi, O. A. Arruti, A. Virtuani, C. Ballif, *Insights into the sensitivity of SHJ modules to Damp Heat: a microscopic model*, oral presentation, 8th World Conference on Photovoltaic Energy Conversion (2022)
2. L. Gnocchi, A. Virtuani, C. Ballif, *The Preconditioning Effect of Uncured EVA Rolls on the Long-Term UV Exposure of Glass/Glass Modules*, visual presentation, 8th World Conference on Photovoltaic Energy Conversion (2022)
3. L. Gnocchi, A. Virtuani, C. Ballif, *EVA for Glass/Glass Solar PV Modules: Effect of encapsulant storage conditions and process parameters*, visual presentation, 48th IEEE Conference on Photovoltaic Specialists (2021)
4. L. Gnocchi, A. W. Fairbrother, Alessandro Virtuani, C. Ballif, *Effect of Encapsulant Storage Conditions on the Long-Term Photo-Induced Degradation of EVA in Double-Glass Solar PV Modules*, oral presentation, 37th European Photovoltaic Solar Energy Conference (2020)
5. L. Gnocchi, A. Virtuani, A. Vallat-Michel, A. W. Fairbrother, H.Y. Li, C. Ballif, *Measuring and Modelling the Generation of Acetic Acid in Aged Ethylene-Vinyl Acetate-Based Encapsulants Used in Solar Modules*, visual presentation, 36th European Photovoltaic Solar Energy Conference (2019)